



**SELINUS UNIVERSITY**  
OF SCIENCES AND LITERATURE

**DESIGN AND ANALYSIS OF LEAD-FREE  
PEROVSKITE BASED SOLAR CELL DEVICES IN  
STANDALONE AND TANDEM CONFIGURATION**

By **KHAGENDRA PRASAD PHULARA**

Supervised By

**PROF. DR. SALVATORE FAVA**

**A DISSERTATION**

Presented to the SELINUS UNIVERSITY OF SCIENCE AND LITERATURE

Faculty of ENGINEERING AND TECHNOLOGY

In fulfillment of the requirements for the degree of

**Doctor of Philosophy**

2022



# LIST OF FIGURES

---

Figure 1-1 AM0, AM1.5G and AM1.5D Spectral Irradiance received from the sun. Reprinted with permission from ( <a href="http://www.pveducation.org">www.pveducation.org</a> ). .....	10
Figure 1-2. The trend in PV in today's and future scenarios. Reprinted from ( <a href="https://itrvp.vdma.org/en/">https://itrvp.vdma.org/en/</a> ). .....	11
Figure 1-3. The absorption phenomena in a semiconductor (a) and thermalization loss (b). Reprinted from (Jäger, Isabella et al. 2016).....	12
Figure 1-4. Energy band diagram of homojunction (a) and heterojunction (b) solar cells. Reprinted from (Islam and Saraswat 2018, Zhang, Chen et al. 2019).....	13
Figure 1-5. Typical illuminated current density-voltage (J-V) curve for a solar cell. J-V curve for the dark is also provided for the comparison. Reprinted from (Jäger, Isabella et al. 2016).....	14
Figure 1-6. Conventional c-Si based Al-BSF solar cell. Reprinted from (Chen and Ebong 2016) .....	15
Figure 1-7. Advanced c-Si based solar cell designs (a) PERC, (b) HJT, and (c) TOPcon. Reprinted from (Chen, Chen et al. 2020, Stein, Reise et al. 2021) .....	16
Figure 1-8. Anticipated world market share of different silicon-based PV devices (a) and stabilized cell efficiency for different types of c-Si solar cell devices. Reprinted from ( <a href="https://itrvp.vdma.org/en/">https://itrvp.vdma.org/en/</a> ). .....	16
Figure 1-9. Different alternative materials for the replacement of silicon-based PV devices (a) III-V compound, (b) CIGS and (c) CZTS based PV devices. Reprinted from (Scofield, Duda et al. 1995, Enayati Maklavani and Mohammadnejad 2020, Geisz, France et al. 2020).....	17
Figure 1-10. Crystal structure of perovskite (CaTiO <sub>3</sub> ). Reprinted from (Passi and Pal 2021) .....	17
Figure 1-11. Fabrication process of perovskite solar cells using the spin coating method. Reprinted from (Tsai, Lin et al. 2020) .....	18
Figure 1-12. Schematic of perovskite silicon tandem solar cell fabricated by Sahil et al. Reprinted from (Sahli, Werner et al. 2018) .....	19
Figure 1-13. Best research cell efficiency for different technologies. Data derived from NREL ( <a href="https://www.nrel.gov/pv/cell-efficiency.html">https://www.nrel.gov/pv/cell-efficiency.html</a> ) .....	20
Figure 1-14. CH <sub>3</sub> NH <sub>3</sub> PbI <sub>3</sub> based perovskite solar cell along with crystal structure and energy band diagram. Reprinted from (Ku, Rong et al. 2013).....	22
Figure 1-15. Possible elements to replace the toxic lead material from the perovskite solar cells. Reprinted from (Wang, Wang et al. 2021).....	23

Figure 2-1: Schematic of the output structures generated by victory process, victory device and victory mesh modules of silvaco TCAD tool. ....	33
Figure 2-2: Schematic of the output structures generated by process, device and structure editing modules of SENTAURUS TCAD tools. ....	34
Figure 2-3: The main user interface of the AFORS-HET solar cell simulator.....	35
Figure 2-4: Schematic representation of different models, features, structures and results generated by SETFOS. ....	36
Figure 2-5: The main user interface of the SCAPS-1D solar cell simulator. ....	38
Figure 2-6: SCAPS-1D user interfaces for layer editing and solar cell definition (part 1). ....	39
Figure 2-7: SCAPS-1D user interfaces for layer editing and solar cell definition (part 2). ....	40
Figure 2-8: SCAPS-1D user interface for deleting, splitting and removing a layer. ....	40
Figure 2-9: SCAPS-1D user interface for defining the properties for the contact. ....	41
Figure 2-10: SCAPS-1D user interface for adding the optical and electrical properties for different layers. ....	42
Figure 2-11: SCAPS-1D user interface for selecting the optical models for a particular layer. ....	43
Figure 2-12: SCAPS-1D user interface for activating the band-to-band tunnelling. ....	43
Figure 2-13: SCAPS-1D user interface for activating the interface or intra-band tunnelling. ....	44
Figure 2-14: Flow diagram of the methodology adopted in this thesis. ....	46
Figure 3-1 Schematic device structures used during simulation for Sn-based perovskite solar cells having different iodine and bromine composition (a) D1, (b) D2, (c) D3 and (d) D4 .....	50
Figure 3-2 Energy band diagram for different Sn-based perovskite solar cells having different iodine and bromine composition (a) D1, (b) D2, (c) D3 and (d) D4. The data is obtained under thermal equilibrium.....	51
Figure 3-3 The J-V parameters for distinct defect density of $\text{MASnI}_3$ perovskite in the range of $1 \times 10^{15} \text{ cm}^{-3}$ to $1 \times 10^{17} \text{ cm}^{-3}$ at various absorber layer thicknesses (a) 100 nm (b) 200 nm (c) 300 nm (d) 400 nm and (e) 500 nm. ....	53
Figure 3-4 The J-V parameters for distinct defect density of $\text{MASnI}_2\text{Br}_1$ perovskite in the range of $1 \times 10^{15} \text{ cm}^{-3}$ to $1 \times 10^{17} \text{ cm}^{-3}$ at various absorber layer thicknesses (a) 100 nm (b) 200 nm (c) 300 nm (d) 400 nm and (e) 500 nm. ....	55
Figure 3-5 The J-V parameters for distinct defect density of $\text{MASnI}_1\text{Br}_2$ perovskite in the range of $1 \times 10^{15} \text{ cm}^{-3}$ to $1 \times 10^{17} \text{ cm}^{-3}$ at various absorber layer thicknesses (a) 100 nm (b) 200 nm (c) 300 nm (d) 400 nm and (e) 500 nm. ....	57

Figure 3-6 The J-V parameters for distinct defect density of MASnBr <sub>3</sub> perovskite in the range of $1 \times 10^{15} \text{ cm}^{-3}$ to $1 \times 10^{17} \text{ cm}^{-3}$ at various absorber layer thicknesses (a) 100 nm (b) 200 nm (c) 300 nm (d) 400 nm and (e) 500 nm. ....	58
Figure 3-7 Effect of optical transparency of substrate on (a) EQE and (b) J-V of MASnI <sub>3</sub> based PSC. ....	60
Figure 3-8 Effect of optical transparency of substrate on the PV parameters of MASnI <sub>3</sub> based PSC. ....	61
Figure 3-9 Effect of cathode work function on (a) EQE and (b) J-V of MASnI <sub>3</sub> based PSC. ....	62
Figure 3-10 Effect of cathode work function on the PV parameters of MASnI <sub>3</sub> based PSC. ....	63
Figure 3-11 Effect of cathode work function on the energy band diagram of MASnI <sub>3</sub> based PSC. ....	64
Figure 4-1 Schematic device structures used during simulation for Cs and Sn-based perovskite solar cells having different iodine and bromine composition (a) D1, (b) D2, (c) D3 and (d) D4. ....	69
Figure 4-2 Energy band diagram for different Cs and Sn-based perovskite solar cells having different iodine and bromine composition (a) D1, (b) D2, (c) D3 and (d) D4. The data is obtained under thermal equilibrium. ....	70
Figure 4-3 Absorption coefficient for different Cs and Sn-based perovskite solar cells having different iodine and bromine composition i.e., CsSnI <sub>3</sub> , CsSnI <sub>2</sub> Br <sub>1</sub> , CsSnI <sub>1</sub> Br <sub>2</sub> and CsSnBr <sub>3</sub> . ....	72
Figure 4-4 Contour plot of JSC during collective variation of defect density and absorber layer thickness for different devices (a) D1, CsSnI <sub>3</sub> (b) D2, CsSnI <sub>2</sub> Br <sub>1</sub> (c) D3, CsSnI <sub>1</sub> Br <sub>2</sub> and (d) D4, CsSnBr <sub>3</sub> ....	74
Figure 4-5 Contour plot of JSC during collective variation of defect density and absorber layer thickness for different devices (a) D1, CsSnI <sub>3</sub> (b) D2, CsSnI <sub>2</sub> Br <sub>1</sub> (c) D3, CsSnI <sub>1</sub> Br <sub>2</sub> and (d) D4, CsSnBr <sub>3</sub> ....	75
Figure 4-6 Contour plot of JSC during collective variation of defect density and absorber layer thickness for different devices (a) D1, CsSnI <sub>3</sub> (b) D2, CsSnI <sub>2</sub> Br <sub>1</sub> (c) D3, CsSnI <sub>1</sub> Br <sub>2</sub> and (d) D4, CsSnBr <sub>3</sub> ....	76
Figure 4-7 Contour plot of JSC during collective variation of defect density and absorber layer thickness for different devices (a) D1, CsSnI <sub>3</sub> (b) D2, CsSnI <sub>2</sub> Br <sub>1</sub> (c) D3, CsSnI <sub>1</sub> Br <sub>2</sub> and (d) D4, CsSnBr <sub>3</sub> ....	77
Figure 4-8 PV parameters for Cs and Sn-based halide devices (D1 to D4) at various donor densities in ETL. ....	79
Figure 4-9 PV parameters for Cs and Sn-based halide devices (D1 to D4) at various donor densities in ETL. ....	81
Figure 5-1 Multijunction tandem structure (a) four terminal or mechanically stacked (b) two-terminal monolithically stacked. Source (Werner, Niesen et al. 2018).....	85
Figure 5-2 Equivalent circuits of two-terminal monolithic tandem solar cells. Source (Pathania, Pandey et al. 2020).....	87
Figure 5-3 Reflection, transmission, and absorption spectrum of perovskite-silicon based tandem solar cells. Source (Singh, Santbergen et al. 2020).....	88
Figure 5-4 Schematic device structures and strategy used for tandem simulation of (a) TD1 and (b) TD2. ....	91

Figure 5-5 Filtered spectrum transmitted by the top cell at different absorber layer thicknesses from 100 nm to 1000 nm (a)  $\text{MASnI}_2\text{Br}_1$  based top cell and (b)  $\text{CsSnI}_1\text{Br}_2$  based top cell. ....95

Figure 5-6 Current matching curve for (a) TD1 and (b) TD2 at various top and bottom subcell thicknesses ranging from 100 nm to 1000 nm and 10  $\mu\text{m}$  to 150  $\mu\text{m}$ . ....97

Figure 5-7 J-V curve of the top cell under AM1.5G, bottom cell under filtered spectrum and tandem cell for (a) TD1 and (b) TD2. ....99

Figure 5-8 Standalone J-V curve of the top and bottom subcell and tandem J-V curve for (a) TD1 and (b) TD2. Standalone means simulation directly under the AM1.5G spectrum. ....100

Figure 5-9 Top and bottom cell EQE curve for (a) TD1 and (b) TD2. Integrated  $J_{\text{SC}}$  values are also provided to validate the final  $J_{\text{SC}}$  values. ....102

# LIST OF TABLES

---

Table 3-1 Material parameters used during simulation for Sn-based perovskite solar cells having different iodine and bromine composition (Al-Ashouri, Köhnen et al. 2020, Wang, Wang et al. 2021).....	51
Table 3-2 Interface defect parameters used during simulation for Sn-based perovskite solar cells having different iodine and bromine composition. ....	52
Table 4-1 Material parameters used during simulation for Cs and Sn-based perovskite solar cells having different iodine and bromine composition (Yang, Zhang et al. 2019, Al-Ashouri, Köhnen et al. 2020, Wang, Wang et al. 2021).....	71
Table 4-2 Interface defect parameters used during simulation for Cs and Sn-based perovskite solar cells having different iodine and bromine composition. ....	71
Table 5-1 The listed materials are used for the simulation of the bottom cell, and all the data related to its electrical and optical properties are taken from already published papers (Zhao, Zhou et al. 2008, Dao, Heo et al. 2010, Shrivastav, Madan et al. 2021). ....	92
Table 5-2 Details of interface defect parameters used during the simulations of the bottom cells (Shrivastav, Madan et al. 2021). ....	92
Table 5-3 Details of bulk defects parameters considered in intrinsic and p-type and n-type a-Si:H layers (Shrivastav, Madan et al. 2021). Detailed information regarding these parameters can be found in the SCAPS-1D manual. ....	92

# TABLE OF CONTENTS

---

## Contents

DESIGN AND ANALYSIS OF LEAD-FREE PEROVSKITE BASED SOLAR CELL DEVICES IN STANDALONE AND TANDEM CONFIGURATION.....	ii
DoctorofPhilosophy.....	ii
CHAPTER 1 .....	9
Introduction .....	9
1.1: <i>OVERVIEW OF PHOTOVOLTAIC</i> .....	9
1.2: <i>MATERIALS UTILIZED IN PV DEVICES</i> .....	15
1.3: <i>RESEARCH GAPS AND MOTIVATIONS</i> .....	21
1.4: <i>OBJECTIVES</i> .....	23
1.5: <i>THESIS OUTLINE</i> .....	24
1.6: <i>REFERENCES</i> .....	27
CHAPTER 2 .....	32
Research Methodology and Software Used .....	32
2.1: <i>LIST OF THE AVAILABLE SOLAR CELL SIMULATION TOOLS</i> .....	33
2.2: <i>FEATURES OF SCAPS-1D</i> .....	38
2.3: <i>ADOPTED METHODOLOGY</i> .....	45
2.4: <i>SUMMARY</i> .....	46
2.5: <i>REFERENCES</i> .....	47
CHAPTER 3 .....	48
Design, Simulation and Optimization of Lead-Free Methylammonium Tin Halides Based Solar Cells .....	48
3.1: <i>INTRODUCTION</i> .....	48
3.2: <i>DEVICE STRUCTURE AND SIMULATION METHODOLOGY</i> .....	50
3.3: <i>RESULTS AND DISCUSSIONS</i> .....	52
3.4: <i>SUMMARY</i> .....	64
3.5: <i>REFERENCES</i> .....	65
CHAPTER 4 .....	68

Design, Simulation and Optimization of Lead-Free Cesium Tin Halides Based Solar Cells .....	68
4.1: <i>INTRODUCTION</i> .....	68
4.2: <i>DEVICE STRUCTURE AND SIMULATION METHODOLOGY</i> .....	69
4.3: <i>RESULTS AND DISCUSSIONS</i> .....	72
4.4: <i>SUMMARY</i> .....	81
4.5: <i>REFERENCES</i> .....	82
CHAPTER 5 .....	84
Design and Simulation of Perovskite-Silicon Tandem Solar Cells using Lead Free Perovskite-Based top Cells .....	84
5.1: <i>INTRODUCTION</i> .....	84
5.2: <i>DEVICE STRUCTURE AND SIMULATION METHODOLOGY</i> .....	89
5.3: <i>RESULTS AND DISCUSSIONS</i> .....	93
5.4: <i>SCAPS-1D SCRIPT FOR TANDEM CALCULATIONS</i> .....	103
5.5: <i>SUMMARY</i> .....	106
5.6: <i>REFERENCES</i> .....	106
CHAPTER 6 .....	109
Conclusion and outlook of the thesis .....	109

# CHAPTER 1

---

---

## INTRODUCTION

---

---

### *1.1: OVERVIEW OF PHOTOVOLTAIC*

Our beautiful planet earth receives a tremendous amount of energy from the Sun in terms of electromagnetic radiation, which contains a bundle of photons with a different set of energies (Sukhatme and Nayak 2017). In the present scenario, fossil fuels that are the source of non-renewable energy are utilized for the generation of electricity (Rabaia, Abdelkareem et al. 2021). The process of burning fossil fuels also results in some concern over the environment. Therefore, it is time to look for some alternate sources of energy, and solar energy is the best among them (Li and Huang 2020). It is a form of renewable source of energy, and the amount of energy provided by the sun in one hour of global irradiance in the form of air-mass 1.5 global (AM 1.5G) spectrum as shown in Fig. 1-1 is more than sufficient to fulfill the energy need for all the humans across the world for one year (Zhang, Ren et al. 2020). However, we need to convert the Sun's energy appropriately to use the same in the desired applications (Adenle 2020). The process of conversion of optical radiation into heat is utilized in solar heaters, and the process of conversion of optical radiation into electricity is known as the photovoltaic (PV) effect (Gorjian, Sharon et al. 2021).

To generate the PV effect, PV devices are utilized, which contain the semiconductor materials as an active layer to generate the electron-hole pairs after receiving the radiation (Pandey and Chaujar 2017, Pandey, Singla et al. 2019, Pandey, Khanna et al. 2020, Zarrabi, Sandberg et al. 2020). The working principle of PV devices depends on three different processes such as (1) generation of electron-hole pairs after absorbing the photons with sufficient energy, (2) separation of generated carriers in the opposite direction with the help of semi-permeable membrane (collecting interfaces), (3) collection of the carriers in the external circuit for the delivering of the power (Zhan, Li et al. 2020). Electricity from PV into the grid jumped from 597 GWh in 2005 to about 545 TWh in 2018, and with many policies being rolled out to try and achieve net-zero in the few decades, solar panel use continues to grow around the world (Deng, Chang et al. 2021).

PV devices have some strength in terms of high lifetime, low maintenance, no requirement of fuels, environment friendly and no effect of price hike for the electricity. However, it cannot operate individually and need to be supported by battery supplies and inverters (Ziar, Manganiello et al. 2021). The current trend in global PV, as well as its future, is summarized in a report published by International Technology Roadmap for Photovoltaic (ITRPV) as stated in Fig. 1-2.

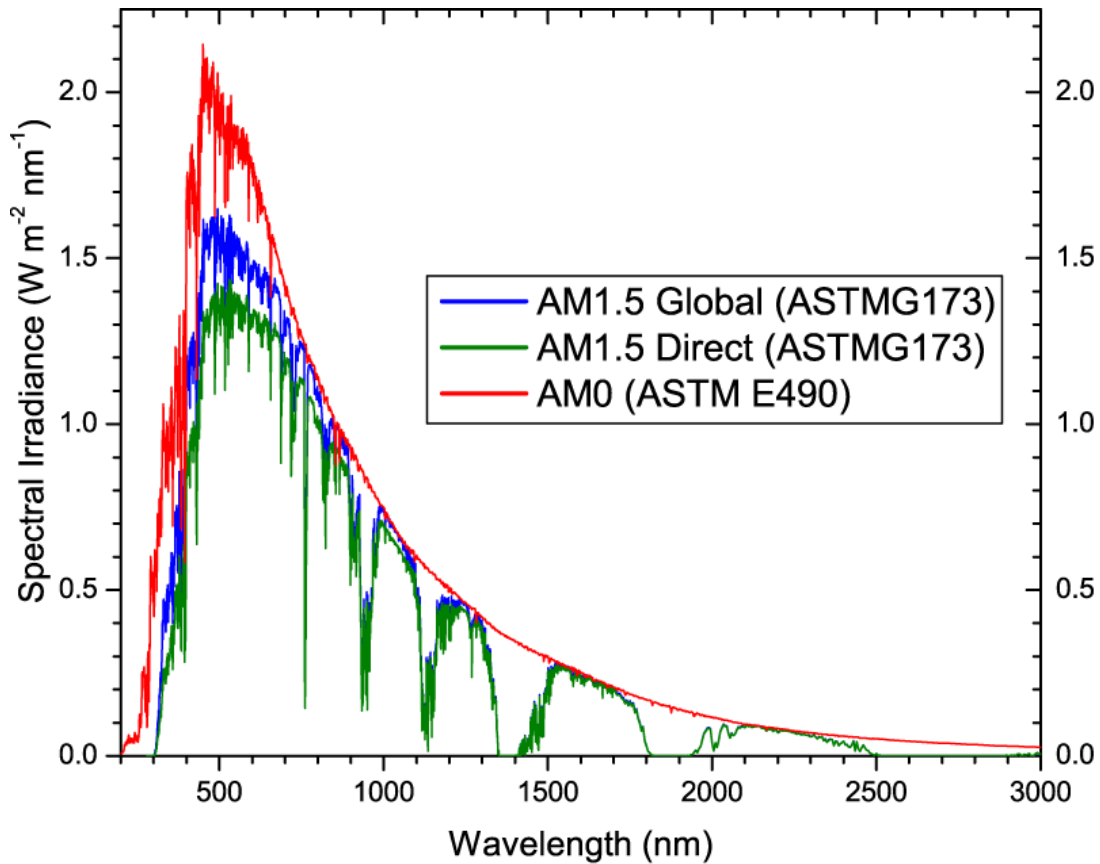


Figure 1-1 AM0, AM1.5G and AM1.5D Spectral Irradiance received from the sun. Reprinted with permission from ([www.pveducation.org](http://www.pveducation.org)).



PV today and in future

Different calculated scenarios in 11<sup>th</sup> edition:

**BNEF NEO 2019**

low: 7.6 TWp/ 9.3 PWh (22% global electricity)  
market peak: 400+GWp / 2050

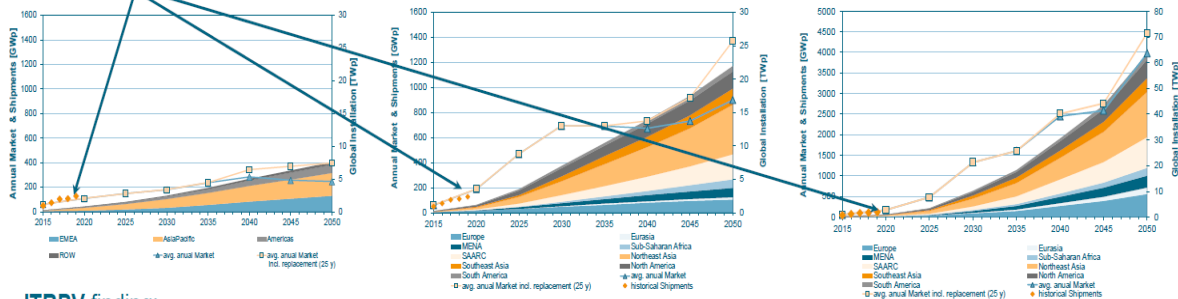
**Breyer ("Electricity")**

high: 22 TWp/ 38 PWh (69% global electricity)  
market peak: 1,400+GWp / 2050

**Breyer ("Broad electrification")**

mix: 63 TWp/ 104PWh (69% global energy)  
market peak: 4,500+ GW / 2050

→ Shipments 2019 were close to approaches!



**ITRPV finding:**

- PV learning continues and progresses but market will remain volatile esp. during unforeseen impacts like Covid-19
- Several 100GW markets are ahead, and can be served based on today's PV technologies
- Further effort is required to meet x TWp market requirements!



**ITRPV will provide also in future guidance to handle the PV challenges**

Figure 1-2. The trend in PV in today's and future scenarios. Reprinted from(<https://itrpv.vdma.org/en/>).

**1.1.1: WORKING OF SOLAR CELL**

The working principle of solar cells is based on the Photovoltaic effect. The photovoltaic effect can be divided into three basic processes as follow:

- (1) Generation of charge carriers due to the absorption of photons in the materials that form a junction:** The foremost important part of the PV effect is the generation of electron-hole pairs. Once a semiconductor material receives the appropriate energy in the form of photons, i.e., the energy of photons ( $E_{ph}$ ) must be greater than equal to the energy band gap of the semiconductor ( $E_g$ ), symbolically  $E_{ph} \geq E_g$ . It results in the formation of electron-hole pairs as depicted in Fig. 1-3 (a-b). The energy of photons equivalent to the band gap is utilized to excite the electrons for making a transition to conduction band from the valence band, and the excess energy is wasted in the form of heat as depicted in Fig. 1-3(b). The excitation process or the generation process itself is not sufficient to generate the photovoltaic effect since the excited electron would eventually recombine with the hole present in the valence band if not extracted in the external circuit.

Therefore, extraction of the generated electron-hole pairs is the essential part of the PV effect.

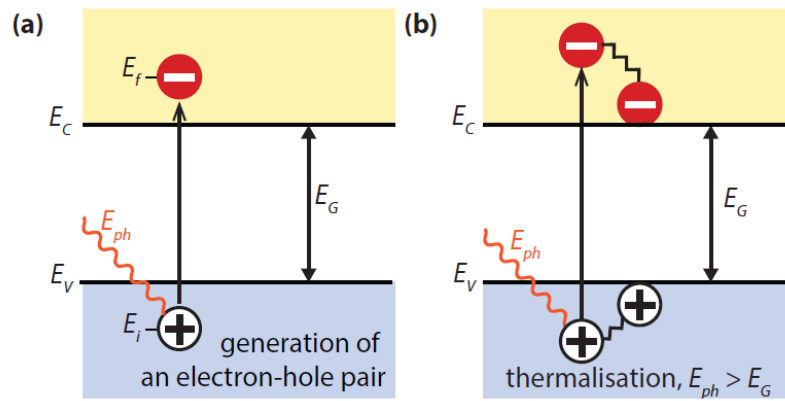


Figure 1-3. The absorption phenomena in a semiconductor (a) and thermalization loss (b). Reprinted from (Jäger, Isabella et al. 2016)

**(2) Subsequent separation of the photogenerated charge carriers in the junction:** The separation of electron-hole pairs is achieved by creating an internal electric field within the device, which helps in collecting the generated electron-hole pairs in the opposite direction. Such an electric field can be created either by doping the semiconductor material to create the homojunction or by employing the different semiconductor materials to form the heterojunction. The homojunction based devices, as shown in Fig. 1-4(a), is created by varying the doping in the different regions of the same semiconductor. This process results in creating the electric field at the junction, and this field assists in the extraction and movement of the carrier within the device, as shown in the following Fig. 1-4(a). The energy band diagram for the heterojunction device is also shown in Fig. 1-4(b), where an absorber layer is sandwiched between the electron and hole transport layer (ETL and HTL). Generated electron-hole pairs in the absorber layer travels towards the collecting interface and are separated due to the internal electric field at ETL/absorber and HTL/absorber layer interface, as shown in Fig. 1-4(b). In the next subheading, the collection process is discussed in detail.

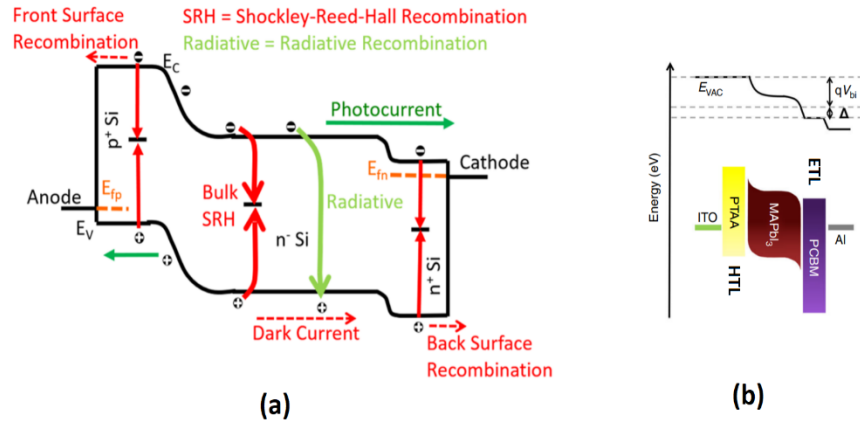


Figure 1-4. Energy band diagram of homojunction (a) and heterojunction (b) solar cells. Reprinted from (Islam and Saraswat 2018, Zhang, Chen et al. 2019)

(3) **The collection of the photogenerated charge carriers at the terminals of the junction:** As discussed in the previous subsection, the internal electric field helps in separating the electron-hole pairs. However, upon illumination, the charge carriers are generated throughout the device. Therefore, all the generated carriers need to diffuse towards the collecting interfaces for being collected at the interface. Sometimes generated carriers die before being collected at the end terminal owing to material quality or different recombination processes) within the device, as shown in Fig. 1-4(a). Therefore, sufficient carrier diffusion length is required to finally collect the light generated electron-hole pairs in the external circuits.

### 1.1.2: PHOTOVOLTAIC PARAMETERS

The performance of the solar cells is measured in terms of conversion efficiency, which is defined as the ratio of the output electrical power to the input optical power. However, this parameter depends on sum other important parameters such as quantum efficiency (QE), short circuit current density ( $J_{SC}$ ), open-circuit voltage ( $V_{OC}$ ), Fill factor (FF), and maximum power ( $P_m$ )

➤ *Quantum efficiency (QE)*= number of carriers collected/number of photons absorbed.

➤ Short circuit current density,  $I_{SC} \approx qG(L_n + L_p)$  where  $L_n$  and  $L_p$  are the electron and hole diffusion lengths, given by  $L = \sqrt{D\tau}$ ,  $D$  is diffusion coefficient, and  $\tau$  is carrier lifetimes.

➤ Open circuit voltage,  $V_{OC} = \frac{nkT}{q} \ln\left(\frac{I_L}{I_0} + 1\right)$  (1.01)

➤ Fill factor,  $FF = \frac{I_{mp}V_{mp}}{I_{SC}V_{OC}}$  (1.02)

➤ Maximum power,  $P_{max} = V_{OC}I_{SC}FF$  (1.03)

➤ Efficiency,  $\eta = \frac{V_{OC}I_{SC}FF}{P_{in}}$  (1.04)

The input AM1.5G spectrum power for efficiency calculation is  $0.1 \text{ W/cm}^2$ . Input power for  $100 \times 100 \text{ mm}^2$  cell is  $10 \text{ W}$  and for  $156 \times 156 \text{ mm}^2$  cell is  $24.3 \text{ W}$ .

Where  $n$  is the diode ideality factor,  $k$  is the Boltzmann constant,  $T$  is temperature,  $q$  is the electronic charge,  $I_L$  is the illuminated current,  $I_0$  is the reverse saturation current,  $I_{mp}$  and  $V_{mp}$  is the maximum current and voltage at the maximum power point. All the PV parameters are indicated in Fig. 1-5, which is a typical current density-voltage curve of the solar cell.

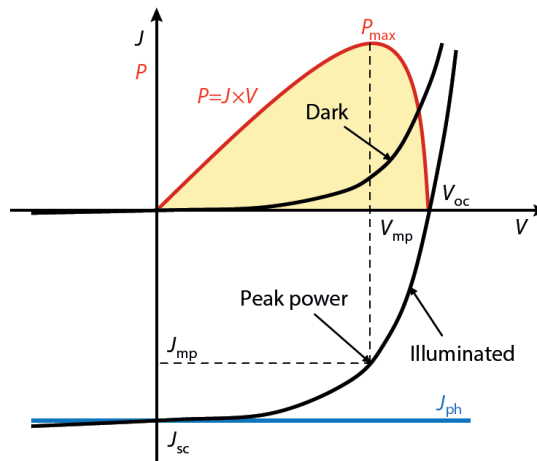


Figure 1-5. Typical illuminated current density-voltage (J-V) curve for a solar cell. J-V curve for the dark is also provided for the comparison. Reprinted from (Jäger, Isabella et al. 2016)

## 1.2: MATERIALS UTILIZED IN PV DEVICES

As of now, more than 95% PV market is dominated by crystalline silicon (c-Si) based PV devices. c-Si has been the go-to choice for decades owing to its availability and mature fabrication techniques. The conventional silicon-based devices were based on aluminium back surface field technology, as shown in Fig. 1-6. The conventional Al-BSF design had several losses associated with the back surface in terms of reflection and recombination losses that are overcome by some other mature and viable industrial approaches such as passivated emitter rear cell (PERC), silicon heterojunction (HJT), Tunnel oxide passivated contact (TOPcon), etc. Further considering the current market trend, ITRPV predicted that PERC based silicon solar cells would dominate the PV market in future, as shown in Fig. 1-7(a-c).

But silicon is not perfect as it still has issues regarding cost as well as efficiency, which typically does not go above 21% to 22% for the top-selling panels (Yu, Li et al. 2021). It is also no secret that making solar panels is a dirty business due to the intense heat required to remove the impurities from the silicon, and apart from significant dominance, the conversion efficiency for c-Si-based PV devices are stagnant, with a record conversion efficiency of 26.7% as shown in Fig. 1-13, and a further improvement in the conversion efficiency is very difficult since c-Si-based PV devices have a theoretical efficiency limit of 29.4% (Pandey and Chaujar 2016, Pandey and Chaujar 2016, Pandey and Chaujar 2017, Pandey and Chaujar 2018).

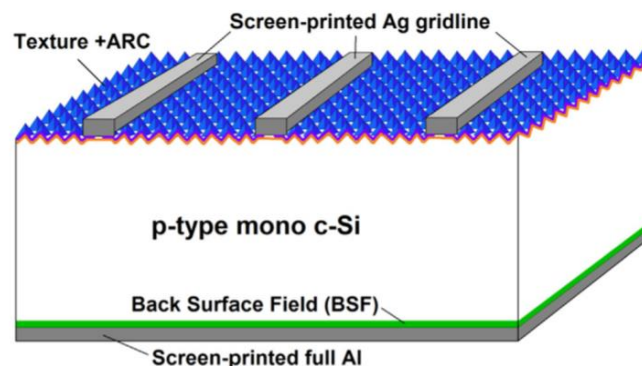


Figure 1-6. Conventional c-Si based Al-BSF solar cell. Reprinted from (Chen and Ebong 2016)

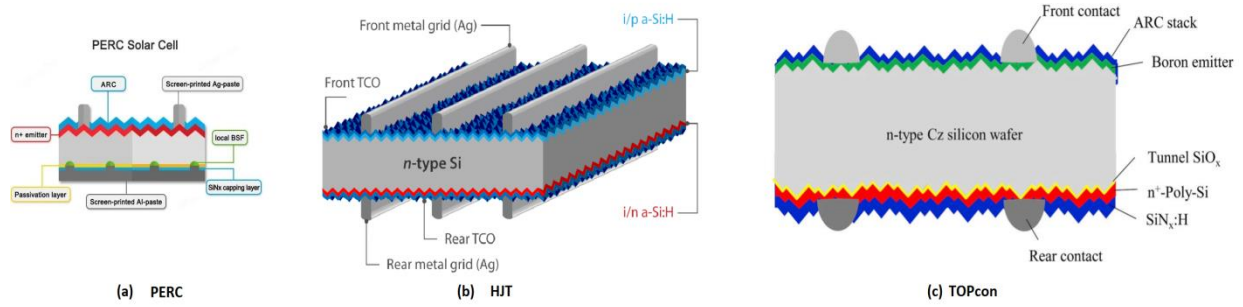


Figure 1-7. Advanced c-Si based solar cell designs (a) PERC, (b) HJT, and (c) TOPcon. Reprinted from (Chen, Chen et al. 2020, Stein, Reise et al. 2021)

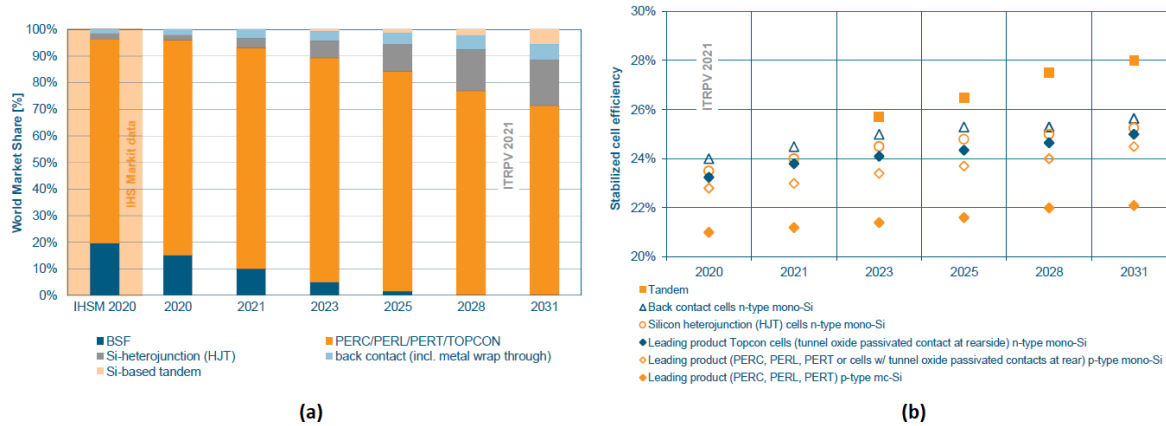


Figure 1-8. Anticipated world market share of different silicon-based PV devices (a) and stabilized cell efficiency for different types of c-Si solar cell devices. Reprinted from (<https://itrpv.vdma.org/en/>).

Therefore, researchers explored some different materials for the use in PV devices such as III-V compound semiconductors (Fig. 1-9(a)), CIGS (Fig. 1-9(b)) and CZTS (Fig. 1-9(c)), but they only cover a small piece of the market that is only about 5% (Oberbeck, Alvino et al. 2020). The main reason for the small market share is that it is hard to make them as efficient and cheaply as traditional silicon solar cells (Madan, Pandey et al. 2019, Gohri, Madan et al. 2021, Gohri, Madan et al. 2021, Yuan, Wang et al. 2021).

Therefore, researchers started exploring some different materials to be used in PV devices, and one promising technology that provided simple manufacturing and highly efficient PVs are the perovskites (Roy, Sinha et al. 2020). Perovskites are a family of materials with a particular crystal structure discovered by German scientist Gustav Rose in 1839. Any type of material that has the same crystal structure as calcium titanium oxide (CaTiO<sub>3</sub>) is considered a perovskite, as shown in Fig. 1-10.

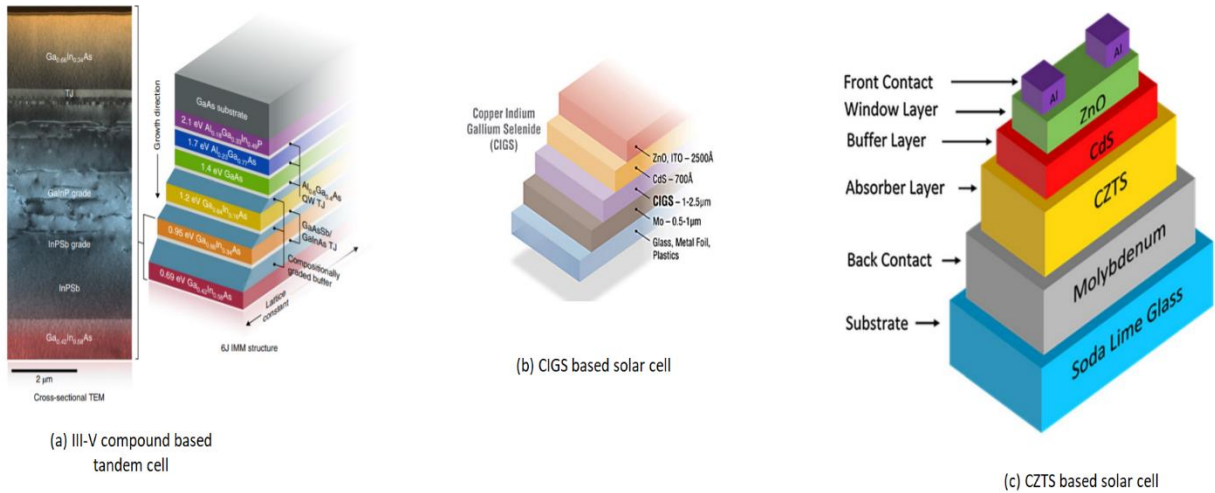


Figure 1-9. Different alternative materials for the replacement of silicon-based PV devices (a) III-V compound, (b) CIGS and (c) CZTS based PV devices. Reprinted from (Scofield, Duda et al. 1995, Enayati Maklavani and Mohammadnejad 2020, Geisz, France et al. 2020).

But it was not until the 1950s that research and development on oxide perovskite grew up, which included its use in fuel cells, glass-ceramics, superconducting devices, and more. But it was only in 1999 that perovskites started being applied to solar cells.

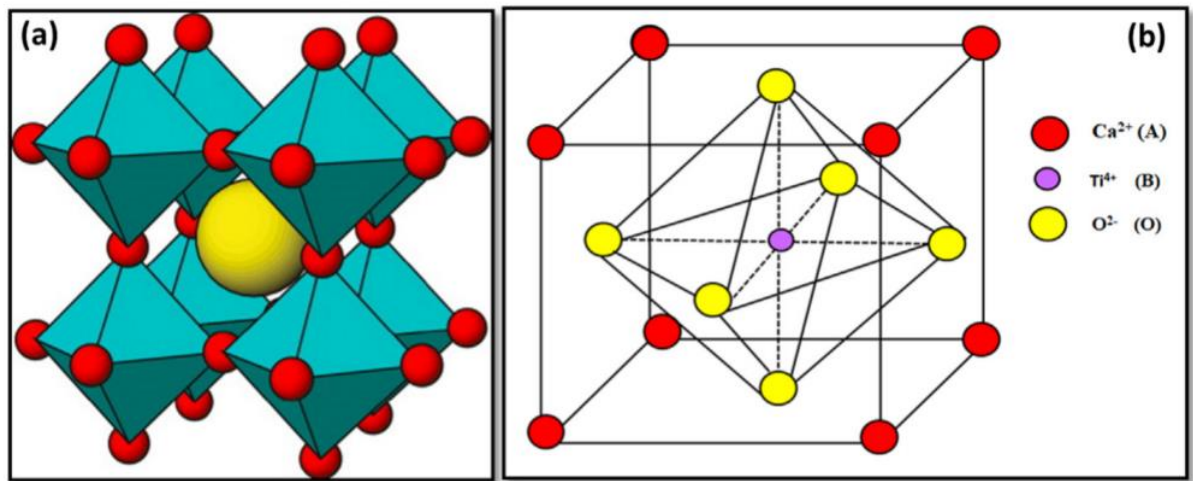


Figure 1-10. Crystal structure of perovskite (CaTiO<sub>3</sub>). Reprinted from (Passi and Pal 2021)

Researchers from the National Institute of Advanced Industrial Science and Technology from Tokyo announced that they had manufactured an optical absorption layer for a solar cell using a rare-earth-based perovskite compound. After that, the new millennium came with extensive research on perovskite solar cells and new fabrication methods and

materials. Perovskite is easy to synthesize materials and are considered the future of solar cells since their distinctive structure has shown a great potential for high performance and low production cost. These solar cells have been improved considerably in a short time frame with a boom in the conversion efficiency from reports of 3% in 2006 to over 25% today as shown in Fig. 1-13 and going over mono and polycrystalline silicon solar cells (Green, Dunlop et al. 2021). In the laboratory, PSCs are manufactured by spin coating, spraying or painting them onto a substrate, which is a material that provides the surface for the chemical to crystallize on (Roy, Sinha et al. 2020). The process flow to fabricate the perovskite devices are is shown in Fig. 1-11. These cells work much to line a traditional solar panel; compared with conventional silicon solar cells, PSCs do not require extensive heat and can be manufactured with much thinner layers (Tailor, Abdi-Jalebi et al. 2020). They can also work with almost all the visible wavelengths, resulting in more efficient transport, recombination and extraction of charges than silicon cells.

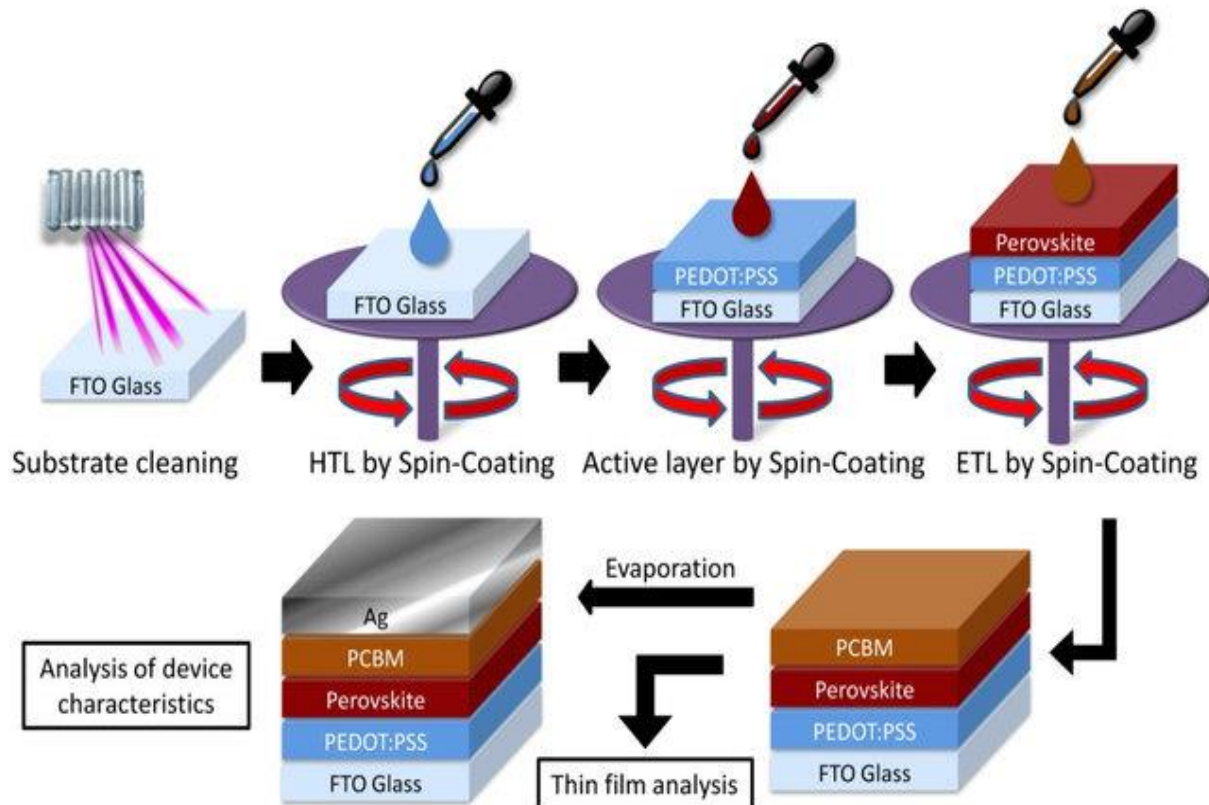


Figure 1-11. Fabrication process of perovskite solar cells using the spin coating method. Reprinted from (Tsai, Lin et al. 2020)

Perovskite can be tuned to absorb different colours in the solar spectrum, and this gives the flexibility to open up another useful application for these solar cells in a high-performance tandem device configuration that can achieve above 30% conversion efficiencies (Al-Ashouri, Köhnen et al. 2020). They can be combined with other materials like silicon, for example, to form hybrid structures like those multijunction cells (Pandey, Jain et al. 2016, Pathania, Pandey et al. 2019, Al-Ashouri, Köhnen et al. 2020). The schematic for the perovskite-silicon tandem solar cell is shown in Fig. 1-12. Each junction is a group of layers and can be tuned to cover the desired wavelengths (Madan, Pandey et al. 2020, Madan, Singh et al. 2021). However, there are some research gaps that need to be overcome before the actual industrial application of the perovskites.

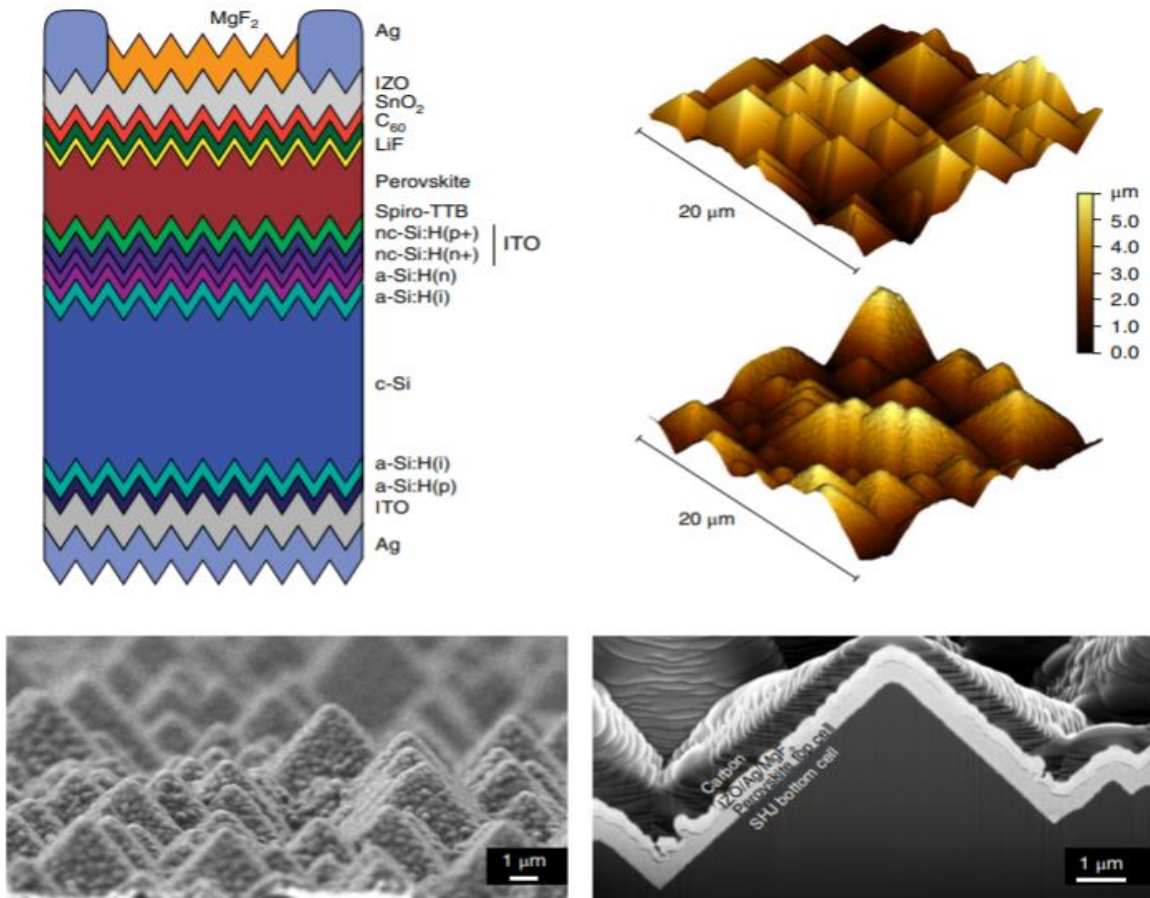


Figure 1-12. Schematic of perovskite silicon tandem solar cell fabricated by Sahil et al. Reprinted from (Sahli, Werner et al. 2018)

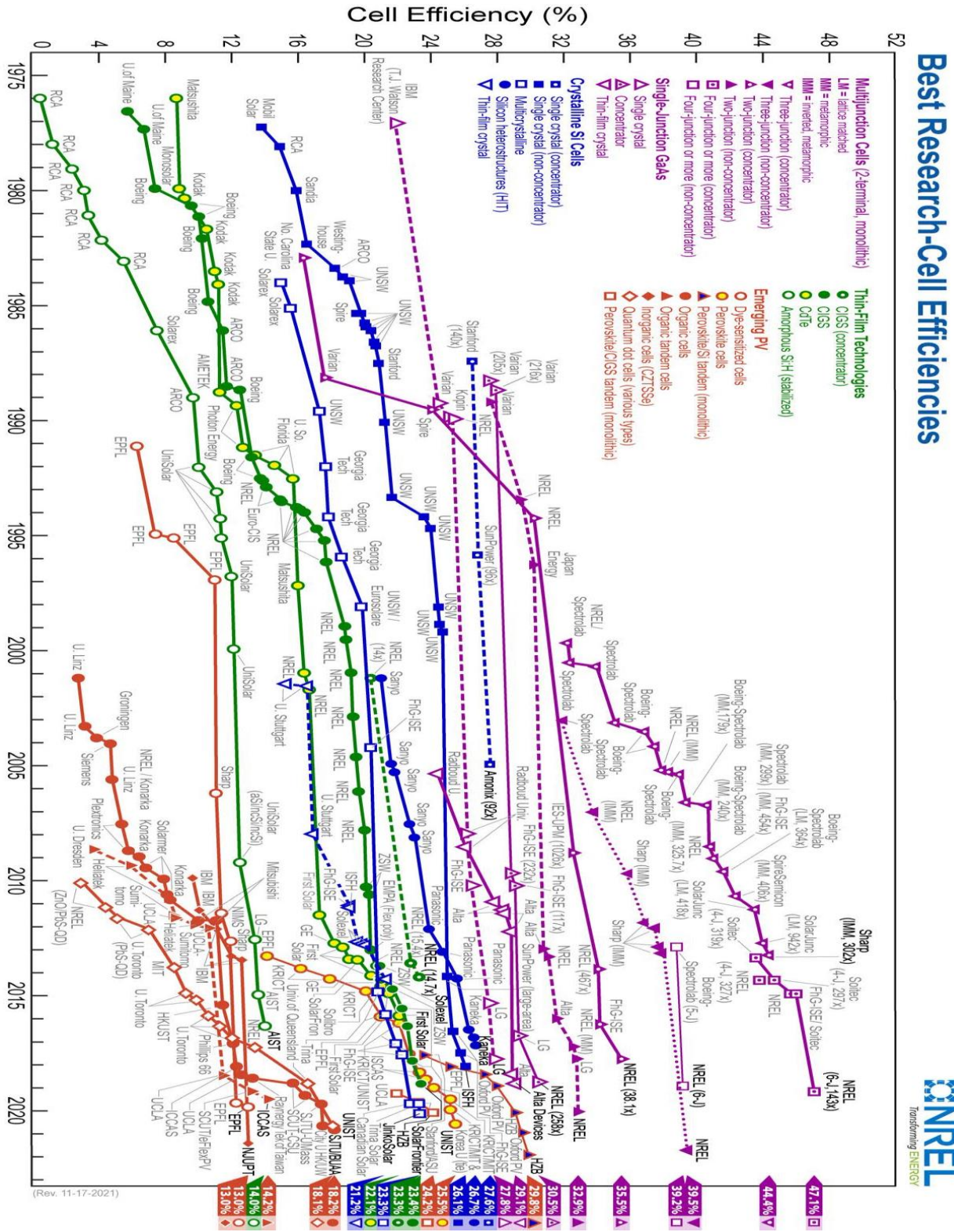


Figure 1-13. Best research cell efficiency for different technologies. Data derived from NREL (<https://www.nrel.gov/pv/cell-efficiency.html>)

### ***1.3: RESEARCH GAPS AND MOTIVATIONS***

In the near future, let's say for the next 5-10 years, we are not seeing perovskite taking over the industry. The main hurdle for the perovskite is whether they can last as long as silicon panels which generally covers 25 years warranty and can last much longer than that(Kim, Ham et al. 2021). Perovskite is very sensitive to oxygen, moisture and heat and requires heavy encapsulation to protect the cell, which increases the cost and weight(Kim, Le et al. 2021). The most common electrode material is now gold which obviously hikes up the price. At warm temperatures that structure cells shift, and although this change is reversible, it degrades the performance of the cell (Jokar, Chuang et al. 2021). However, high efficiencies have been achieved like Oxford PV perovskite-silicon cell, which reached 29.5% conversion efficiencies most perovskites haven't published their stability results(Schulze, Bett et al. 2020, Shrivastav, Madan et al. 2021). The module efficiency of perovskite falls to 80% of their initial performance in just 1-2 years on average, according to field trials in China. PSCs are simple solar cells containing metal halide perovskite. Initially, metal halide perovskites, i.e., methyl ammonium lead tri-iodide ( $\text{CH}_3\text{NH}_3\text{PbI}_3$ ), as shown in Fig. 1-14, were the working horse for the PSCs. However, they suffer from some of the inherent issues in terms of performance and stability. So, the researchers made a transition from conventional perovskites to mixed cation mixed anion materials to form the high-quality perovskite layers to be used in PSCs(Yang, Xiong et al. 2021).

Another small but questionable problem with perovskite cells is their toxicity. Lead (Pb) is used in the most common cell structure, and since it's a toxic metal substance and it needs to be carefully controlled from its manufacturing to its recycling(Tan, Chu et al. 2020). While these challenges still exist, a lot of research and development is being put into making PSC cells a reality. Scientists and companies are working towards increasing efficiency, stability as well as an increased lifespan and replacing toxic material with safer ones (Nie, Sumukam et al. 2020). The presence of toxic material in conventional PSCs also hinders the large-scale application of the PSCs. Therefore, a variety of non-toxic and less toxic materials are being deployed to be used in perovskite solar cells, which showed excellent optoelectronic properties in terms of device performance. As of now, more new materials with tunable

properties are required to be used in lead-free or low lead content-based PSCs(Li, Duan et al. 2021).

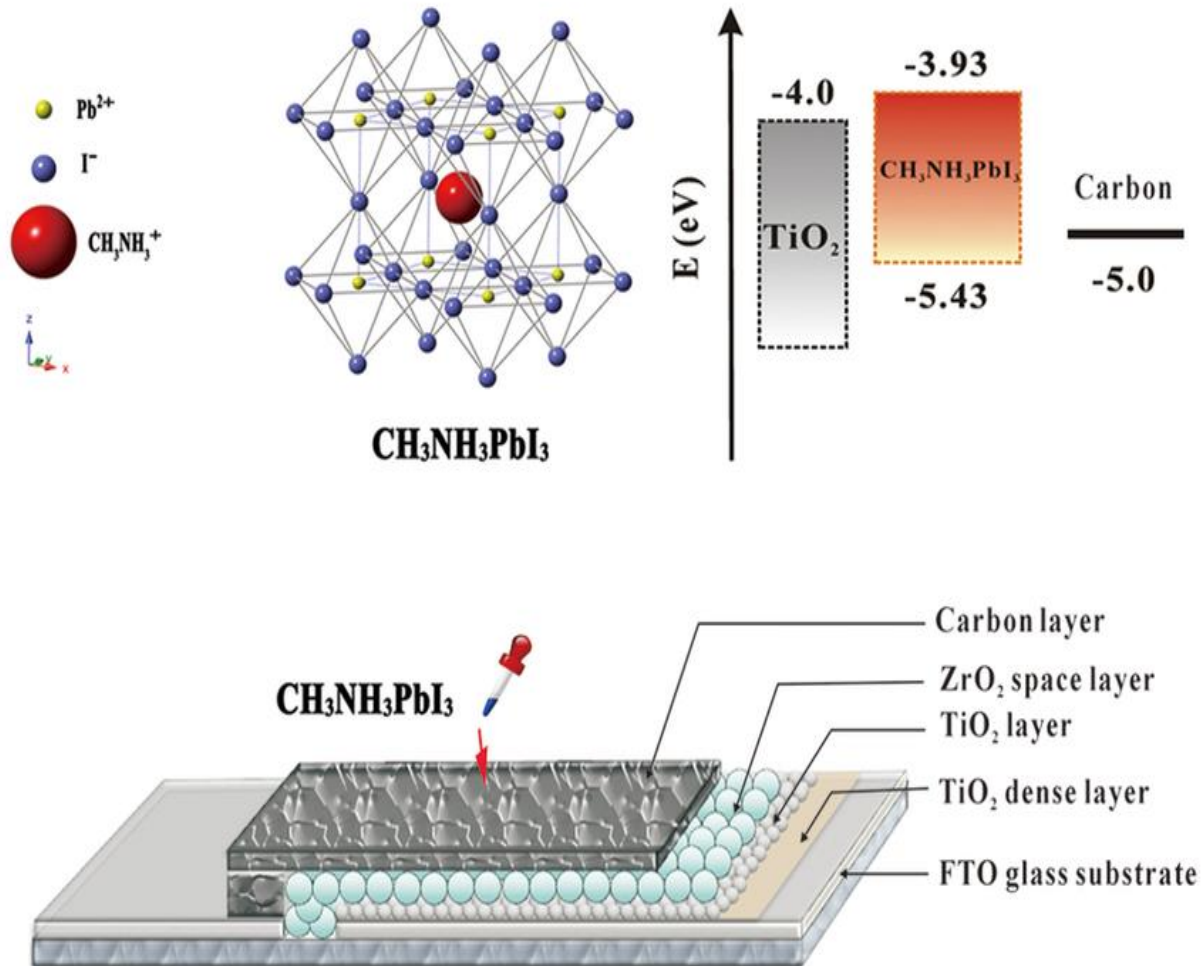


Figure 1-14.  $\text{CH}_3\text{NH}_3\text{PbI}_3$  based perovskite solar cell along with crystal structure and energy band diagram. Reprinted from (Ku, Rong et al. 2013).

Most of the researchers have published their findings on replacing the lead with some other elements, as highlighted in orange and green colour in Fig. 1-15(Wang, Wang et al. 2021). However, detailed theoretical analysis to optimize the performance of modified perovskite-based PSCs is not extensively investigated in the literature. Therefore, the ongoing thesis has been dedicated to taking up this research can make a humble contribution in the field of lead-free or low lead content perovskite solar cells.

H																	He
Li	Be										B	C	N	O	F		Ne
Na	Mg										Al	Si	P	S	Cl		Ar
K	Ca	Sc	Ti	V	Cr	Mn	Fe	Co	Ni	Cu	Zn	Ga	Ge	As	Se	Br	Kr
Rb	Sr	Y	Zr	Nb	Mo	Tc	Ru	Rh	Pd	Ag	Cd	In	Sn	Sb	Te	I	Xe
Cs	Ba		Hf	Ta	W	Re	Os	Ir	Pt	Au	Hg	Tl	Pb	Bi	Po	At	Rn
Fr	Ra		Rf	Db	Sg	Bh	Hs	Mt	Ds	Rg	Cn	Unt	Fl	Uup	Lv	Uns	Uuo

Figure 1-15. Possible elements to replace the toxic lead material from the perovskite solar cells. Reprinted from (Wang, Wang et al. 2021).

## 1.4: OBJECTIVES

In this thesis, comprehensive device simulations are performed to design and optimize the conversion efficiencies of PSCs, reduce the losses and achieve higher efficiencies. Moreover, the objective of the work done is briefly stated as follows:

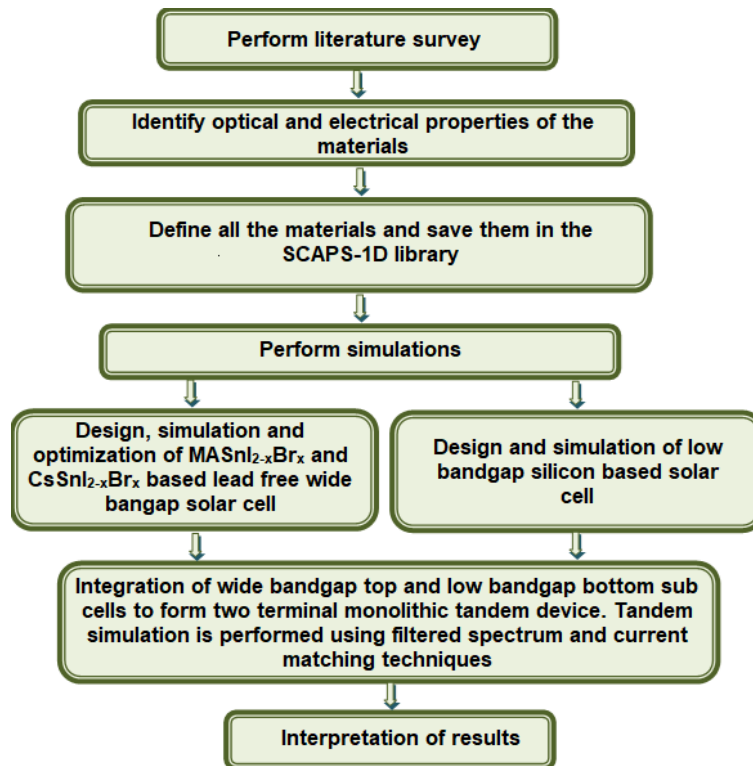
1. To list down all the available TCAD software capable of simulating solar cells and to provide a detailed description of the opted SCAPS-1D software.
2. To design and optimize the performance of  $\text{MASnI}_{3-x}\text{Br}_x$  based lead free perovskite solar cell in terms of different iodide and bromide composition, bulk defect density, absorber layer thickness, substrate transparency and cathode work function.
3. To design and optimize the performance of  $\text{CsSnI}_{3-x}\text{Br}_x$  based lead free perovskite solar cell in terms of different iodide and bromide composition, bulk defect density, absorber layer thickness, substrate transparency and cathode work function.
4. To propose and design lead free perovskite-silicon tandem solar cells to mitigate thermalization and transparent band gap losses with the help of  $\text{MASnI}_2\text{Br}_{1-x}$ – Si and  $\text{CsSnI}_1\text{Br}_2$ – Si based two terminal monolithic tandem design.

## 1.5: THESIS OUTLINE

This thesis is organized into six chapters to accommodate all the research objectives. Each chapter is organized to be fundamentally self-contained.

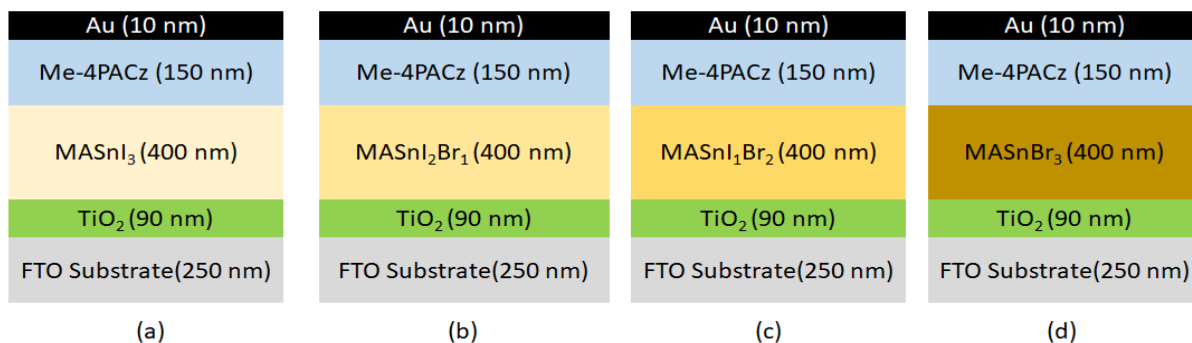
### Chapter-2

Chapter 2 provides a detailed summary of the research methodology and software used in this thesis to achieve the objectives stated in chapter 1. All the available TCAD software capable of simulating solar cells have been summarized. A detailed description of the opted SCAPS-1D software is also provided.



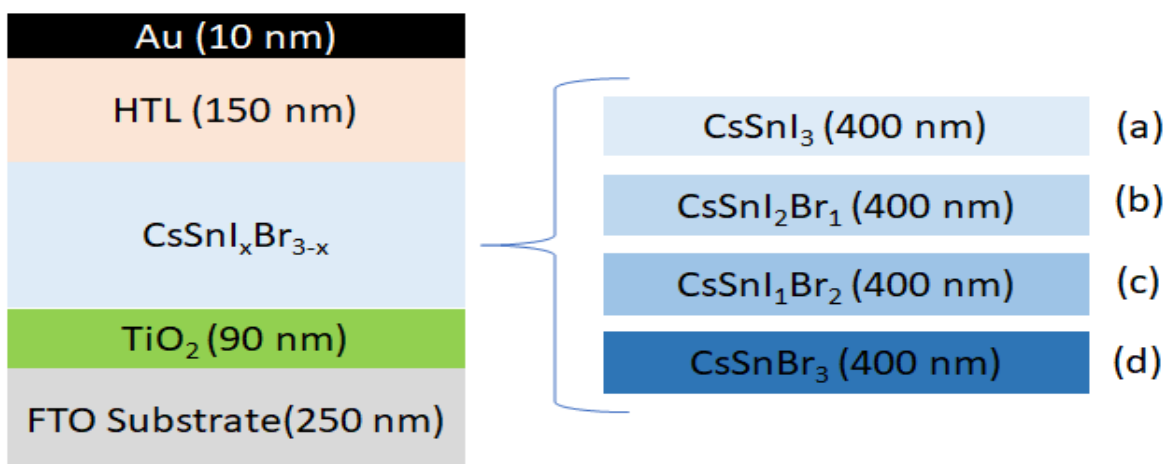
### Chapter-3

Chapter 3 provided detailed comprehensive study of one of the most widely preferred lead-free perovskite solar cell i.e.,  $\text{MA}_{1-2x}\text{Br}_x$  perovskite having different iodide and bromide composition. Performance optimization has been done with the help of energy band diagram, bulk defect density, absorber layer thickness, electrode work function and substrate transiency. A snap of the device structures considered in chapter 3 is provided below.



### Chapter-4

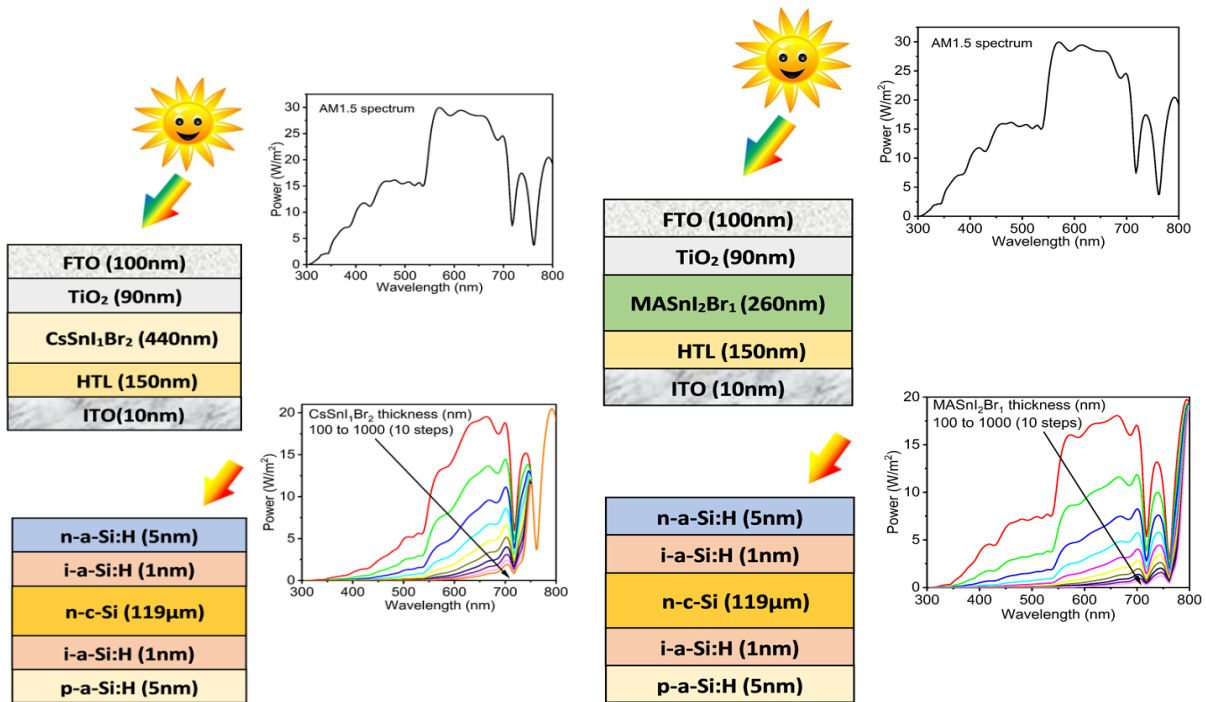
Chapter 4 provided detailed comprehensive study of another one of the most widely preferred lead-free perovskite solar cell i.e., CsSnI<sub>3-x</sub>Br<sub>x</sub> perovskite having different iodide and bromide composition. Performance optimization has been done with the help of energy band diagram, bulk defect density, absorber layer thickness, electron and hole transport layer doping density. A snap of the device structures considered in chapter 4 is provided below.



Chapter-5

Chapter-5 brought the comprehensive study of  $\text{MASnI}_2\text{Br}_1$ - Si and  $\text{CsSnI}_1\text{Br}_2$ - Si based two-terminal monolithic tandem solar cell design with 27.9% and 25.5% conversion efficiency, respectively. Tandem design is investigated using widely used filtered spectrum and current matching techniques. Filtered spectrum is calculated at varying thicknesses of perovskite top cell, and the same is fed to bottom cell for obtaining the current matching curve at different bottom sub cell thicknesses. The scripting feature is utilized to calculate the tandem curve.

A snap of the device structures considered in chapter 5 is provided below.



**Chapter-6**

Finally, the research work of the thesis is briefly summarized in **Chapter -6**, and future scopes is outlined.

**1.6: REFERENCES**

Adenle, A. A. (2020). "Assessment of solar energy technologies in Africa-opportunities and challenges in meeting the 2030 agenda and sustainable development goals." Energy Policy**137**: 111180.

Al-Ashouri, A., et al. (2020). "Monolithic perovskite/silicon tandem solar cell with > 29% efficiency by enhanced hole extraction." Science**370**(6522): 1300-1309.

Chen, D., et al. (2020). "24.58% total area efficiency of screen-printed, large area industrial silicon solar cells with the tunnel oxide passivated contacts (i-TOPCon) design." Solar Energy Materials and Solar Cells**206**: 110258.

Chen, N. and A. Ebong (2016). "Towards 20% efficient industrial Al-BSF silicon solar cell with multiple busbars and fine gridlines." Solar Energy Materials and Solar Cells**146**: 107-113.

Deng, R., et al. (2021). "Peer behaviour boosts recycling." Nature Energy**6**(9): 862-863.

Enayati Maklavani, S. and S. Mohammadnejad (2020). "Enhancing the open-circuit voltage and efficiency of CZTS thin-film solar cells via band-offset engineering." Optical and Quantum Electronics**52**(2): 72.

Geisz, J. F., et al. (2020). "Six-junction III–V solar cells with 47.1% conversion efficiency under 143 Suns concentration." Nature Energy**5**(4): 326-335.

Gohri, S., et al. (2021). Assessment of WSe<sub>2</sub> based BSF layer on CZTSSe solar cell using SCAPS-1D. 2021 IEEE 48th Photovoltaic Specialists Conference (PVSC), IEEE.

Gohri, S., et al. (2021). "Performance Analysis for SnS-and Sn<sub>2</sub>S<sub>3</sub>-Based Back Surface Field CZTSSe Solar Cell: A Simulation Study." Journal of Electronic Materials**50**(11): 6318-6328.

Gorjian, S., et al. (2021). "Recent technical advancements, economics and environmental impacts of floating photovoltaic solar energy conversion systems." Journal of Cleaner Production**278**: 124285.

Green, M., et al. (2021). "Solar cell efficiency tables (version 57)." Progress in Photovoltaics: Research and Applications**29**(1): 3-15.

Islam, R. and K. Saraswat (2018). "Limitation of Optical Enhancement in Ultra-thin Solar Cells Imposed by Contact Selectivity." Scientific Reports**8**(1): 8863.

Jäger, K.-D., et al. (2016). Solar energy: fundamentals, technology and systems, UIT Cambridge.

Jokar, E., et al. (2021). "Slow Passivation and Inverted Hysteresis for Hybrid Tin Perovskite Solar Cells Attaining 13.5% via Sequential Deposition." The Journal of Physical Chemistry Letters**12**: 10106-10111.

Kim, M. c., et al. (2021). "Advanced characterization techniques for overcoming challenges of perovskite solar cell materials." Advanced Energy Materials**11**(15): 2001753.

Kim, S. G., et al. (2021). "Capturing mobile lithium ions in a molecular hole transporter enhances the thermal stability of perovskite solar cells." Advanced Materials**33**(12): 2007431.

Ku, Z., et al. (2013). "Full Printable Processed Mesoscopic CH<sub>3</sub>NH<sub>3</sub>PbI<sub>3</sub>/TiO<sub>2</sub> Heterojunction Solar Cells with Carbon Counter Electrode." Scientific Reports**3**(1): 3132.

Li, J., et al. (2021). "Review on recent progress of lead-free halide perovskites in optoelectronic applications." Nano Energy**80**: 105526.

Li, J. and J. Huang (2020). "The expansion of China's solar energy: Challenges and policy options." Renewable and Sustainable Energy Reviews**132**: 110002.

Madan, J., et al. (2019). Designing of CZTSSe Based SnS Thin Film Solar Cell for Improved Conversion Efficiency: A Simulation Study with SCAPS. 2019 IEEE 46th Photovoltaic Specialists Conference (PVSC), IEEE.

Madan, J., et al. (2020). "Device simulation of 17.3% efficient lead-free all-perovskite tandem solar cell." Solar Energy**197**: 212-221.

Madan, J., et al. (2021). "Comprehensive device simulation of 23.36% efficient two-terminal perovskite-PbS CQD tandem solar cell for low-cost applications." Scientific Reports**11**(1): 1-13.

Nie, R., et al. (2020). "Lead-free perovskite solar cells enabled by hetero-valent substitutes." Energy & Environmental Science**13**(8): 2363-2385.

Oberbeck, L., et al. (2020). "IPVF's PV technology vision for 2030." Progress in Photovoltaics: Research and Applications**28**(11): 1207-1214.

Pandey, R. and R. Chaujar (2016). "Numerical simulation of rear contact silicon solar cell with a novel front surface design for the suppression of interface recombination and improved absorption." Current Applied Physics**16**(12): 1581-1587.

Pandey, R. and R. Chaujar (2016). "Numerical simulations: Toward the design of 27.6% efficient four-terminal semi-transparent perovskite/SiC passivated rear contact silicon tandem solar cell." Superlattices and Microstructures**100**: 656-666.

Pandey, R. and R. Chaujar (2017). "Technology computer aided design of 29.5% efficient perovskite/interdigitated back contact silicon heterojunction mechanically stacked tandem solar cell for energy-efficient applications." Journal of Photonics for Energy**7**(2): 022503.

Pandey, R. and R. Chaujar (2018). "Rear contact silicon solar cells with a-SiCX: H based front surface passivation for near-ultraviolet radiation stability." Superlattices and Microstructures**122**: 111-123.

Pandey, R., et al. (2016). Novel 4-terminal perovskite/SiC-based rear contact silicon tandem solar cell with 27.6% PCE. 2016 IEEE 43rd Photovoltaic Specialists Conference (PVSC), IEEE.

Pandey, R., et al. (2020). "Device simulations: Toward the design of > 13% efficient PbS colloidal quantum dot solar cell." Solar Energy**207**: 893-902.

Pandey, R., et al. (2019). "Toward the design of monolithic 23.1% efficient hysteresis and moisture free perovskite/c-Si HJ tandem solar cell: a numerical simulation study." Journal of Micromechanics and Microengineering**29**(6): 064001.

Passi, M. and B. Pal (2021). "A review on CaTiO<sub>3</sub> photocatalyst: Activity enhancement methods and photocatalytic applications." Powder Technology**388**: 274-304.

Pathania, A., et al. (2019). Design and simulation of novel perovskite/Mg<sub>2</sub>Si based monolithic tandem solar cell with 25.5% conversion efficiency. 2019 IEEE 46th Photovoltaic Specialists Conference (PVSC), IEEE.

Rabaia, M. K. H., et al. (2021). "Environmental impacts of solar energy systems: A review." Science of The Total Environment**754**: 141989.

Roy, P., et al. (2020). "A review on perovskite solar cells: Evolution of architecture, fabrication techniques, commercialization issues and status." Solar Energy**198**: 665-688.

Sahli, F., et al. (2018). "Fully textured monolithic perovskite/silicon tandem solar cells with 25.2% power conversion efficiency." Nature Materials**17**(9): 820-826.

Schulze, P. S., et al. (2020). "25.1% High- efficiency monolithic perovskite silicon tandem solar cell with a high bandgap perovskite absorber." Solar RRL**4**(7): 2000152.

Scofield, J. H., et al. (1995). "Sputtered molybdenum bilayer back contact for copper indium diselenide-based polycrystalline thin-film solar cells." Thin Solid Films**260**(1): 26-31.

Shrivastav, N., et al. (2021). "Investigations aimed at producing 33% efficient perovskite-silicon tandem solar cells through device simulations." RSC Advances**11**(59): 37366-37374.

Stein, J., et al. (2021). IEA PVPS Task 13 Performance, Operation and Reliability of Photovoltaic Systems - Bifacial Photovoltaic Modules and Systems: Experience and Results from International Research and Pilot Applications.

Sukhatme, S. P. and J. Nayak (2017). Solar energy, McGraw-Hill Education.

Taylor, N. K., et al. (2020). "Recent progress in morphology optimization in perovskite solar cell." Journal of Materials Chemistry A**8**(41): 21356-21386.

Tan, Z., et al. (2020). "Lead- Free Perovskite Variant Solid Solutions Cs<sub>2</sub>Sn<sub>1-x</sub>TeXCl<sub>6</sub>: Bright Luminescence and High Anti- Water Stability." Advanced Materials**32**(32): 2002443.

Tsai, C.-H., et al. (2020). "Investigation of the Effects of Various Organic Solvents on the PCBM Electron Transport Layer of Perovskite Solar Cells." Coatings**10**(3): 237.

Wang, M., et al. (2021). "Lead-Free Perovskite Materials for Solar Cells." Nano-Micro Letters**13**(1): 62.

Yang, L., et al. (2021). "Artemisinin-passivated mixed-cation perovskite films for durable flexible perovskite solar cells with over 21% efficiency." Journal of Materials Chemistry A**9**(3): 1574-1582.

Yu, J., et al. (2021). "Copper metallization of electrodes for silicon heterojunction solar cells: Process, reliability and challenges." Solar Energy Materials and Solar Cells**224**: 110993.

Yuan, M., et al. (2021). "Phase- Transfer Exchange Lead Chalcogenide Colloidal Quantum Dots: Ink Preparation, Film Assembly, and Solar Cell Construction." Small: 2102340.

Zarrabi, N., et al. (2020). "Charge-generating mid-gap trap states define the thermodynamic limit of organic photovoltaic devices." Nature Communications**11**(1): 1-10.

Zhan, L., et al. (2020). "Over 17% efficiency ternary organic solar cells enabled by two non-fullerene acceptors working in an alloy-like model." Energy & Environmental Science**13**(2): 635-645.

Zhang, M., et al. (2019). "Reconfiguration of interfacial energy band structure for high-performance inverted structure perovskite solar cells." Nature Communications**10**(1): 1-9.

Zhang, Y., et al. (2020). "Solar energy potential assessment: A framework to integrate geographic, technological, and economic indices for a potential analysis." Renewable Energy**149**: 577-586.

Ziar, H., et al. (2021). "Photovoltatronics: intelligent PV-based devices for energy and information applications." Energy & Environmental Science**14**(1): 106-126.

# CHAPTER 2

---

## RESEARCH METHODOLOGY AND SOFTWARE USED

---

The previous chapter summarizes the overview of photovoltaic, materials utilized in PV devices, research gaps and motivation for this work, and objectives. Detailed justification for opting for lead-free perovskite materials in PSCs is also provided. There are two different approaches to research and development in PSCs, namely (1) experimental and (2) theoretical. Researchers fabricate the laboratory device in the experimental method and then measure the performance parameters. This requires expensive resources, space, and the handling of sophisticated chemicals and equipment. In the second approach, which is based on theoretical analysis of the devices, a Technology Computer-Aided Design (TCAD) software is required to compute the optoelectronic performance of the device without actually fabricating the same. These studies are appreciated as they provide a detailed understanding of the carrier dynamics and device physics and predict the behaviour more accurately. Theoretical studies save a lot of resources and help the experimentalist fabricate the device with the desired performance.

Therefore, looking at the importance of simulation related study, it has been decided to complete the objective of the thesis using TCAD simulations. The ongoing chapter 2 provides a detailed summary of the research methodology and software used in this thesis to achieve the objectives stated in chapter 1. All the available TCAD software capable of simulating solar cells have been summarized. A detailed description of the opted SCAPS-1D software is also provided.

## 2.1: LIST OF THE AVAILABLE SOLAR CELL SIMULATION TOOLS

### 2.1.1: SILVACO TCAD

It is an advanced semiconductor device simulator that supports multidimensional (1D/2D/3D) device simulation developed by Silvaco, a USA based company. It is one of the widely adopted TCAD tools for simulating the devices' optical, electrical, and thermal behaviour. Core functionality includes process simulation, complex mesh generation and device simulation. Its process simulator (Victory Process) is equipped with different state of the art fabrication processes such as oxidation, ion implantation, dopant diffusion, activation, etching, deposition, epitaxy and photolithography. Solid modelling and mesh generator (Victory Mesh) is equipped with complex solid and device meshing features in 1D/2D/3D. The device simulator (Victory Device) includes core functionality such as optoelectronic, self-heating, radiation effect and electro-chemistry-based device simulations to account for realistic device simulation. Following Fig. 2-1 shows the block diagram of different features and some of the software-generated simulation output. It is paid software. Therefore, users need to get a legal license from Silvaco to carry out research and development activities using the Silvaco TACD (Silvaco 2021).

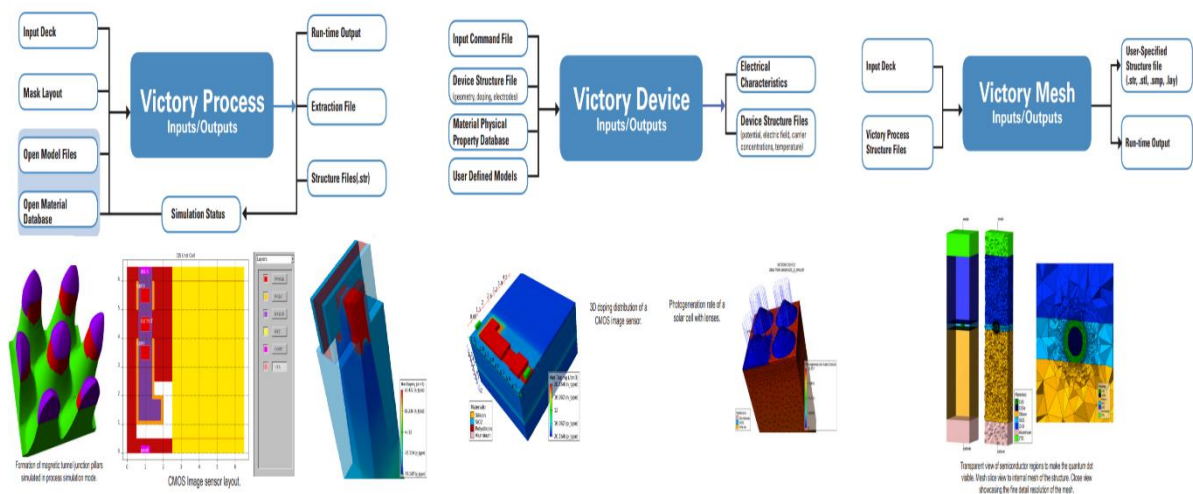


Figure 2-1: Schematic of the output structures generated by victory process, victory device and victory mesh modules of silvaco TCAD tool.

### 2.1.2: SENTAURUS TCAD

It is an advanced semiconductor device simulator that supports multidimensional (1D/2D/3D) device simulation developed by Synopsys. It can simulate the optical, electrical and thermal behaviour of the devices. The semiconductor manufacturing industry widely adopts it to optimize the devices before fabricating them. Core functionality includes process simulation, process emulation, structure editing, device simulation, interconnect simulation and TCAD to Spice and are depicted in Fig. 2-2. It is paid software. Therefore, users need to get a legal license from Synopsys to carry out research and development activities using the Sentaurus tool (Sentaurus 2021).

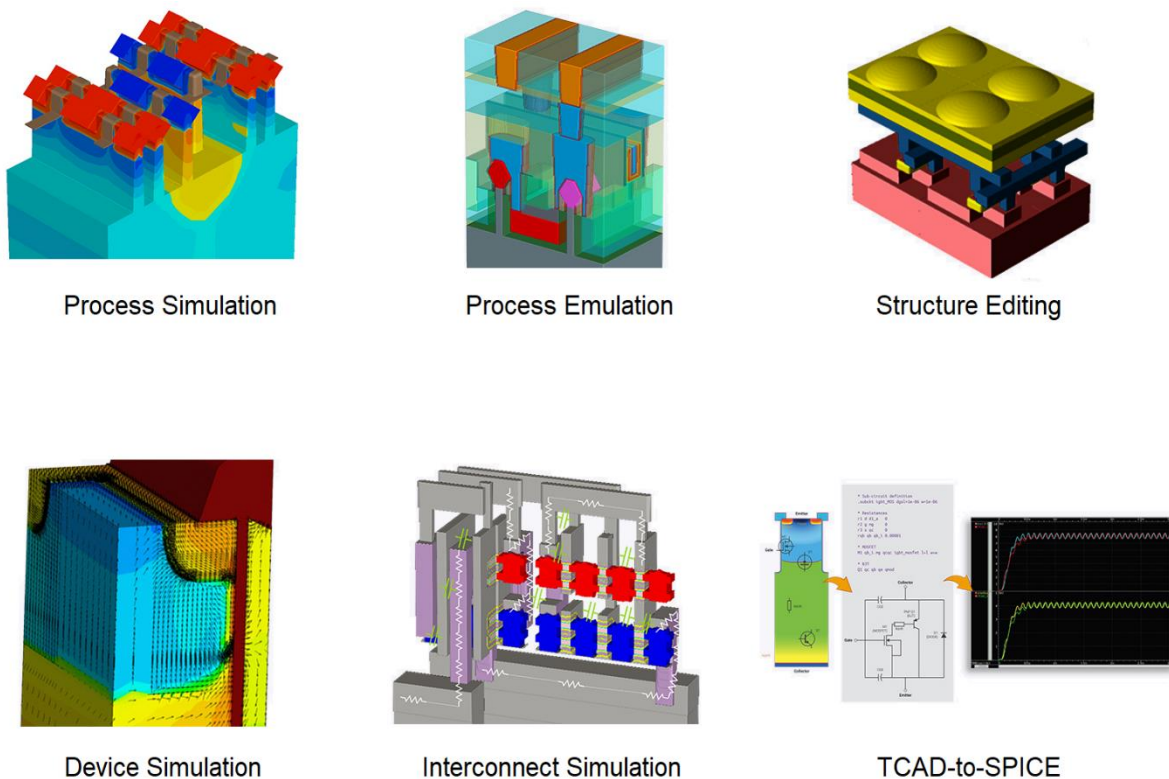


Figure 2-2: Schematic of the output structures generated by process, device and structure editing modules of SENTAURUS TCAD tools.

### 2.1.3: AFORS-HET

AFORS-HET is an open-source software tool designed for the simulation and measurements of solar cells [63]. It is originated from Helmholtz-Zentrum Berlin für Materialien und Energie, Berlin, Germany. AFORS-HET stands for Automat for Simulations of Heterostructures. This tool is effective but only limited to the 1D modelling of semiconductor materials and their interfaces layer by layer. It supports different functionality such as DC, AC, transient, optical, interface, boundary, and layer. It also supports tunnelling phenomena. The main interface window is displayed below in Fig. 2-3. This is the first window that appears after clicking right on the software icon. This window is locked initially and gets activated for the required calculations only after defining the structure (Stangl, Leendertz et al. 2010, Varache, Leendertz et al. 2015).

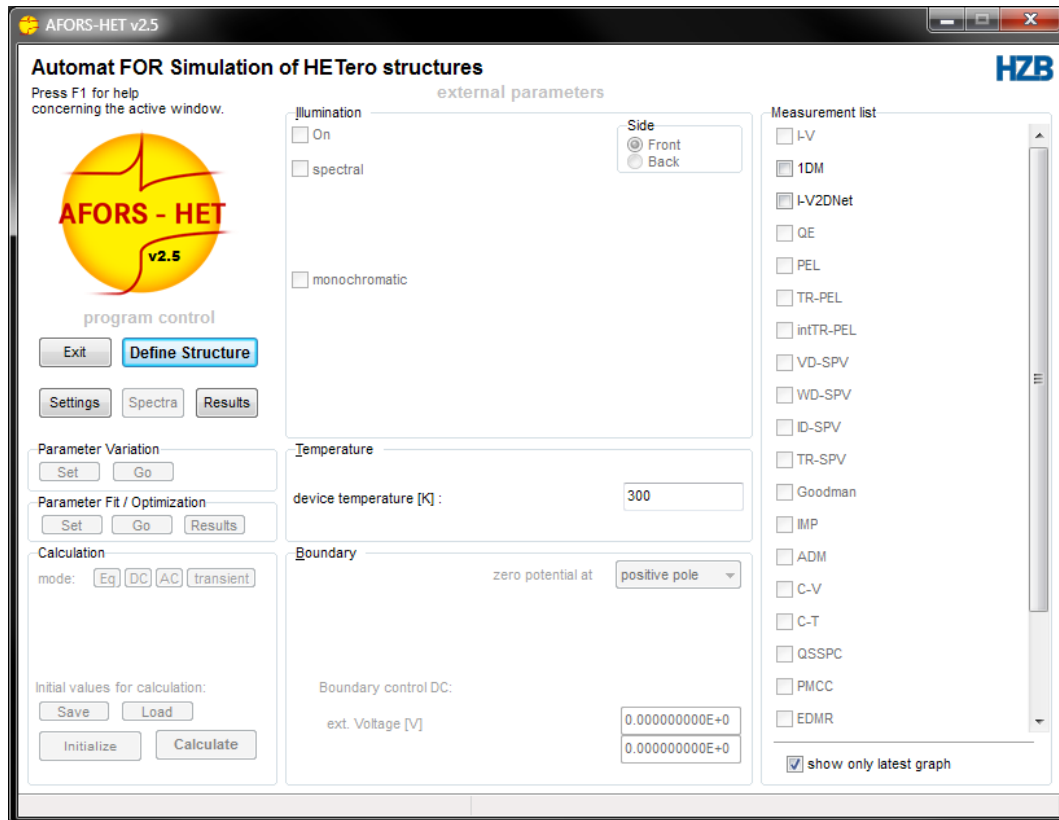


Figure 2-3: The main user interface of the AFORS-HET solar cell simulator.

### 2.1.4: SETFOS

SETFOS is a simulation software developed for organic and perovskite-related solar cells and light-emitting diodes (LEDs). FLUXiM AG, Switzerland, develops it. Different models that SETFOS supports is shown in Fig. 2-4. It supports coherent/incoherent optical layers, absorption profile and layer-specific absorption. It also supports drift-diffusion of electronic, excitons, ion, recombination, and tandem devices. Advanced optics are also supported, such as ray scattering, interference, Mie particles, Birefringence, Quantum dot down conversion. The emission model contains coherent/incoherent layers, spectral emission, mode analysis and quenching. Multithreading is also supported to ensure high-speed computation. Fitting and optimization algorithms are included. It is paid software. Therefore, users need to get a legal license from FLUXiM AG to conduct research and development activities using the SETFOS tool (Fluxim 2021).

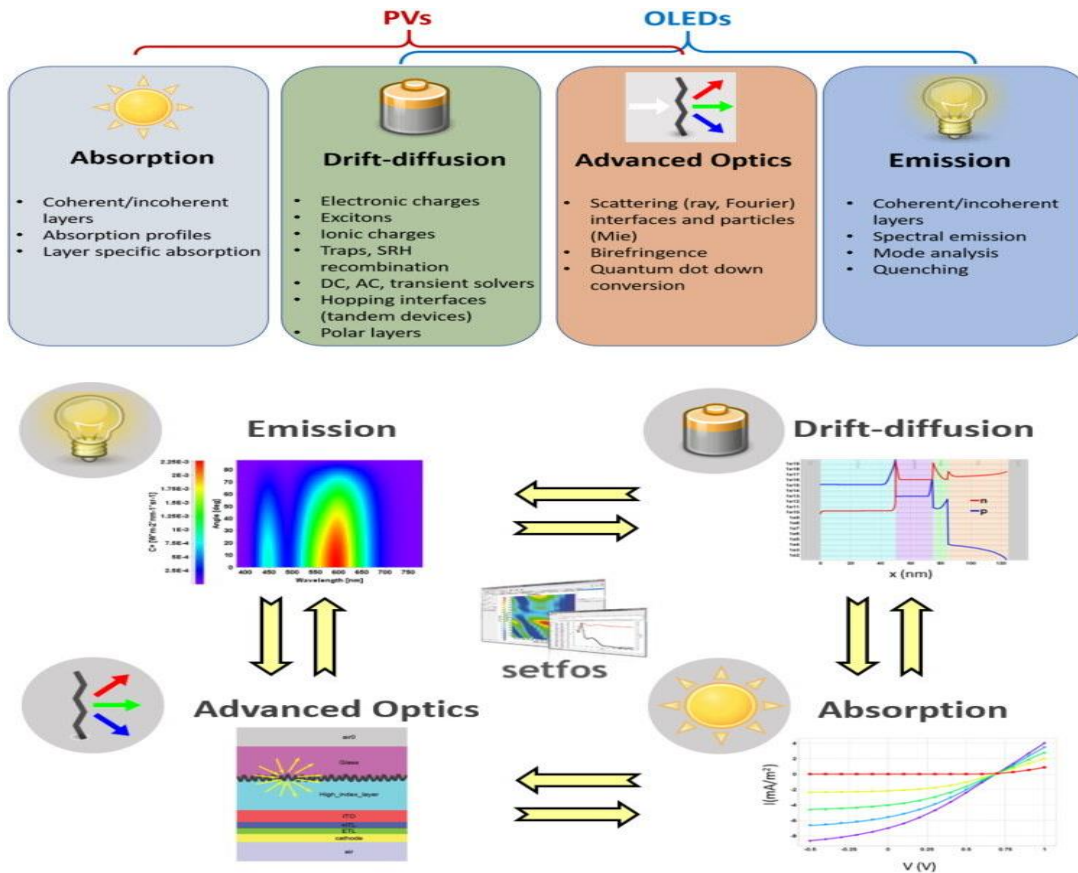


Figure 2-4: Schematic representation of different models, features, structures and results generated by SETFOS.

### **2.1.5: SCAPS-1D**

SCAPS-1D is a one-dimensional simulator equipped with advanced features to simulate solar cell devices to predict optoelectronic performance. It is developed at the Department of Electronics and Information Systems (ELIS) of the University of Gent, Belgium. This program was initially developed for cadmium telluride (CdTe), copper indium selenide (CuInSe<sub>2</sub>) and families-based devices; however, from time to time, the addition of advanced features also allowed its application for c-Si, gallium arsenide (GaAs) and amorphous silicon solar cell (a-Si) etc. Some of the main features of the SCAPS-1D is provided below (Burgelman, Nollet et al. 2000).

- Support a maximum of seven semiconducting layers.
- A compound semiconductor with different composition can be defined, and all the optoelectrical parameters can be graded as per the composition.
- Supports bulk and interface defect definition.
- Inter and Intra band tunnelling is also supported
- Shockley read hall (SRH), Auger and Radiative recombination models are supported.
- Batch execution for parametric variation and optimization is also supported.
- Analytical model for optical absorption.
- Supports current density-voltage (J-V), capacitance-voltage (C-V), capacitance-frequency (C-F) and external quantum efficiency (EQE) analysis for the device.
- Contains different panels for visualization of the results on the go.
- Support curve fitting
- Supports scripting features to define and run the problem.

SCAPS-1D is an open-source software tool obtained by writing a request to its developer Prof Marc Burgelman. Therefore, considering the open-source nature, advanced features, and user-friendly interface, SCAPS-1D has been considered throughout this thesis to perform the solar cells' simulation analysis and complete the objectives. The following section provides a brief overview of different features available in SCAPS-1D.

## 2.2: FEATURES OF SCAPS-1D

### 2.2.1: ACTION PANEL

As shown in Fig. 2-5, the action panel is the first window that appears after executing the scaps.exe file installed on the PC. The central panel consists of different options highlighted with the number that starts from 2 since number 1 is already assigned to the main action panel. The user initially needs to click on the set problem (2) to define the entire structure. After that, initial working points (3) can be defined in terms of temperature, voltage, frequency and number of points. This section also allows introducing series and shunt resistance to the solar cell being simulated using the tool. Criteria for solar illumination or dark simulation can also be activated using this section. After defining the problem using the set problem and selecting the initial conditions, the user needs to visit the action setting (4) to select the one or more desired analyses, including current-voltage (J-V), capacitance-voltage (C-V), capacitance frequency (C-f) and external quantum efficiency (EQE). The initial and final values for sweeping the parameter can also be set along with incremental steps in terms of the number of points using the action setting panel (4). (Burgelman, Decock et al. 2016)

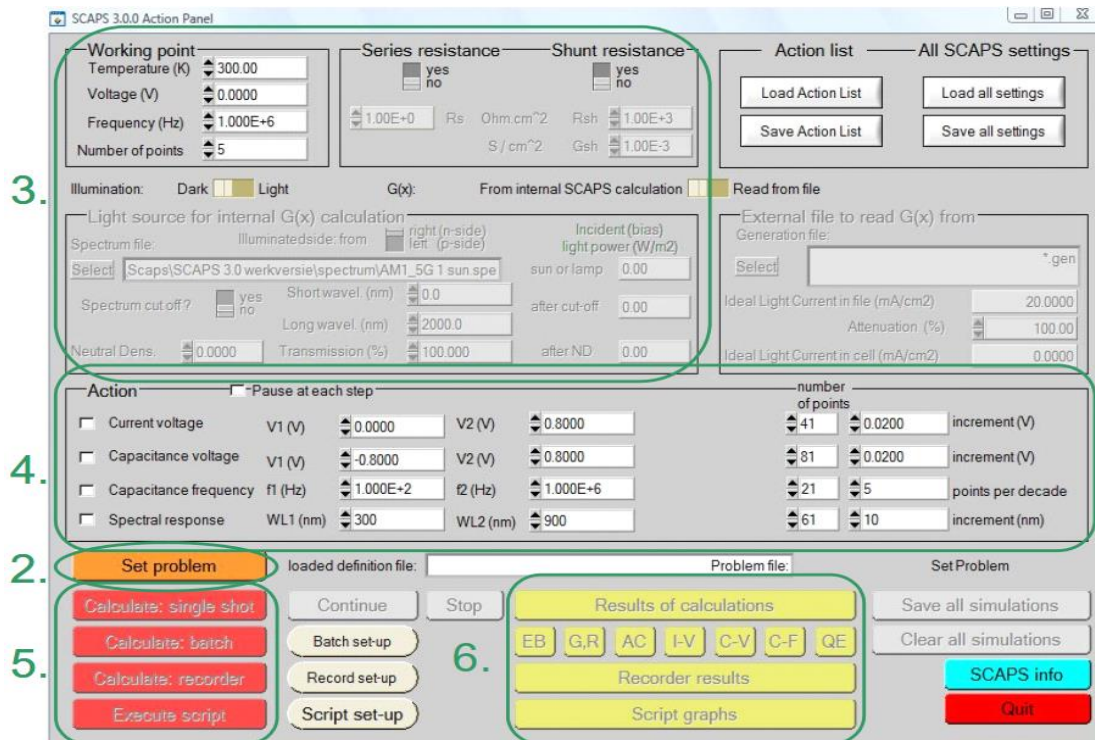


Figure 2-5: The main user interface of the SCAPS-1D solar cell simulator.

After doing all the steps till point 4, the user can set a model for calculation which includes different options such as single shot, batch, recorder and script execution. Once all the steps till point 5 are completed, the stored results can be viewed by using the results of the calculation panel (6).

### 2.2.2: SOLAR CELL DEFINITION AND LAYER EDITING

After clicking the set problem option, a window shown in Fig. 2-6 appears, which allow us to add different semiconducting layers. This panel also helps us in visualizing the schematic of the device structure defined, load previously defined structure, saving the current structure. After opening this panel, the user needs to click on add layer option to start creating the desired solar cell device. This panel supports a maximum number of 7 layers during structure definition. Once the user starts adding different layers, the information available on these panels gets updated, as shown in Fig. 2-7, which shows an example file created using three layers and corresponding device structure. Users can also select the desired direction for illumination, applied voltage and invert the structure as and when required. Users can duplicate, split and remove any layer created in this panel, as shown in Fig. 2-8. (Burgelman, Decock et al. 2016)

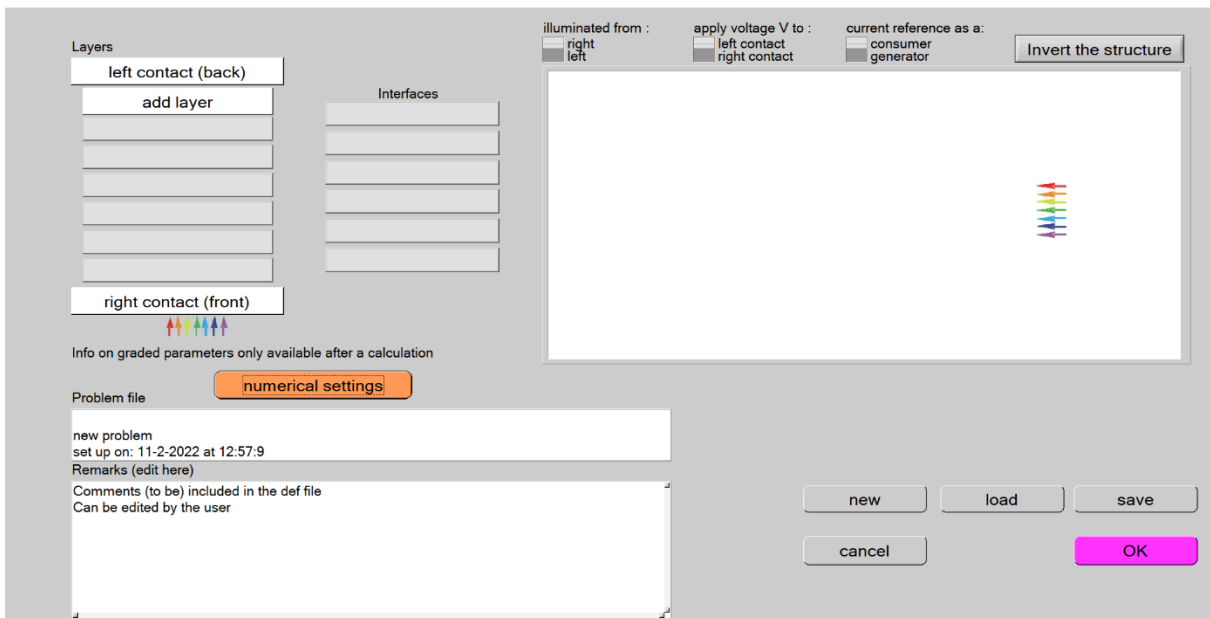


Figure 2-6: SCAPS-1D user interfaces for layer editing and solar cell definition (part 1).

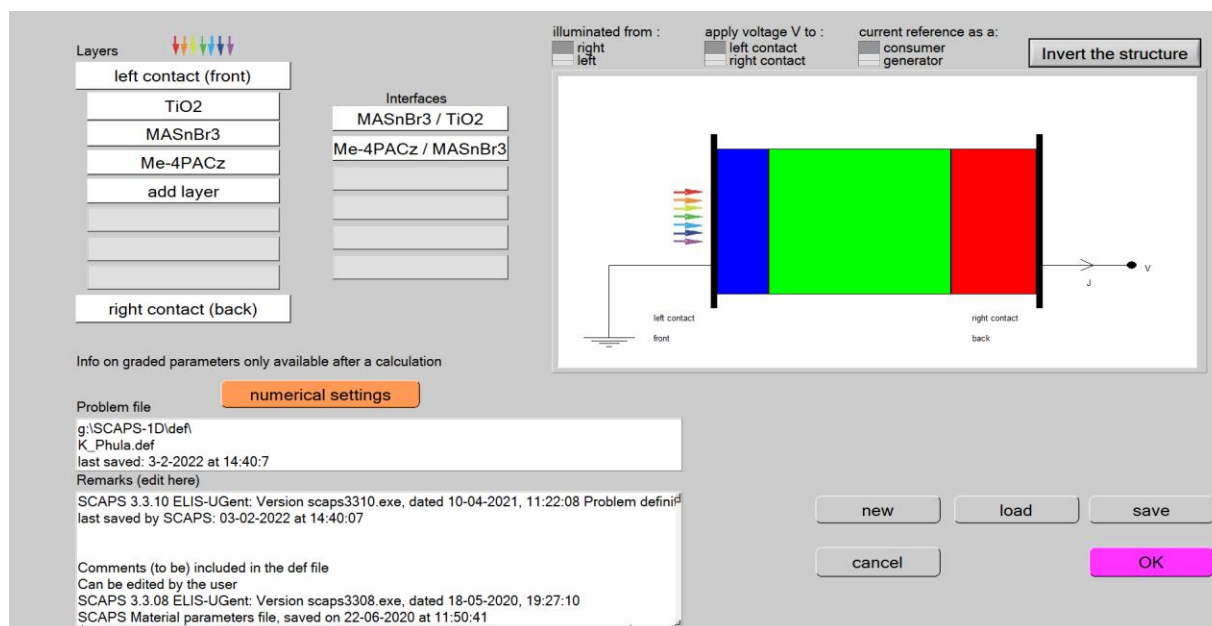


Figure 2-7: SCAPS-1D user interfaces for layer editing and solar cell definition (part 2).

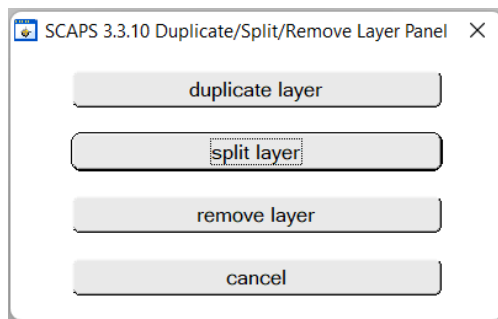


Figure 2-8: SCAPS-1D user interface for deleting, splitting and removing a layer.

### 2.2.3: CONTACT PROPERTIES

After creating the device structure with the help of layer definition, it is important to define some properties for the front and back electrodes/contacts. The contacts allow the extraction of light generated electron-hole pairs in the external circuit, and they can make an Ohmic or Schottky contact with the active layer laying below. In a thin-film solar cell, at least one transparent electrode is required to ensure optical coupling of incident photons. Therefore, the transparency of contact for optical radiation can also be selected from the contact panel, as shown in Fig. 2-9. Users can also select and decide the type of contact, i.e., either Ohmic (flat bands) or Schottky with some barrier height. This panel also allow the tuning of the work

function for the contacts and contact tunnelling from the active layer to contact. (Burgelman, Decock et al. 2016)

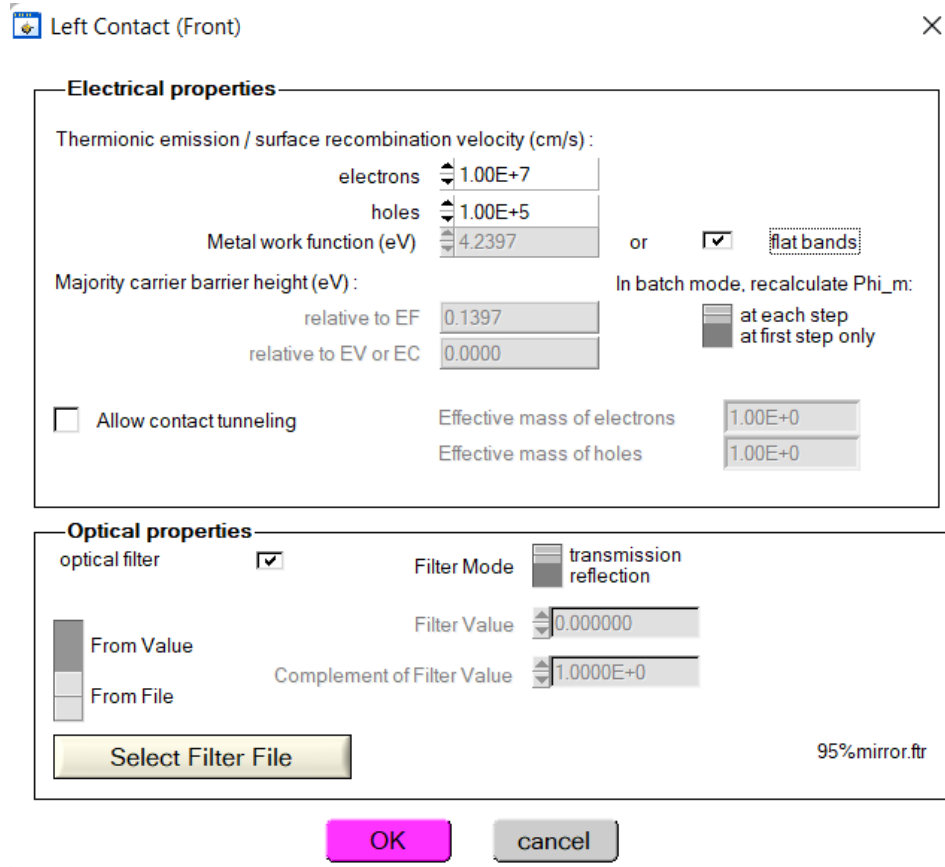


Figure 2-9: SCAPS-1D user interface for defining the properties for the contact.

### 2.2.4: LAYER PROPERTIES AND SAVE A MATERIAL

It is very important to edit the electrical as well optical properties of a layer after adding the layer to ensure the accurate simulation for predicting the performance. The material properties can be obtained from literature and can be supplied using this panel shown in Fig. 2-10, which is activated after clicking the desired layer. Electrical properties in terms of band gap, affinity, dielectric contact, conduction and valence band density of state, thermal velocity, mobility, effective tunnelling mass, doping can be adjusted using. Coefficients for the recombination model and bulk defect density can also be supplied using this interface. The panel also allow us to select the absorption coefficient file either from an external source or through inbuilt optical models. After inserting the desired properties, the user can save the material using the

save material option. Already defined material saved in the library of SCAPS-1D can also be invoked using the load material option. Once all the parameters are inserted, the user needs to click accept in order to return to the previous option. (Burgelman, Decock et al. 2016)

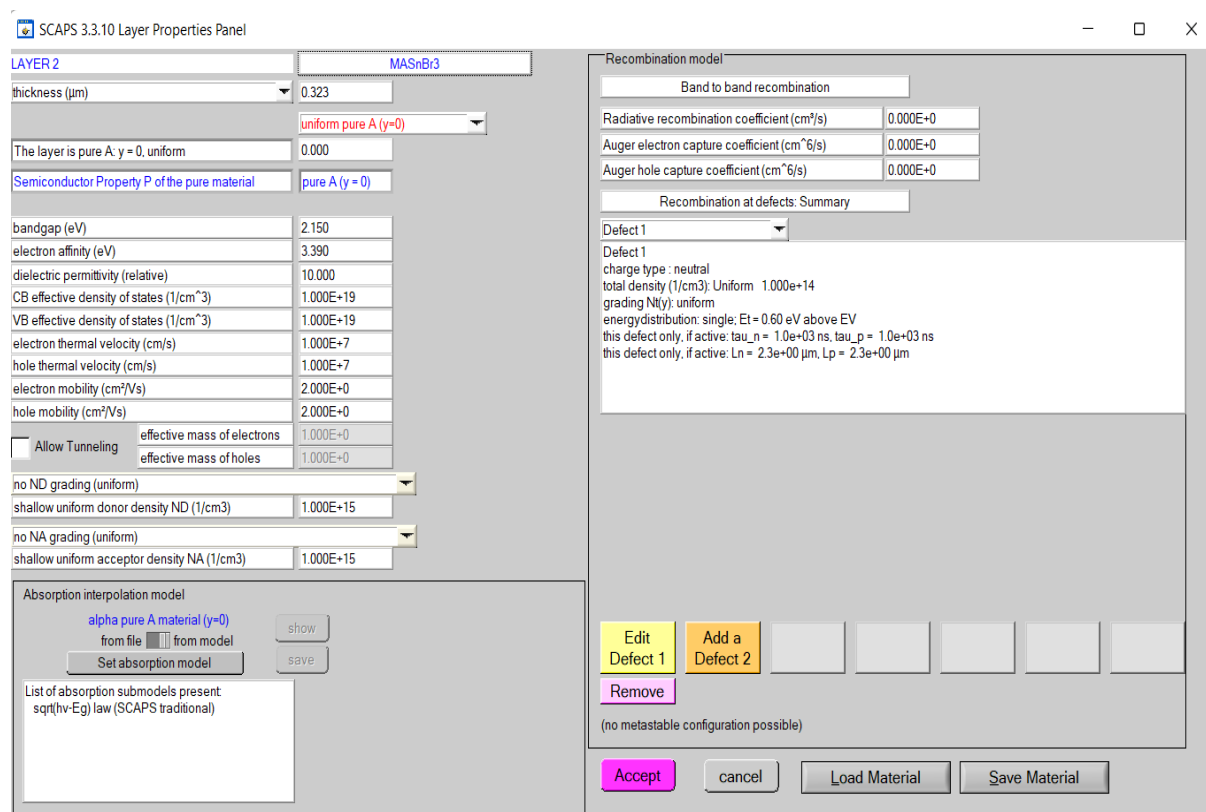


Figure 2-10: SCAPS-1D user interface for adding the optical and electrical properties for different layers.

### 2.2.5: OPTICAL MODELS

Inbuilt optical properties model can be activated by using the material properties panel shown in the previous subsection and once activated. It allows the selection of different models to generate the wavelength-dependent absorption coefficient for a particular material. Generated absorption coefficient data is further utilized in order to solve the optical performance of the device. It supports six different optical models where one or more models can be selected by the user to model the desired optical properties. Fig. 2-11 shows the option from where these inbuilt models are activated along with the formula for different optical models and an example of absorption coefficient data generated by utilizing the SCAPS-1D optical model. (Burgelman, Decock et al. 2016)

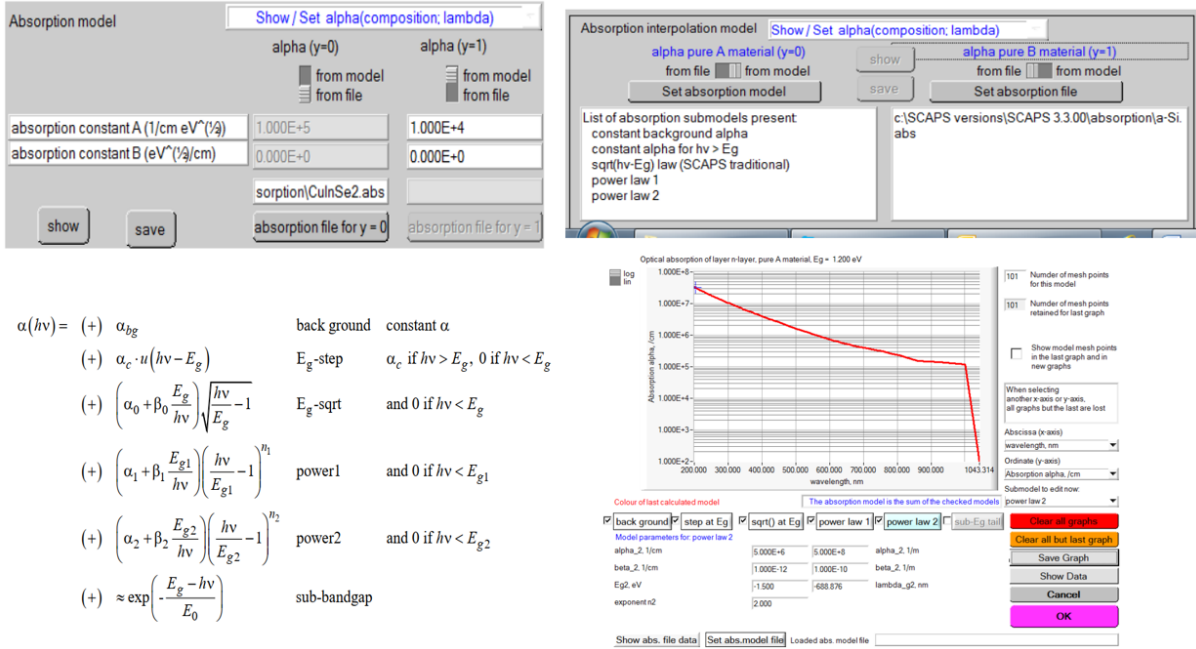


Figure 2-11: SCAPS-1D user interface for selecting the optical models for a particular layer.

### 2.2.6: TUNNELLING

Tunnelling is a phenomenon where an electron/hole can tunnel through a potential barrier. In semiconductor devices, two types of tunnelling phenomena commonly observed is inter band tunnelling, also known as band-to-band tunnelling, as shown in Fig. 2-12 and intra band tunnelling, as shown in Fig. 2-13. Both types of tunnelling are supported in SCAPS-1D, where interband tunnelling can be activated using the layer properties option, and intra band tunnelling can be activated using interface properties, as shown in Fig. 2-6 of section 2.2.2. (Burgelman, Decock et al. 2016)

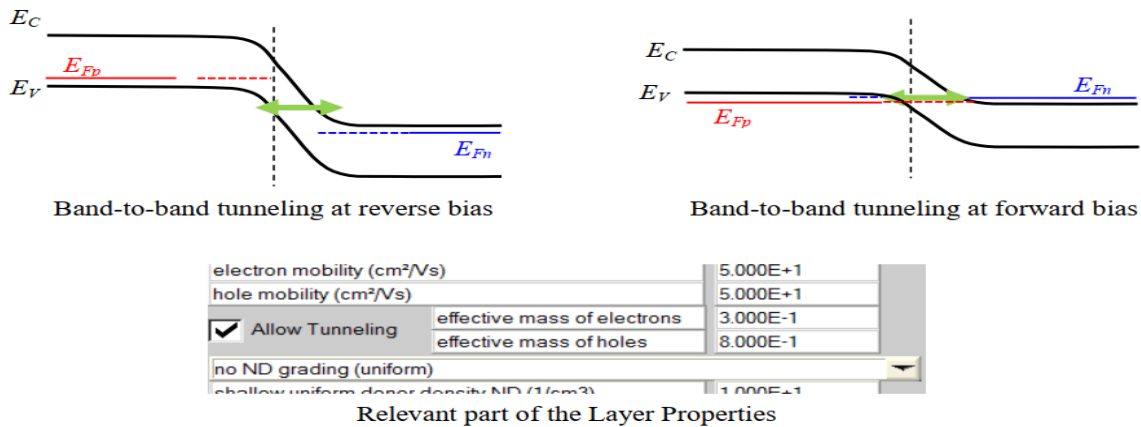


Figure 2-12: SCAPS-1D user interface for activating the band-to-band tunnelling.

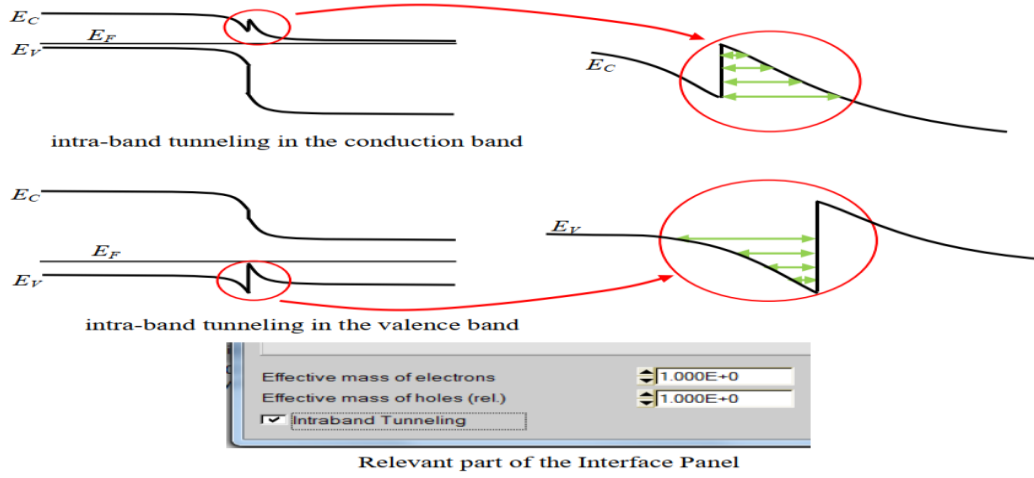


Figure 2-13: SCAPS-1D user interface for activating the interface or intra-band tunnelling.

## 2.2.7: OPTICAL MODELS AND FUNDAMENTAL SEMICONDUCTOR EQUATIONS IN SCAPS-1D.

SCAPS-1D utilizes different equations to solve the optical generation and to obtain the current density voltage curve. The equations are summarized below (Burgelman, Decock et al. 2016).

### 2.2.7.1: Optical Model

$$N_{phot}(\lambda, x) = N_{pho0}(\lambda) \cdot T_{front}(\lambda) \cdot \exp(-x \cdot a(\lambda)) \times \left( \frac{1 + R_{back}(\lambda) \cdot \exp(-2(d-x) \cdot a(\lambda))}{1 - R_{back}(\lambda) \cdot R_{int} \cdot \exp(-2d \cdot a(\lambda))} \right)$$

$$G(\lambda, x) = a(\lambda) \cdot N_{phot}(\lambda, x)$$

$$G(x) = \int_{\lambda_{min}}^{\lambda_{max}} G(\lambda, x) d\lambda = \int_{\lambda_{min}}^{\lambda_{max}} a(\lambda) \cdot N_{phot}(\lambda, x) d\lambda$$

Where,  $N_{phot}(\lambda, x)$  is the photon flux at each position in the layer,  $N_{pho0}(\lambda)$  is the incident photon flux,  $T_{front}(\lambda)$  is the transmission of the front contact,  $a(\lambda)$  is the absorption

coefficient,  $R_{int}$  is the internal reflection at the front contact (default value 0 is used),  $R_{back}(\lambda)$  is the reflection at the back contact (default value 0 is used),  $d$  is the layer thickness,  $x$  is the position in the layer, and  $G(x)$  is the generation rate of electron-hole pairs. This model includes only reflection/ transmission at two contacts and the absorption in the semiconducting layer. It does not incorporate the scattering, interference and intermediate reflections.

### 2.2.7.2: One-dimensional semiconductor equations

$$\frac{\partial}{\partial x} \left( \varepsilon_0 \varepsilon \frac{\partial \Psi}{\partial x} \right) = -q \left( p - n + N_D^+ - N_A^- + p_t - n_t \right)$$

$$J_n = -\frac{\mu_n n}{q} \frac{\partial E_{Fn}}{\partial x}$$

$$J_p = +\frac{\mu_p p}{q} \frac{\partial E_{Fp}}{\partial x}$$

$$-\frac{\partial J_n}{\partial x} - U_n + G = \frac{\partial n}{\partial t}$$

$$-\frac{\partial J_p}{\partial x} - U_p + G = \frac{\partial p}{\partial t}$$

Where  $q$  is the electronic charge,  $\Psi$  is electrostatic potential,  $p, n, p_t, n_t$  are the free hole, free electron, trapped hole and trapped electron, respectively.  $N_D^+, N_A^-$  is the ionized donor-like doping ionized acceptor-like doping concentration, respectively.  $\varepsilon$  is the permittivity and  $\varepsilon_0$  is the permittivity of free space,  $J_n$  is the electron current density,  $J_p$  is the hole current density,  $U_n$  is the electron recombination rate,  $U_p$  is the hole recombination rate,  $G$  is the generation rate,  $\mu_n$  is the electron mobility,  $\mu_p$  is the hole mobility,  $E_{Fn}$  is the electron quasi Fermi-level, and  $E_{Fp}$  is the hole quasi Fermi-level.

## 2.3: ADOPTED METHODOLOGY

The following Fig. 2-14 shows the methodology adopted in this thesis. Initially, literature is done to obtain the electrical and optical properties for the materials under consideration. After that design of the solar cell is done in SCAPS-1D using the features discussed above. Results

are obtained after designing the cell, and interpretation has been made. Standalone as well as tandem simulations are carried out in this thesis to full fill all the objectives.

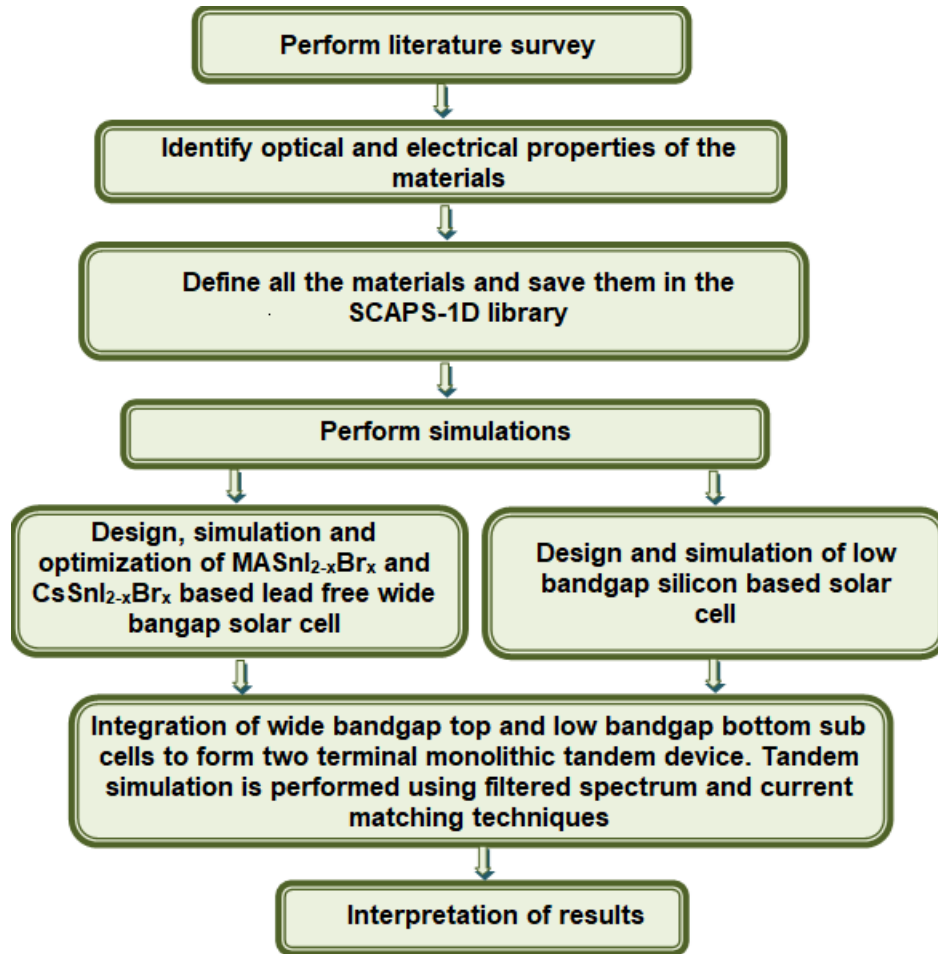


Figure 2-14: Flow diagram of the methodology adopted in this thesis.

## 2.4: SUMMARY

This chapter summarizes the importance of simulation related work in the field of the solar cell. List of the available paid and open-source software to perform the simulation related work for solar cells. In addition, all the features of SCAPS-1D, the software which is utilized in this thesis, are summarized in this chapter.

The next chapter is devoted to achieving the first objective stated in the introduction section, where a detailed simulation of tin-based halide, i.e., MASnI<sub>3-x</sub>Br<sub>x</sub> is provided.

## **2.5: REFERENCES**

- Burgelman, M., et al. (2016). "SCAPS manual." February.
- Burgelman, M., et al. (2000). "Modelling polycrystalline semiconductor solar cells." Thin Solid Films**361-362**: 527-532.
- Fluxim, A. (2021). Semiconducting thin film optics simulation software user manual, SETFOS.
- Sentaurus, T. (2021). "Manuals." Synopsys Inc., Mountain View, CA**94043**.
- Silvaco (2021). Athena User's Manual. Santa Clara, CA 95054, Silvaco.
- Stangl, R., et al. (2010). "Numerical simulation of solar cells and solar cell characterization methods: the open-source on demand program AFORS-HET." Solar Energy**14**: 319-352.
- Varache, R., et al. (2015). "Investigation of selective junctions using a newly developed tunnel current model for solar cell applications." Solar Energy Materials and Solar Cells**141**: 14-23.

# CHAPTER 3

---

---

## DESIGN, SIMULATION AND OPTIMIZATION OF LEAD-FREE METHYLAMMONIUM TIN HALIDES BASED SOLAR CELLS

---

---

The previous chapter summarizes the overview of different device simulators available for the simulation of solar cells. This chapter focused on designing and optimizing lead-free tin-based halide solar cells for environmentally friendly perovskite solar cell applications. Detailed motivation is provided in the introduction section (Sec. 3.1), followed by the device simulation and methodology section (Sec 3.2), which describes the details of device structure and material properties used during SCAPS-1D based device simulations. The findings are summarized in the results and discussion section (Sec 3.3).

### ***3.1: INTRODUCTION***

Decades ago, researchers focused on increasing the conversion efficiency of solar cells that serve as an alternative to traditional fossil fuels. With the growing demand for high conversion efficiency of solar cells, perovskite solar cells (PSCs) have gained notable attention due to their impressive features such as high absorption coefficient and low cost (Green, Ho-Baillie et al. 2014, Yin, Shi et al. 2014, Song, Chen et al. 2015, Razza, Castro-Hermosa et al. 2016, Petrus, Schlipf et al. 2017, Li, Zhang et al. 2018, Zhang, Bai et al. 2018, Velilla, Ramirez et al. 2019, Chen, Deng et al. 2021, Su, Málaga et al. 2021, Wang, Wang et al. 2021). The most commonly used perovskite on PSC applications is hybrid lead halide perovskite ( $\text{CH}_3\text{NH}_3\text{PbI}_3$ ) (Kojima, Teshima et al. 2009, Juarez-Perez, Wußler et al. 2014, Wehrenfennig, Liu et al. 2014). The basic structure of solar peroxide cells includes a perovskite layer, electron transport layer (ETL) and hole transport layer (HTL) (Schmidt, Larsen- Olsen et al. 2015, Ye, Sun et al. 2015). The PCE of lead-based PSCs has improved from an initial 3.8% to 25.2% (Kojima, Teshima et al. 2009, Chen, Wu et al. 2015, Bi, Tress

et al. 2016, Meng, Gao et al. 2016, Jeon, Na et al. 2018, Wang, Liu et al. 2019, Wang, Wang et al. 2021). However, recent research into this rapidly growing photovoltaic technology shows that there are certain limitations associated with Pb-based PSCs that are most effective. First, Pb-based PSCs (e.g., FAPbI<sub>3</sub>, MAPbI<sub>3</sub>) are toxic to the environment that has a detrimental effect on human, animal, and plant life (Giustino and Snaith 2016, Hong, Saparov et al. 2016, Hoefler, Trimmel et al. 2017, Lyu, Yun et al. 2017, Shi, Guo et al. 2017, Wang, Wang et al. 2019). Second, Pb-based PSCs are unstable due to environmental influences (humidity and oxygen) [28], heat stress [29] and mechanical weakness [30] etc.

These drawbacks have prompted a community of researchers working on photovoltaic technology to look for PSC that are stable, non-toxic and environmentally friendly. In this context, tin (Sn) based perovskite are investigated for better performance and stability. The improved performance was achieved using Sn-based perovskite absorbers due to their high optoelectronic properties (Umari, Mosconi et al. 2014). In addition, the Sn-based Perovskite shows high mobility and low optical band gap compared to lead-based halides (Hao, Stoumpos et al. 2014, Li, Zhang et al. 2019). The attractive structures of MASnI<sub>3-x</sub>Br<sub>x</sub> perovskite have led to significant developments in photovoltaic technology. Hao et al. (Hao, Stoumpos et al. 2014) compared PSCs with different absorbers and found a PCE of 5.23%, 5.48%, 5.73% and 4.27% with absorbers of MASnI<sub>3</sub>, MASnI<sub>2</sub>Br<sub>1</sub>, MASnI<sub>1</sub>Br<sub>2</sub> and MASnBr<sub>3</sub>, respectively. Another work, reported by Handa et al. (Handa, Yamada et al. 2017) in the PSC context using MASnI<sub>3-x</sub>Br<sub>x</sub> as an absorber layer shows a PCE of 1.10%.

However, apart from significant efforts by the researchers in developing Sn-based perovskite solar cells, the conversion efficiency is struggling to compete with that of conventional lead-based halide cells. Therefore, a detailed computational based study is much needed to perform the device simulations related to these Sn-based perovskite solar cells to optimize the performance and to improve the conversion efficiencies. The ongoing chapter of this thesis contributed to that field by designing and optimizing the Sn-based perovskite solar cells. The next section describes the details of the device structure, material properties and simulation methodology adopted used during SCAPS-1D based device simulations.

### **3.2: DEVICE STRUCTURE AND SIMULATION METHODOLOGY**

SCAPS-1D device simulator, as discussed in the previous chapter, is utilized to perform the device simulation for the devices under consideration. Four different Sn-based halides, such as  $\text{MASnI}_3$ ,  $\text{MASnI}_2\text{Br}_1$ ,  $\text{MASnI}_1\text{Br}_2$  and  $\text{MASnBr}_3$ , are considered for the device simulation, and their schematics are shown in Fig. 3.1 (a-d). For all the devices, fluorine-doped tin oxide (FTO) substrate has been utilized, and a 90 nm thick  $\text{TiO}_2$  layer which acts as an ETL, is deposited into it followed by deposition of the active layer, i.e.,  $\text{MASnI}_{3-x}\text{Br}_x$ . HTL layer of [4-(3,6-Dimethyl-9H-carbazol-9-yl)butyl] Phosphonic Acid (Me-4PACz) has been utilized for the collection of light generated holes, and the final device is completed by pasting gold contact on the top surface. The Sn-based halide structure with different composition ( $x=0, 1, 2$  and  $3$ ) is shown in Fig. 3-1 (a), (b), (c) and (d), respectively. The  $\text{MASnI}_3$ ,  $\text{MASnI}_2\text{Br}_1$ ,  $\text{MASnI}_1\text{Br}_2$  and  $\text{MASnBr}_3$  based perovskite solar cells are termed as D1, D2, D3 and D4 throughout this chapter.

The energy band diagrams have also been obtained for all the devices, i.e., D1, D2, D3 and D4 and shown in Fig. 3-2(a), (b), (c) and (d), respectively. It can be validated from the band diagram that is increasing the bromide composition increases the energy band gap for the perovskite absorber layer from 1.3 eV, 1.56 eV, 1.75 eV to 2.15 eV for  $\text{MASnI}_3$ ,  $\text{MASnI}_2\text{Br}_1$ ,  $\text{MASnI}_1\text{Br}_2$  and  $\text{MASnBr}_3$  based perovskite absorber layers.

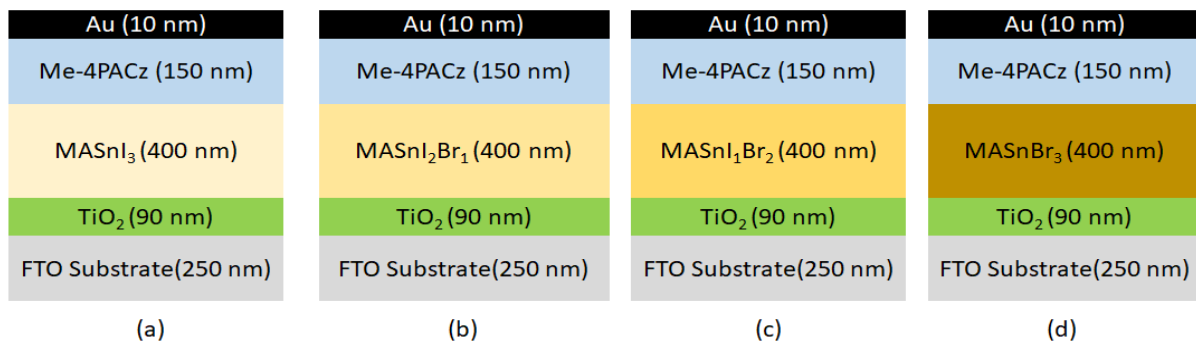


**Figure 3-1 Schematic device structures used during simulation for Sn-based perovskite solar cells having different iodine and bromine composition (a) D1, (b) D2, (c) D3 and (d) D4**

**CHAPTER 3: DESIGN, SIMULATION AND OPTIMIZATION OF LEAD-FREE METHYLAMMONIUM TIN HALIDES BASED SOLAR CELLS**

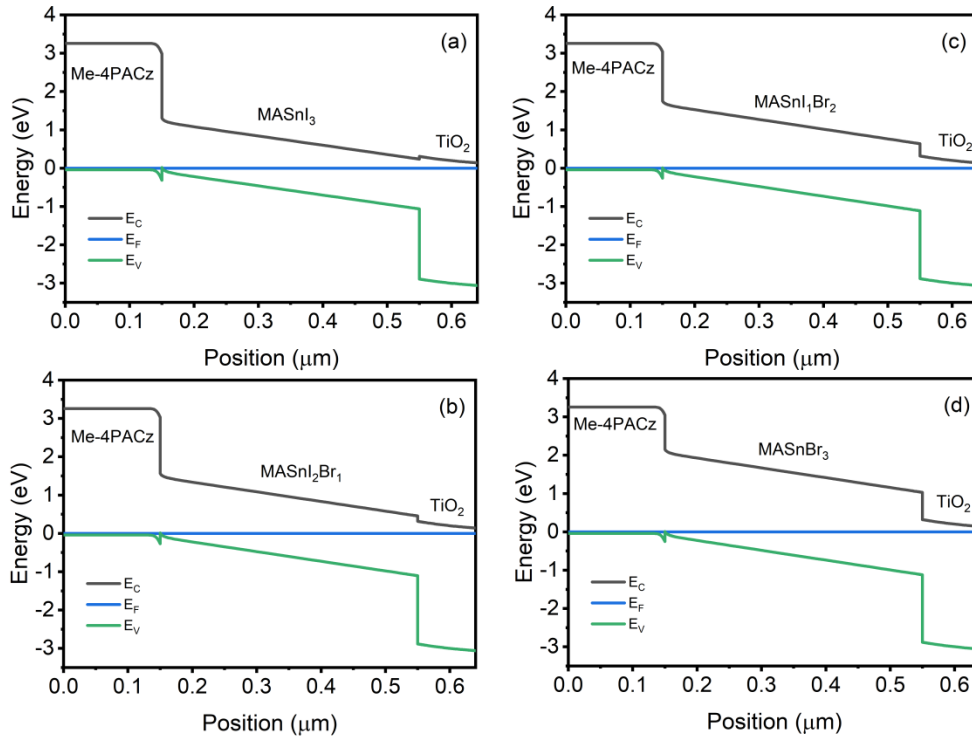


Figure 3-2 Energy band diagram for different Sn-based perovskite solar cells having different iodine and bromine composition (a) D1, (b) D2, (c) D3 and (d) D4. The data is obtained under thermal equilibrium.

Table 3-1 Material parameters used during simulation for Sn-based perovskite solar cells having different iodine and bromine composition (Al-Ashouri, Köhnen et al. 2020, Wang, Wang et al. 2021)

Material	TiO <sub>2</sub>	MASnI <sub>3</sub>	MASnI <sub>2</sub> Br <sub>1</sub>	MASnI <sub>1</sub> Br <sub>2</sub>	MASnBr <sub>3</sub>	Me-4PACz
<b>Parameter</b>						
<b>Bandgap (eV)</b>	3.20	1.3	1.56	1.75	2.15	3.3
<b>Electron affinity (eV)</b>	4.1	4.17	3.96	3.78	3.39	2.5
<b>Dielectric Permittivity</b>	9	10	10	10	10	10
<b>CB effective density of states (cm<sup>-3</sup>)</b>	2.2x10 <sup>18</sup>	1x10 <sup>19</sup>	1x10 <sup>19</sup>	1x10 <sup>19</sup>	1x10 <sup>19</sup>	1x10 <sup>19</sup>
<b>VB effective density of states (cm<sup>-3</sup>)</b>	1.8x10 <sup>19</sup>	1x10 <sup>19</sup>	1x10 <sup>19</sup>	1x10 <sup>19</sup>	1x10 <sup>19</sup>	1x10 <sup>19</sup>
<b>Electron mobility (cm<sup>2</sup>V<sup>-1</sup> s<sup>-1</sup>)</b>	4	2	2	2	2	5.0x10 <sup>1</sup>
<b>Hole mobility (cm<sup>2</sup>V<sup>-1</sup> s<sup>-1</sup>)</b>	4	2	2	2	2	5.0x10 <sup>1</sup>
<b>Donor density N<sub>D</sub> (cm<sup>-3</sup>)</b>	1x10 <sup>16</sup>	1x10 <sup>15</sup>	1x10 <sup>15</sup>	1x10 <sup>15</sup>	1x10 <sup>15</sup>	0
<b>Acceptor density N<sub>A</sub> (cm<sup>-3</sup>)</b>	0	1x10 <sup>15</sup>	1x10 <sup>15</sup>	1x10 <sup>15</sup>	1x10 <sup>15</sup>	2x10 <sup>18</sup>

**CHAPTER 3: DESIGN, SIMULATION AND OPTIMIZATION OF LEAD-FREE METHYLAMMONIUM TIN HALIDES BASED SOLAR CELLS**

**Table 3-2 Interface defect parameters used during simulation for Sn-based perovskite solar cells having different iodine and bromine composition.**

Interface	Me-4PACz/MASnI <sub>3-x</sub> Br <sub>x</sub>	MASnI <sub>3-x</sub> Br <sub>x</sub> /TiO <sub>2</sub>
<b>Parameters</b>		
<b>Capture cross section electrons (cm<sup>2</sup>)</b>	1x10 <sup>-19</sup>	1x10 <sup>-19</sup>
<b>Capture cross section holes (cm<sup>2</sup>)</b>	1x10 <sup>-19</sup>	1x10 <sup>-19</sup>
<b>Energy with respect to reference (eV)</b>	0.6	0.6
<b>Total density (integrated over all energies) (cm<sup>-2</sup>)</b>	1x10 <sup>10</sup>	1x10 <sup>10</sup>
<ul style="list-style-type: none"> <li>• For all the cases, the defect type is neutral with the single energetic distribution. The reference for defect energy level (E<sub>i</sub>) is above the highest E<sub>v</sub>.</li> <li>• For neutral defects, carrier lifetimes are determined using <math>\tau_n = 1/(\sigma_n v_{th} N_t)</math> and <math>\tau_p = 1/(\sigma_p v_{th} N_t)</math>. Where <math>\sigma_n, \sigma_p, v_{th}, N_t</math> are the electron capture cross-section, hole capture cross-section, thermal velocity (10<sup>7</sup> cm/s), and total defect density, respectively.</li> </ul>		

The material parameters used during simulations are summarized in Table 3.1, and considered values for interface defects are shown in Table 3.2. The neutral type bulk defect for the active layer is also considered for the active (perovskite) layer with an electron/hole capture cross-section of 1x10<sup>-15</sup> cm<sup>2</sup> having a defect density of 1x10<sup>15</sup> cm<sup>-3</sup> to account for bulk defect recombination. Standard AM1.5G spectrum has been utilized to illuminate the device and to obtain optoelectronic performances. The equation and coefficient utilized by SCAPS-1D to solve the device physics are also considered as reported in the previous chapter. Square root at E<sub>g</sub> model is utilized to generate the optical properties for the perovskite absorber layer.

### 3.3: RESULTS AND DISCUSSIONS

The performance of solar cells depends on the efficient utilization of the solar cell and the successful collection of light-generated charge carriers in the external circuits. Therefore, thickness and bulk defects in the absorber layer play a very crucial role in tuning the overall performance of the device. Increasing the thickness increases the photon absorption; however, it is also important that the carriers that are generated by enhanced absorption must get collected in the external circuit. Therefore, it is always required to have higher thickness with minimal defect density so that generated charge carriers can easily diffuse through the device

and make their path to the end electrodes. In addition, consideration of interface defects is also very important to obtain its impact on the performance. Since higher defect density would kill most of the light generated carriers within its vicinity, therefore, this entire result and discussion section are divided into seven different subsections from Sec. 3.1.1 to Sec. 3.1.7, where the collective influence of perovskite absorber layer thickness and bulk defect density to optimize the performance is reported followed by the impact of optical transparency of substrate and cathode work function on the PV performance of the optimized device.

### 3.1.1: Illuminated J-V data and photovoltaic performance for MASnI<sub>3</sub> based PSCs at different absorber layer thickness and bulk defects

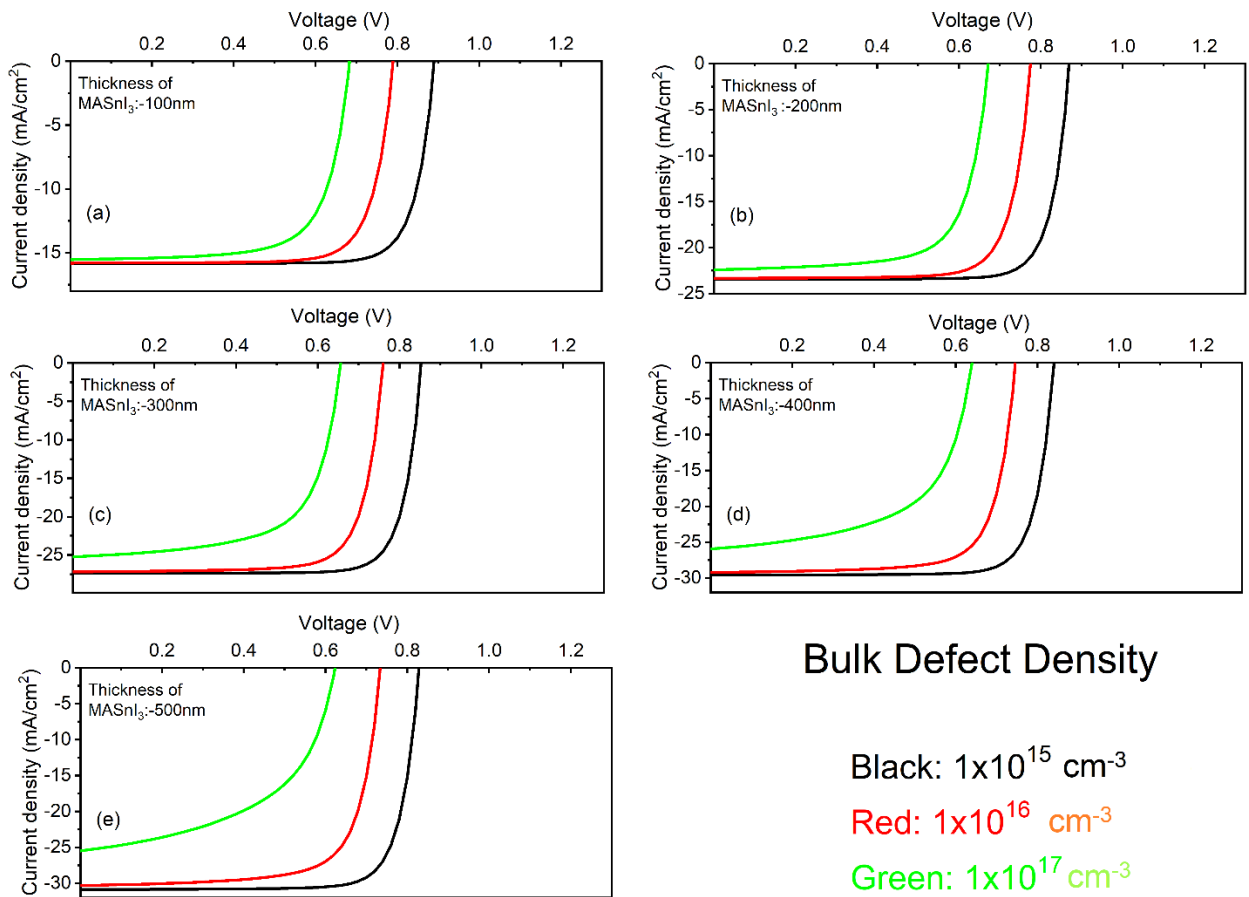


**Figure 3-3** The J-V parameters for distinct defect density of MASnI<sub>3</sub> perovskite in the range of  $1 \times 10^{15} \text{ cm}^{-3}$  to  $1 \times 10^{17} \text{ cm}^{-3}$  at various absorber layer thicknesses (a) 100 nm (b) 200 nm (c) 300 nm (d) 400 nm and (e) 500 nm.

This sub-section explores the defect density at different thicknesses for the lead-free perovskite solar cells, i.e.,  $\text{MASnI}_3$ , and its implications for photovoltaic performances. As Fig. 3-3 (a-e) shows, the device's performance with five distinct perovskite thicknesses, ranging from 100 nm to 500 nm. Precisely, at 100 nm of  $\text{MASnI}_3$  thickness, the defect density of  $\text{MASnI}_3$  is changed from  $1 \times 10^{15} \text{ cm}^{-3}$  to  $1 \times 10^{17} \text{ cm}^{-3}$  offering the  $J$ - $V$  curve as shown in Fig. 3-3 (a-e). It can be well predicted that the low defect density offers better output parameters, i.e., at a value of  $1 \times 10^{15} \text{ cm}^{-3}$ , the highest combination of  $J_{sc}/V_{oc}$ , i.e., 15.2 mA/cm<sup>2</sup>/ 0.9 Volt, 23.5 mA/cm<sup>2</sup>/ 0.86 Volt, 27.0 mA/cm<sup>2</sup>/ 0.85 Volt, 30.0 mA/cm<sup>2</sup>/ 0.82 Volt and 31.0 mA/cm<sup>2</sup>/ 0.81 Volt, respectively has been achieved at absorber layer thickness of 100 nm, 200 nm, 300 nm, 400 nm and 500 nm. While increasing the defect density, a low  $J_{sc}/V_{oc}$  value is observed. More specifically, at  $1 \times 10^{17} \text{ cm}^{-3}$ , it offers the  $J_{sc}/V_{oc}$ , i.e., 15.1 mA/cm<sup>2</sup>/ 0.7 Volt, 22.5 mA/cm<sup>2</sup>/ 0.64 Volt, 25.0 mA/cm<sup>2</sup>/ 0.625 Volt, 25 mA/cm<sup>2</sup>/ 0.62 Volt and 25.5 mA/cm<sup>2</sup>/ 0.61 Volt, respectively has been achieved at absorber layer thickness of 100 nm, 200 nm, 300 nm, 400 nm and 500 nm. The best performance has been obtained at an absorber layer thickness of 500 nm having a low defect density of  $1 \times 10^{15} \text{ cm}^{-3}$  with  $J_{sc}$  (31.0 mA.cm<sup>-2</sup>),  $V_{oc}$  (0.81 V) and Fill factor (FF) of 79.9%, which resulted in 20% PCE.

### **3.1.2: Illuminated J-V data and photovoltaic performance for $\text{MASnI}_2\text{Br}_1$ based PSCs at different absorber layer thickness and bulk defects**

Fig. 3-4 (a-e) shows the device's performance with distinct perovskite thicknesses, namely 100 nm and 500 nm, respectively. The defect density of  $\text{MASnI}_2\text{Br}_1$  is changed from  $1 \times 10^{15} \text{ cm}^{-3}$  to  $1 \times 10^{17} \text{ cm}^{-3}$  which offers the  $J$ - $V$  curve as shown in Fig. 3-4 (a-e). The  $V_{oc}$  of the PSCs has been shifted to the left as the defectivity increases, attaining a much smaller value of 1 Volt than 1.4 Volt for optimizing absorber thickness condition of 500 nm. As the smaller thickness of absorber layer, i.e., 100 nm, only obtains a much smaller  $J$ - $V$  value of 11 mA/cm<sup>2</sup> and 1.41 Volt, on the contrary, the 500

nm achieves a much-optimized value of 22.5 mA/cm<sup>2</sup> and 1.4 Volt respectively at low defectivity of 1×10<sup>12</sup> cm<sup>-3</sup> as shown from Fig. 3-4 (a-e). The best performance has been obtained at an absorber layer thickness of 500 nm, having a low defect density of 1×10<sup>15</sup> cm<sup>-3</sup> with J<sub>SC</sub> (22.3 mA.cm<sup>-2</sup>), V<sub>OC</sub> (1.07 V) and FF (81.7), which resulted in 19.4% PCE.

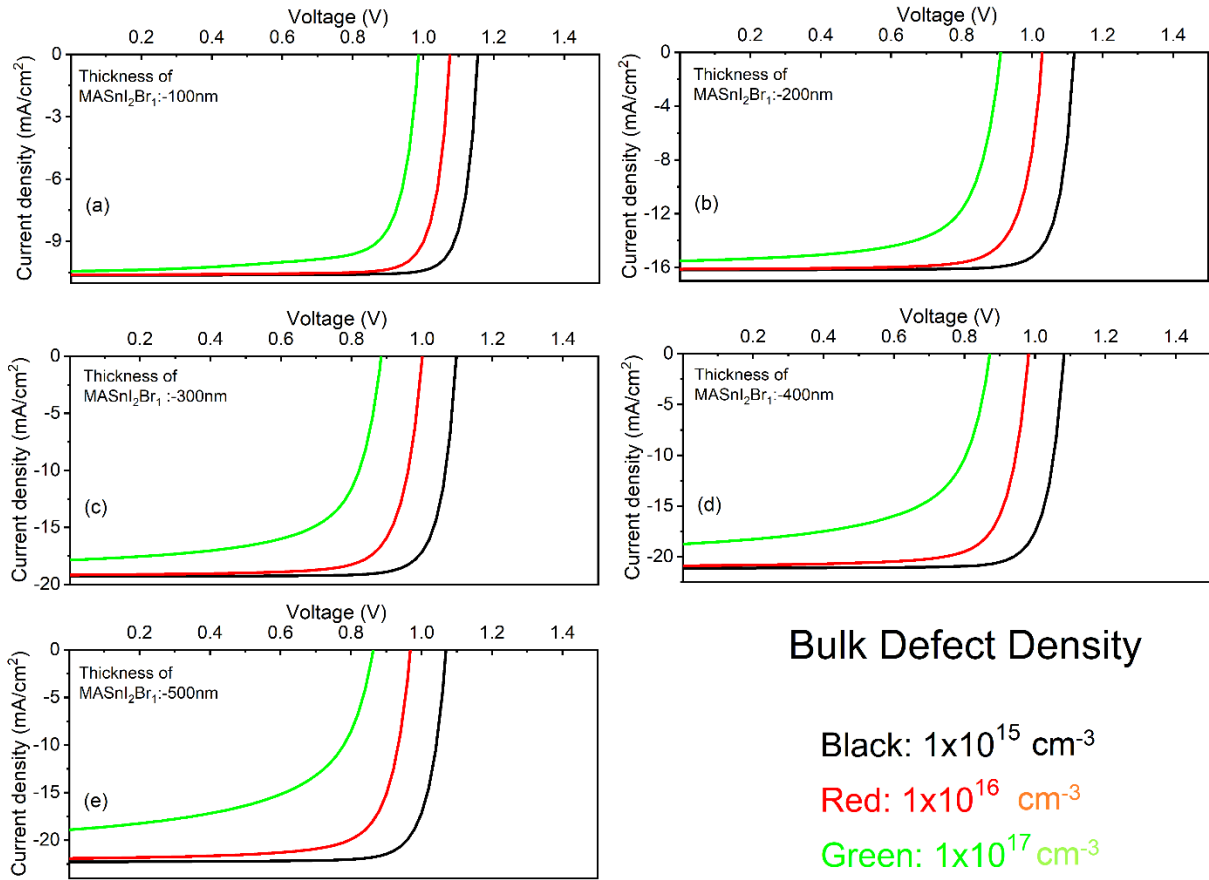


**Figure 3-4**The J-V parameters for distinct defect density of MASnI<sub>2</sub>Br<sub>2</sub> perovskite in the range of 1×10<sup>15</sup> cm<sup>-3</sup> to 1×10<sup>17</sup> cm<sup>-3</sup> at various absorber layer thicknesses (a) 100 nm (b) 200 nm (c) 300 nm (d) 400 nm and (e) 500 nm.

### 3.1.3: Illuminated J-V data and photovoltaic performance for MASnI<sub>1</sub>Br<sub>2</sub> based PSCs at different absorber layer thickness and bulk defects

The simulated photovoltaic parameters of  $J$ - $V$  have been investigated with varying defectivity of the perovskite layer concerning various absorber layer thicknesses. In Fig. 3-5(a-e), the impact of defect density of the perovskites in the range of  $1 \times 10^{15} \text{ cm}^{-3}$  and  $1 \times 10^{17} \text{ cm}^{-3}$  is shown for 100 nm – 500 nm thick  $\text{MASnI}_1\text{Br}_2$  based absorber layer. A similar mechanism is followed since the previous structures show decreasing trends over increasing defects. This implies that the highest  $J$ - $V$  parameter is obtained for the simulated thicknesses from 100 nm to 500 nm, having lower defect density. The highest  $J$ - $V$  of  $17 \text{ mA/cm}^2$  and 1.5 Volt is achieved for the  $\text{MASnI}_1\text{Br}_2$  at a thickness level of 500 nm with the lowest defect density. Whereas least  $J_{SC}$  of  $7.5 \text{ mA/cm}^2$  is obtained due to lesser absorption by the perovskite layer in the case of thin, i.e., 100 nm thick absorber layer as depicted in Fig. 3-5(a). The best performance has been obtained at an absorber layer thickness of 500 nm, having a low defect density of  $1 \times 10^{15} \text{ cm}^{-3}$  with  $J_{SC}$  ( $16.9 \text{ mA.cm}^{-2}$ ),  $V_{OC}$  (1.26 V) and FF (78.24), which resulted in 16.7% PCE.

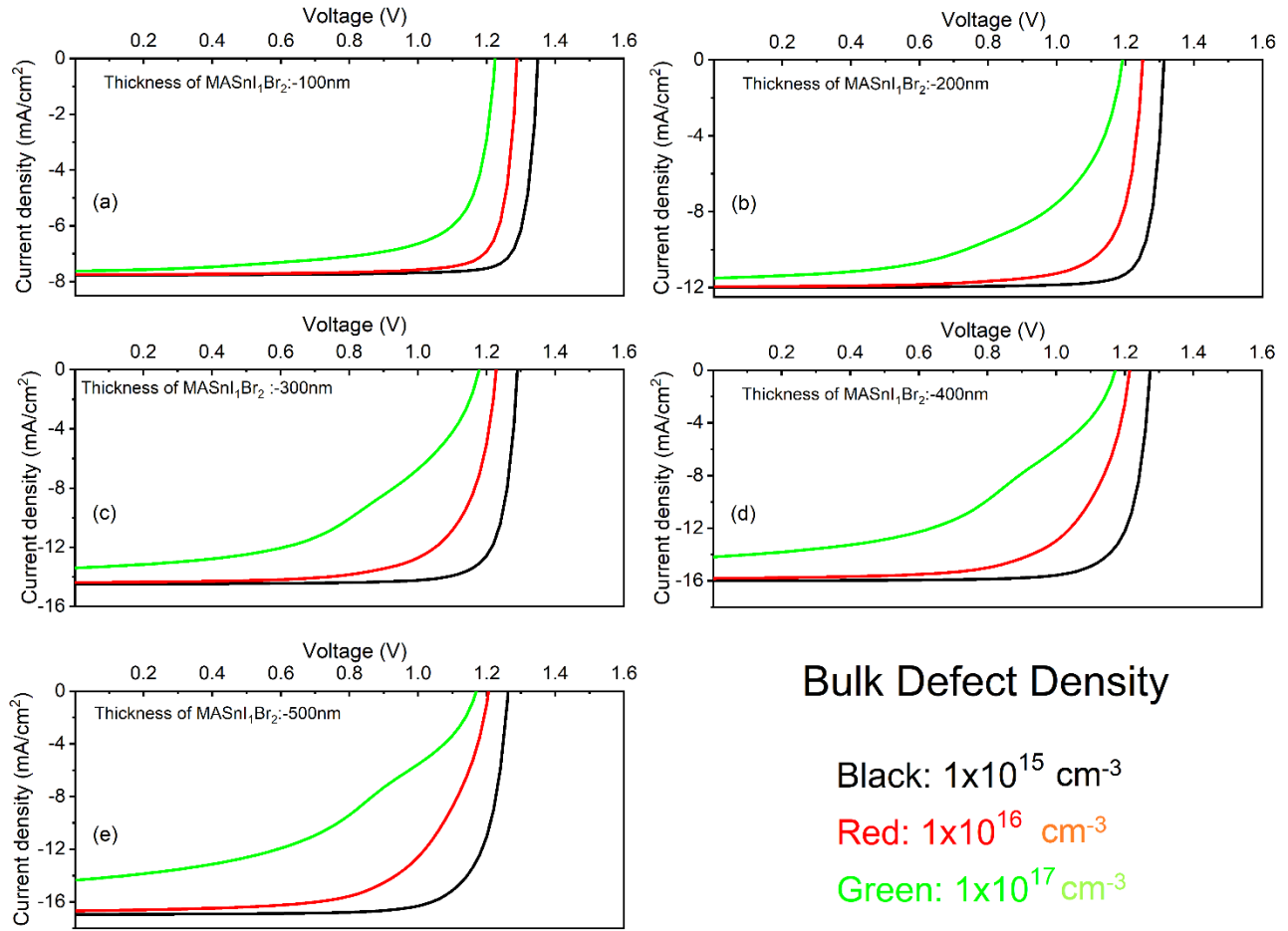


**Figure 3-5** The J-V parameters for distinct defect density of  $\text{MASnI}_1\text{Br}_2$  perovskite in the range of  $1 \times 10^{15} \text{ cm}^{-3}$  to  $1 \times 10^{17} \text{ cm}^{-3}$  at various absorber layer thicknesses (a) 100 nm (b) 200 nm (c) 300 nm (d) 400 nm and (e) 500 nm.

### 3.1.4: Illuminated J-V data and photovoltaic performance for $\text{MASnBr}_3$ based PSCs at different absorber layer thickness and bulk defects

The dependency of thicknesses over the device's performance with tin based pure bromide halide, from 100 nm and 500 nm, has been shown in Fig. 3-6(a-e). Furthermore, the defect density of  $\text{MASnBr}_3$  is altered similar as discussed in the previous subsections, i.e.,  $1 \times 10^{15} \text{ cm}^{-3}$  to  $1 \times 10^{17} \text{ cm}^{-3}$  at various absorber layer thicknesses from 100 nm - 500 nm, resulting in the J-V curve shown in Fig. 3-6. (a-e). Low defect density, for example, yields improved output parameters, with the maximum combination of PV parameters  $J_{\text{SC}}$  ( $9.06 \text{ mA.cm}^{-2}$ ),  $V_{\text{OC}}$  (1.41 V), FF

(69.6%) and PCE (8.97%). A low J-V value is observed by increasing defect density. It is noteworthy to mention that the increasing thickness with the lowest defect density of the perovskite layer improves the J-V parameter and the overall device outputs.

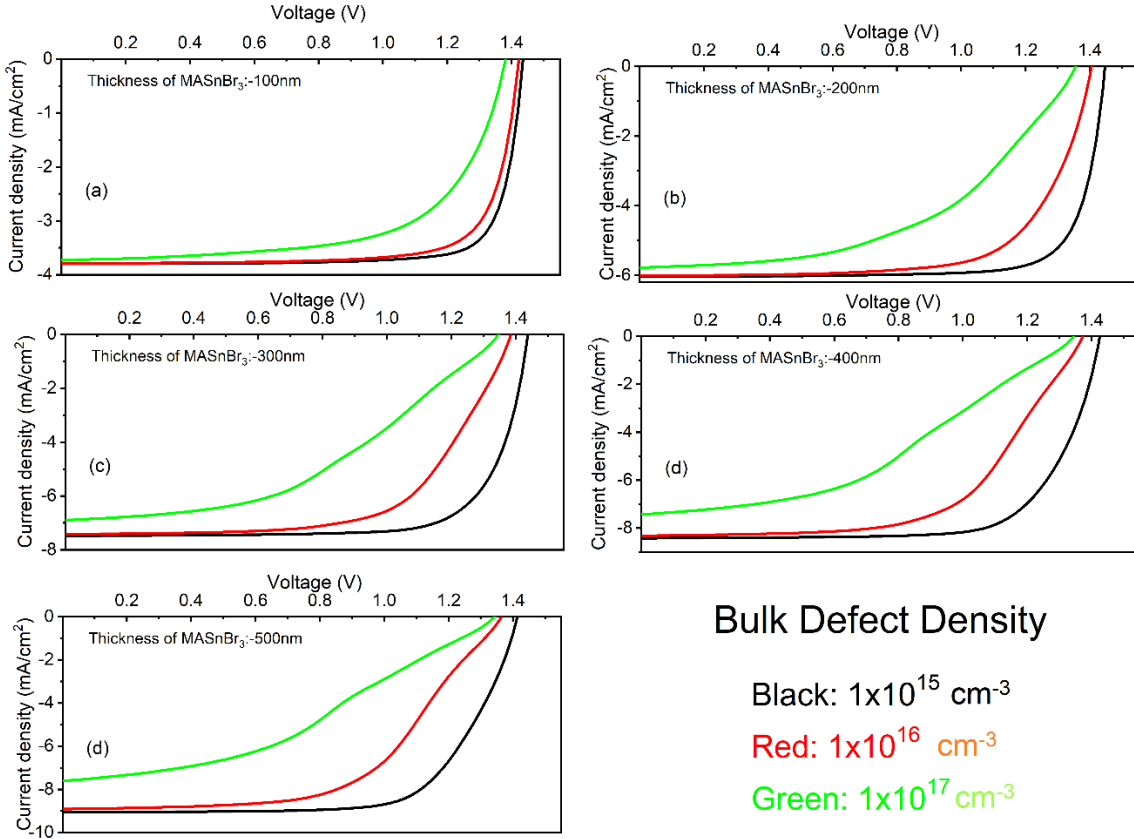


**Figure 3-6** The J-V parameters for distinct defect density of MASnBr<sub>3</sub> perovskite in the range of 1 × 10<sup>15</sup> cm<sup>-3</sup> to 1 × 10<sup>17</sup> cm<sup>-3</sup> at various absorber layer thicknesses (a) 100 nm (b) 200 nm (c) 300 nm (d) 400 nm and (e) 500 nm.

### 3.1.5: Comparison of PV performance among MASnI<sub>3</sub>, MASnI<sub>2</sub>Br<sub>1</sub>, MASnI<sub>2</sub>Br<sub>1</sub> and MASnBr<sub>3</sub> based perovskites.

Simulation results showed the highest performance in terms of conversion efficiency of 20% had been obtained with the D1 device, which includes pure iodide-based halide. Improvement is attributed to sufficient spectrum utilization compared to other devices, i.e., D2, D3 and D4. It is worth noting that increasing the bromide composition increases the band gap, and the same has been shown in Table 3-1. Higher band gap resulted in inferior performance in terms of J<sub>SC</sub> values, but the device also showed higher V<sub>OC</sub> due to larger band gap. Though improvement in V<sub>OC</sub> is unable

to mitigate the  $J_{SC}$  loss and hence hampers the overall conversion efficiency from 20% to 8.97% while moving from pure iodide to pure bromide-based Sn halide.

### **3.1.6: Impact of optical transparency of the substrate on the performance of $MASnI_3$ based device.**

The previous section showed that the highest conversion efficiency is obtained with pure iodide-based halide, i.e.,  $MASnI_3$ ; therefore, for further analysis related to substrate transparency and electrode work function, only  $MASnI_3$  is considered. The ongoing subsection provides a comprehensive study for the impact of substrate transparency on the performance of the device. The perovskite devices can be fabricated on a variety of substrates having optical transparency from 80%-95%. Therefore, it is important to investigate the impact of substrate transparency on the performance of the device. To perceive the same during simulation, the transparency of the substrate has been varied from 80%-95% and corresponding external quantum efficiency (EQE), current density-voltage curve (J-V) and PV parameters are provided in Fig. 3-7(a-b) and Fig. 3-8, respectively.

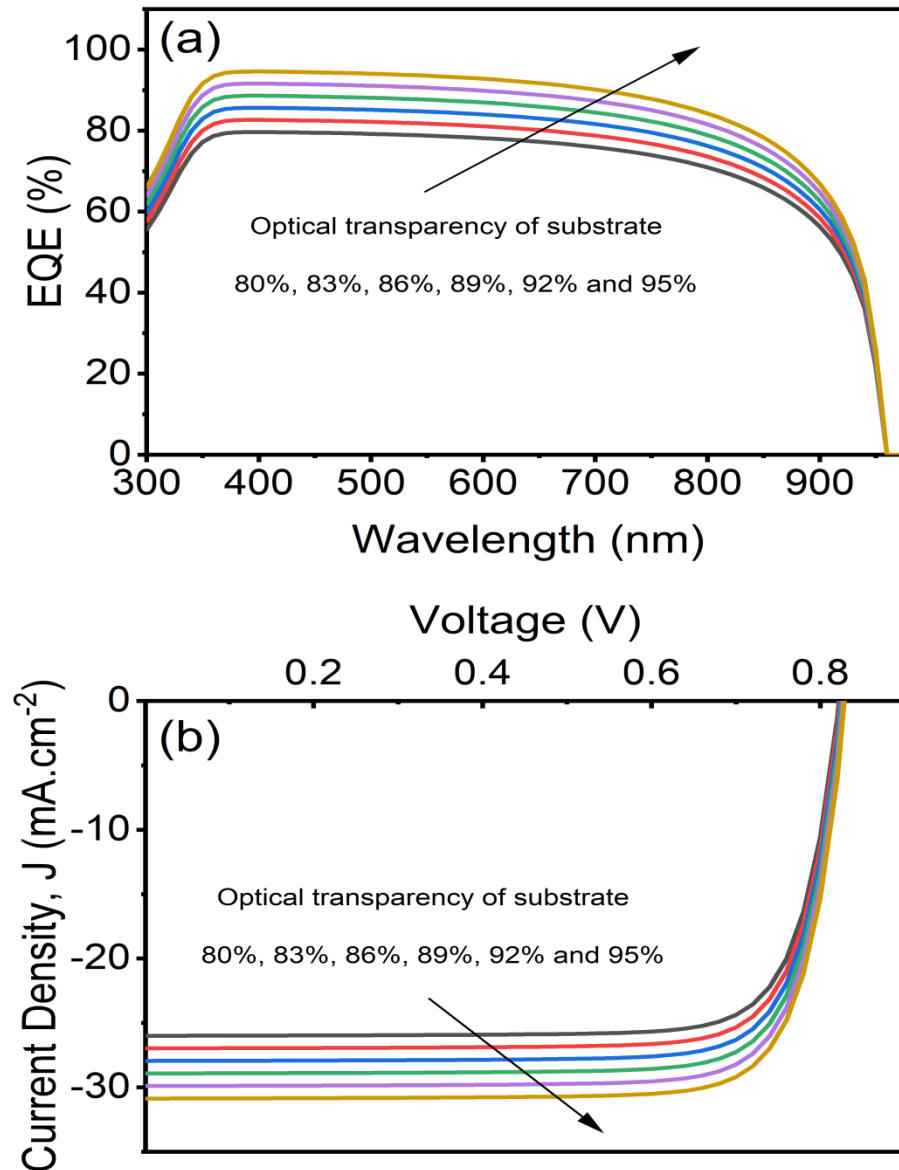
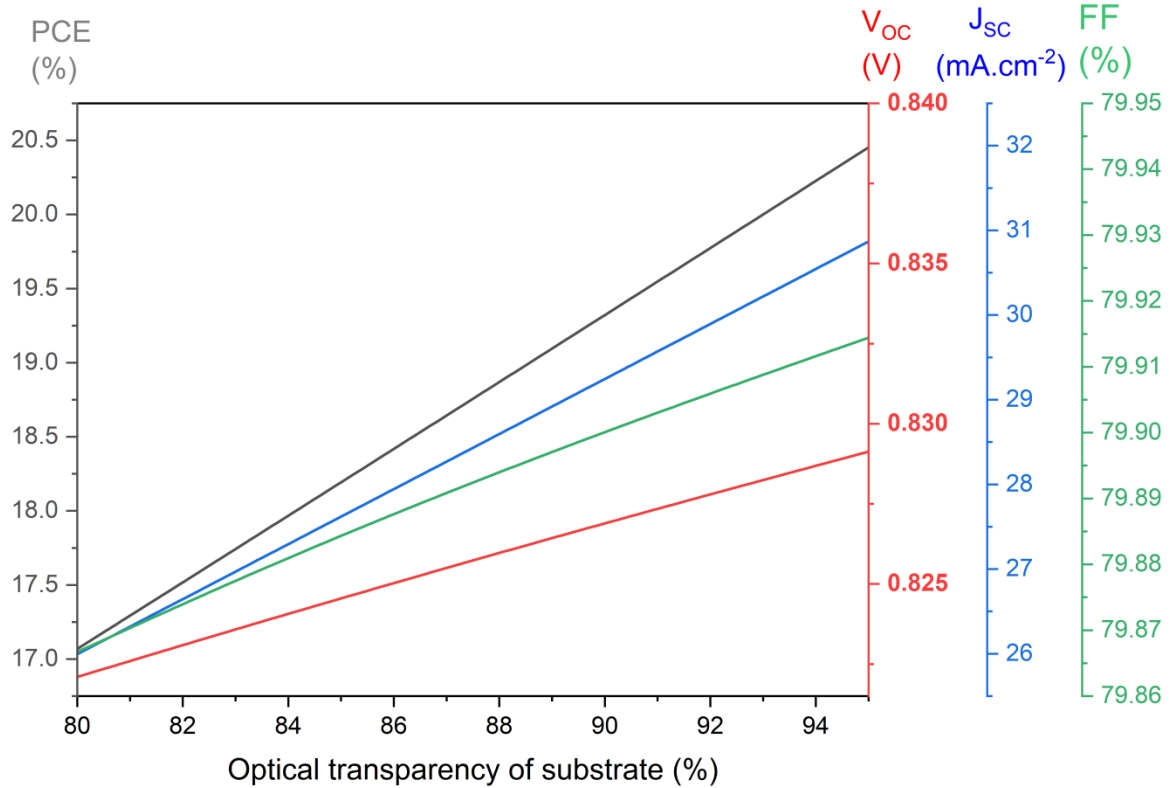


Figure 3-7 Effect of optical transparency of substrate on (a) EQE and (b) J-V of MASnI<sub>3</sub> based PSC.

Results show that substrates with lower optical transparency of 80% showed the lowest EQE values and J-V curve. This is attributed to lower photon coupling in the underlying active absorber layer. While increasing the transparency beyond 80%, improvement in EQE and J-V is observed, and higher performance is obtained for transparency equivalent to 95%, as shown in Fig. 3-7(a-b). Further, PV parameters in terms of  $J_{SC}$ ,  $V_{OC}$ , FF and PCE are summarized in Fig. 3-8. Increasing the transparency did not affect the  $V_{OC}$  and FF but significantly improved the  $J_{SC}$  because

of higher photon absorption in the active layer, which consequently increases the electron-hole generation within the active layer. Quantitatively,  $J_{SC}$  improves from 26  $\text{mA}\cdot\text{cm}^{-2}$  to 31  $\text{mA}\cdot\text{cm}^{-2}$  while increasing the transparency from 80% to 95%. This resulted in improvement in PCE from 17.1% to 20.4%. Therefore, this section concludes that a substrate with higher transparency is needed to yield a maximum PCE of 20.4% for  $\text{MASnI}_3$  based PSC.



**Figure 3-8**Effect of optical transparency of substrate on the PV parameters of  $\text{MASnI}_3$  based PSC.

### **3.1.7: Impact of cathode work function on the performance of $\text{MASnI}_3$ based device.**

Overall collection of light-generated carriers not only depends on the alignment of ETL and HTL with perovskite but also on the work function of the electrodes attached to corresponding transport layers. An appropriate ohmic contact is required to ensure the sufficient collection of electrons from the ETL layer to the cathode electrode. However, deviation from the desired workfunction can significantly affect the device performance by degrading mainly the  $V_{oc}$  and FF of the device. Therefore, the effect

of the cathode work function is extensively investigated in this thesis to understand its impact on the overall PCE of the device.

To perceive the same during simulation, the cathode work function has been varied from 4.2 eV to 5.2 eV, and corresponding EQE, J-V and PV parameters are provided in Fig. 3-9(a-b) and Fig. 3-10, respectively.

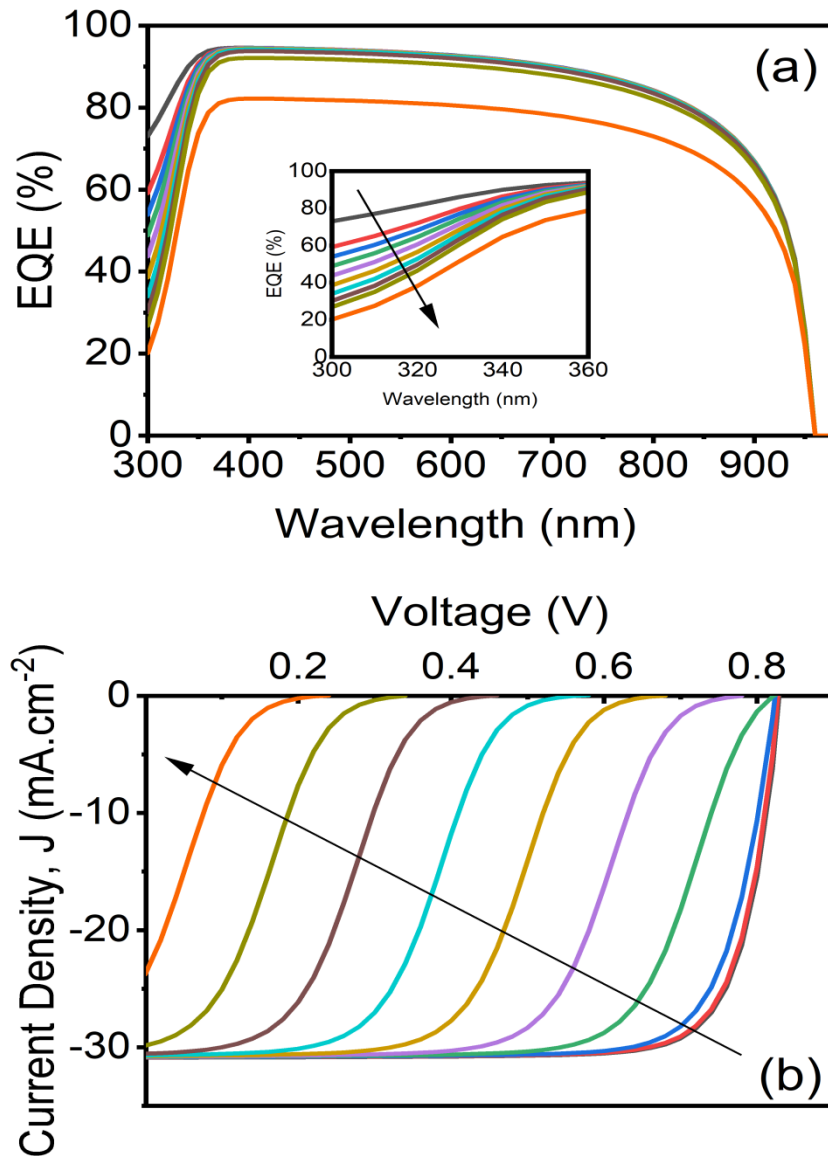


**Figure 3-9**Effect of cathode work function on (a) EQE and (b) J-V of MASnI<sub>3</sub> based PSC.

Results showed that the  $J_{SC}$  remained unaffected till work function of 5.0 eV, and the same can be verified from EQE, J-V and PV parameters reported in this section. The  $V_{OC}$  is also immune to variation till 4.6 eV and thereafter showed significant reduction while increasing the work function beyond 4.6 eV. Among all the PV parameters, FF is significantly affected by the work function variation due to an increase in contact series resistance near the ETL/cathode interface. Increased series resistance is contributed by the associated electric field with ETL/cathode interface, and the direction of the field is such that it is unfavourable for electron transport toward the cathode. This eventually reduces the overall FF of the device, and degradation in all the parameters resulted in a significant reduction in PCE from 20.4% to 0.8% while increasing the work function from 4.2 eV to 5.2 eV, as shown in Fig. 3-10.

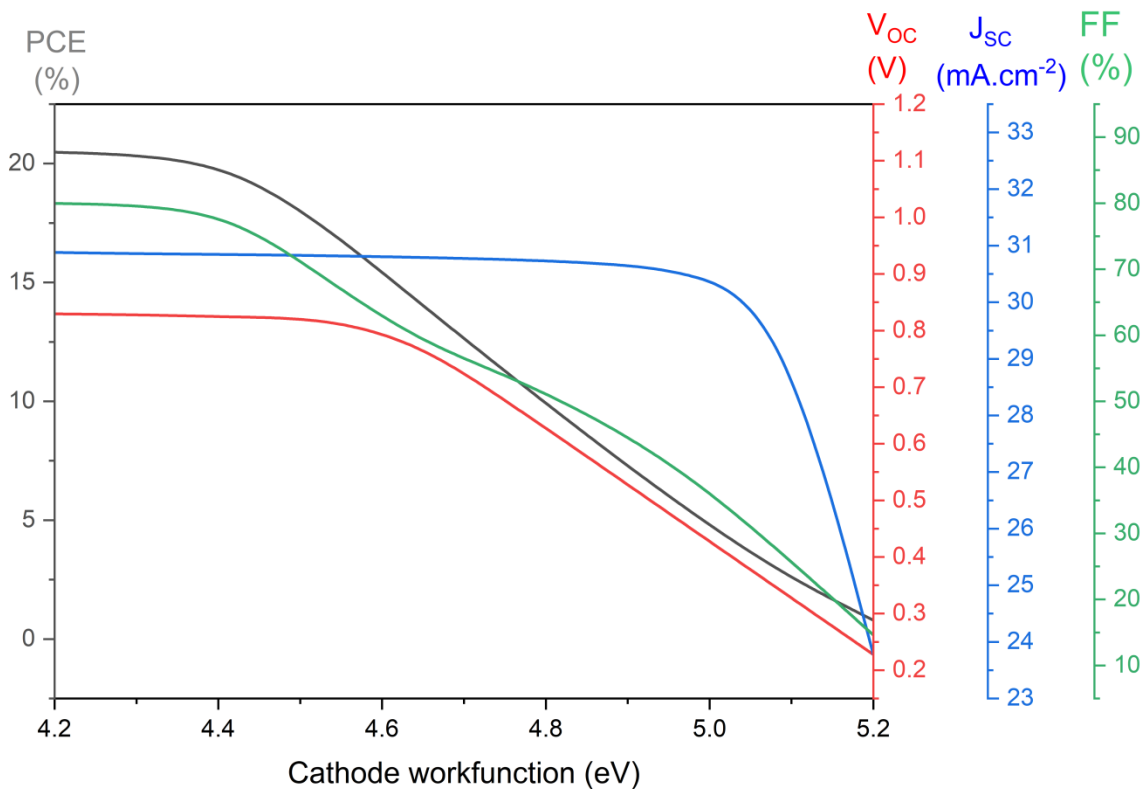


**Figure 3-10** Effect of cathode workfunction on the PV parameters of  $\text{MASnI}_3$  based PSC.

To further investigate the cause of reduction and carrier dynamics within the device, an energy band diagram has also been obtained for two distinct values such as 4.2 eV and 5.2 eV and shown in Fig. 3-11 (a-b). Band diagrams are obtained under illumination and which

showed the splitting of Fermi levels in the form of electron and hole quasi-Fermi levels ( $E_{fn}$  and  $E_{fp}$ ) and the generation of electron-hole pairs. A higher slope of energy band is required to ensure the significant collection probability, and the same has been observed in the case of the 4.2 eV work function-based device compared to 5.2 eV. This resulted in insufficient carrier collection and lower performance at higher work function, i.e., 5.2 eV.

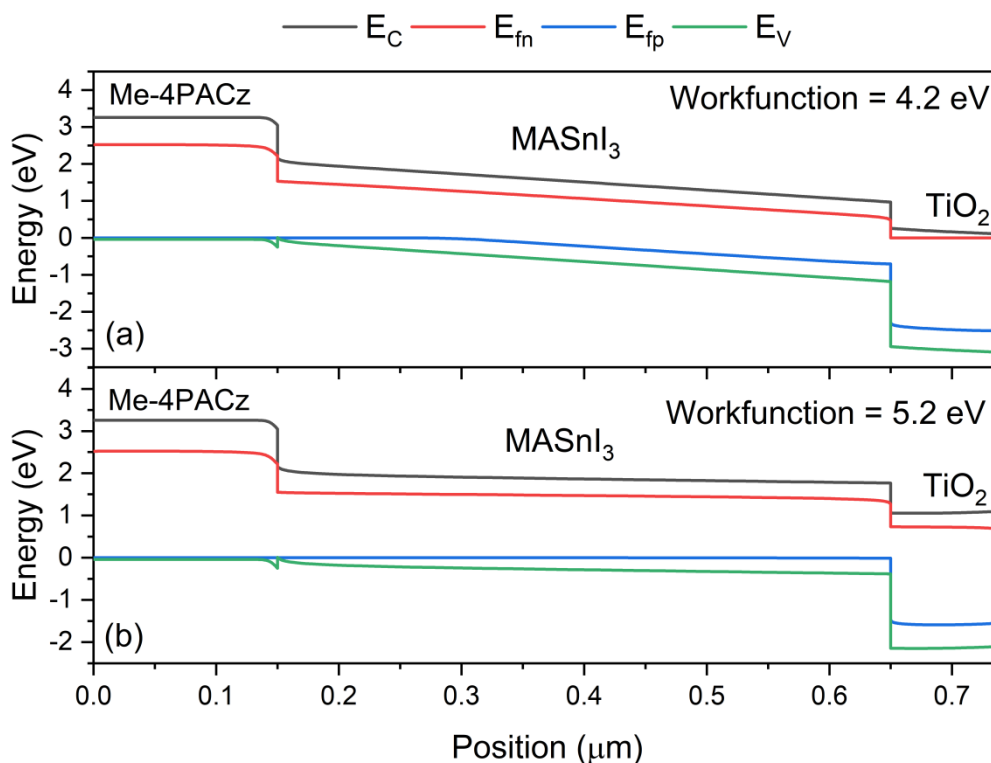


**Figure 3-11** Effect of cathode work function on the energy band diagram of MASnI<sub>3</sub> based PSC.

### 3.4: SUMMARY

This chapter brings forth the detailed investigation of four different Sn-based halides having different iodide and bromide composition. Analysis and optimization have been carried out in terms of absorber layer thickness variation and bulk defect density. Results are interpreted with the help of an energy band diagram and illuminated J-V curves. It has been observed that the best performance is obtained with a 500 nm thick absorber layer having the lowest defect density of  $1 \times 10^{15} \text{ cm}^{-3}$  for all the devices under consideration. The champion device showed 20% conversion efficiency with MASnI<sub>3</sub> at 500 nm thickness with a bulk defect of  $1 \times 10^{15} \text{ cm}^{-3}$ .

<sup>2</sup>. Detailed analysis related to transparency of substrate and cathode work function is also reported to understand the influence of these parameters on the performance of lead-free Sn-based perovskite solar cells.

The next chapter is devoted to another lead-free halide perovskite, i.e., cesium tin halides  $\text{CsSnI}_{3-x}\text{Br}_x$ , for optimizing the device performance of another lead-free halide perovskite solar cell.

### **3.5: REFERENCES**

Al-Ashouri, A., et al. (2020). "Monolithic perovskite/silicon tandem solar cell with > 29% efficiency by enhanced hole extraction." *Science***370**(6522): 1300-1309.

Bi, D., et al. (2016). "Efficient luminescent solar cells based on tailored mixed-cation perovskites." *Science advances***2**(1): e1501170.

Chen, S., et al. (2021). "Preventing lead leakage with built-in resin layers for sustainable perovskite solar cells." *Nature Sustainability***4**(7): 636-643.

Chen, W., et al. (2015). "Efficient and stable large-area perovskite solar cells with inorganic charge extraction layers." *Science***350**(6263): 944-948.

Giustino, F. and H. J. Snaith (2016). "Toward lead-free perovskite solar cells." *ACS Energy Letters***1**(6): 1233-1240.

Green, M. A., et al. (2014). "The emergence of perovskite solar cells." *Nature Photonics***8**(7): 506-514.

Handa, T., et al. (2017). "PhotocARRIER recombination and injection dynamics in long-term stable lead-free  $\text{CH}_3\text{NH}_3\text{SnI}_3$  perovskite thin films and solar cells." *The Journal of Physical Chemistry C***121**(30): 16158-16165.

Hao, F., et al. (2014). "Lead-free solid-state organic–inorganic halide perovskite solar cells." *Nature Photonics***8**(6): 489-494.

Hoefler, S. F., et al. (2017). "Progress on lead-free metal halide perovskites for photovoltaic applications: a review." *Monatshefte für Chemie-Chemical Monthly***148**(5): 795-826.

Hong, F., et al. (2016). "Viability of lead-free perovskites with mixed chalcogen and halogen anions for photovoltaic applications." *The Journal of Physical Chemistry C***120**(12): 6435-6441.

Jeon, N. J., et al. (2018). "A fluorene-terminated hole-transporting material for highly efficient and stable perovskite solar cells." Nature Energy**3**(8): 682-689.

Juarez-Perez, E. J., et al. (2014). "Role of the selective contacts in the performance of lead halide perovskite solar cells." The Journal of Physical Chemistry Letters**5**(4): 680-685.

Kojima, A., et al. (2009). "Organometal halide perovskites as visible-light sensitizers for photovoltaic cells." Journal of the american chemical society**131**(17): 6050-6051.

Li, F., et al. (2019). "A Cation- Exchange Approach for the Fabrication of Efficient Methylammonium Tin Iodide Perovskite Solar Cells." Angewandte Chemie International Edition**58**(20): 6688-6692.

Li, L., et al. (2018). "Recent advances of flexible perovskite solar cells." Journal of energy chemistry**27**(3): 673-689.

Lyu, M., et al. (2017). "Addressing toxicity of lead: progress and applications of low- toxic metal halide perovskites and their derivatives." Advanced energy materials**7**(15): 1602512.

Meng, K., et al. (2016). "Two-dimensional organic–inorganic hybrid perovskite photonic films." Nano letters**16**(7): 4166-4173.

Petrus, M. L., et al. (2017). "Capturing the sun: A review of the challenges and perspectives of perovskite solar cells." Advanced energy materials**7**(16): 1700264.

Razza, S., et al. (2016). "Research Update: Large-area deposition, coating, printing, and processing techniques for the upscaling of perovskite solar cell technology." Apl Materials**4**(9): 091508.

Schmidt, T. M., et al. (2015). "Upscaling of perovskite solar cells: fully ambient roll processing of flexible perovskite solar cells with printed back electrodes." Advanced energy materials**5**(15): 1500569.

Shi, Z., et al. (2017). "Lead- free organic–inorganic hybrid perovskites for photovoltaic applications: recent advances and perspectives." Advanced Materials**29**(16): 1605005.

Song, T.-B., et al. (2015). "Perovskite solar cells: film formation and properties." Journal of Materials Chemistry A**3**(17): 9032-9050.

Su, L., et al. (2021). "Use of organic bulk-heterojunction solar cells as selective contacts in wide bandgap perovskite solar cells: advantages and limitations." Journal of Materials Chemistry A**9**(24): 13979-13985.

Umari, P., et al. (2014). "Relativistic GW calculations on CH<sub>3</sub>NH<sub>3</sub>PbI<sub>3</sub> and CH<sub>3</sub>NH<sub>3</sub>SnI<sub>3</sub> perovskites for solar cell applications." Scientific reports**4**(1): 1-7.

Velilla, E., et al. (2019). "Outdoor performance of perovskite solar technology: Silicon comparison and competitive advantages at different irradiances." Solar Energy Materials and Solar Cells**191**: 15-20.

Wang, J., et al. (2019). "Functional metal oxides in perovskite solar cells." ChemPhysChem**20**(20): 2580-2586.

Wang, M., et al. (2021). "Lead-free perovskite materials for solar cells." Nano-Micro Letters**13**(1): 1-36.

Wang, M., et al. (2021). "Lead-Free Perovskite Materials for Solar Cells." Nano-Micro Letters**13**(1): 62.

Wang, R., et al. (2019). "Opportunities and challenges of lead-free perovskite optoelectronic devices." Trends in Chemistry**1**(4): 368-379.

Wehrenfennig, C., et al. (2014). "Charge carrier recombination channels in the low-temperature phase of organic-inorganic lead halide perovskite thin films." Apl Materials**2**(8): 081513.

Ye, S., et al. (2015). "CuSCN-based inverted planar perovskite solar cell with an average PCE of 15.6%." Nano letters**15**(6): 3723-3728.

Yin, W. J., et al. (2014). "Unique properties of halide perovskites as possible origins of the superior solar cell performance." Advanced Materials**26**(27): 4653-4658.

Zhang, J., et al. (2018). "3D–2D–0D interface profiling for record efficiency all- inorganic CsPbBr<sub>2</sub> perovskite solar cells with superior stability." Advanced energy materials**8**(15): 1703246.

# CHAPTER 4

---

## DESIGN, SIMULATION AND OPTIMIZATION OF LEAD-FREE CESIUM TIN HALIDES BASED SOLAR CELLS

---

The previous chapter summarizes the comprehensive study of methylammonium tin halides perovskite solar cell, which is one of the widely adopted materials as an alternative to lead-based halides perovskite. The impact of halide composition, absorber layer thickness, bulk defect density, the optical transparency of the substrate and cathode work function has also been carried out to optimize the performance. Further, in this particular chapter, another alternative, i.e., cesium tin halides are investigated, and their performance is optimized in terms of different halide composition, absorber layer thickness, bulk defect density, electron transport layer doping, hole transport layer doping

### **4.1: INTRODUCTION**

To provide a remedy for lead toxicity, the community has started increasing efforts to introduce lead-free perovskite materials(Kong, Cheng et al. 2020, Duan, Zhao et al. 2021). When we talk about lead-free perovskite materials, they are perovskite derivatives which are nothing but 3D connected  $BX_6$  octahedrons(Deng, Kieslich et al. 2018). One of the solutions adopted is replacing the  $Pb^{2+}$  with the  $Sn^{2+}$  as in  $MASnI_xBr_{3-x}$ , which ended as ineffective due to the metallic nature of the Sn perovskites(Cao and Yan 2021). However, the inorganic equivalent of the  $MASnI_xBr_{3-x}$ , i.e.,  $CsSnI_xBr_{3-x}$ , is a p-type conductor with a band gap ranging from 1.3eV to 1.75 eV and has a favourable band gap and high optical absorption coefficient ( $10^4 \text{ cm}^{-1}$  compared to  $MASnI_xBr_{3-x}$ (Chung, Song et al. 2012). Its low exaction binding energy (18 meV) represents that it is a suitable candidate as a light absorber for lead-free perovskite solar cells(Ye, Wang et al. 2021). Therefore, this chapter demonstrated the PV potential of  $CsSnI_xBr_{3-x}$  based halide and optimized its efficiency by varying some of the important parameters in terms of absorber layer thickness, bulk defect density, and ETL doping and HTL doping to propose a lead-free perovskite solar cell with superior conversion efficiency.

## **4.2: DEVICE STRUCTURE AND SIMULATION METHODOLOGY**

SCAPS-1D device simulator is again utilized to perform the device simulation for the devices under consideration. Four different Cs and Sn-based halides, such as  $\text{CsSnI}_3$ ,  $\text{CsSnI}_2\text{Br}_1$ ,  $\text{CsSnI}_1\text{Br}_2$  and  $\text{CsSnBr}_3$ , are considered for the device simulation, and their schematics are shown in Fig. 4-1 (a-d). For all the devices, fluorine-doped tin oxide (FTO) substrate has been utilized, and a 90 nm thick PCBM layer which acts as an ETL, is deposited into it followed by deposition of the active layer, i.e.,  $\text{CsSnI}_{3-x}\text{Br}_x$ . The Me-4PACz HTL, as utilized previous, showed inferior energy band alignment with Cs based absorber layer and was unable to extract the light generated hole from the electron-hole pairs generated in the absorber layer. Therefore, different HTL material has been utilized with electrical parameters as tabulated in Table 4-1. The Cs based halide structure with different composition ( $x=0, 1, 2$  and  $3$ ) is shown in Fig. 4-1 (a), (b), (c) and (d), respectively. The  $\text{CsSnI}_3$ ,  $\text{CsSnI}_2\text{Br}_1$ ,  $\text{CsSnI}_1\text{Br}_2$  and  $\text{CsSnBr}_3$  based perovskite solar cells are termed as D1, D2, D3 and D4 throughout this chapter.

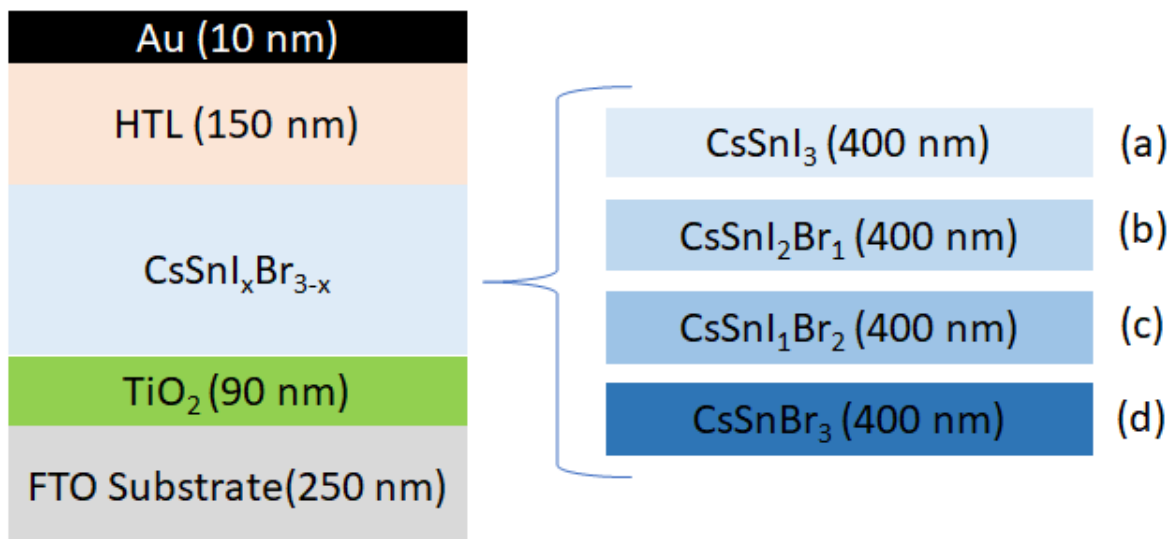


**Figure 4-1 Schematic device structures used during simulation for Cs and Sn-based perovskite solar cells having different iodine and bromine composition (a) D1, (b) D2, (c) D3 and (d) D4**

The energy band diagrams have also been obtained for all the devices, i.e., D1, D2, D3 and D4 and shown in Fig. 4-2(a), (b), (c) and (d), respectively. It can be validated from the band diagram that increasing the bromide composition increases the energy band gap for the perovskite absorber layer from 1.3 eV, 1.37 eV, 1.65 eV to 1.75 eV for CsSnI<sub>3</sub>, CsSnI<sub>2</sub>Br<sub>1</sub>, CsSnI<sub>1</sub>Br<sub>2</sub> and CsSnBr<sub>3</sub> based perovskite absorber layers. It is worth noting that introducing bromide in pure iodide-based halide shows a marginal increase in band gap from 1.3 eV to 1.37 eV in the case of Cs based perovskite, whereas MA-based halide showed significant improvement from 1.3 eV to 1.56 eV as discussed in the previous chapter. Increasing the bromide composition increases the band gap and yields a poor alignment of the energy band of the absorber layer with HTL. A valence band offset at HTL/perovskite interface started appearing for the higher bromide composition, which makes it unfavorable for hole transport in the transport layer from the absorber layer.

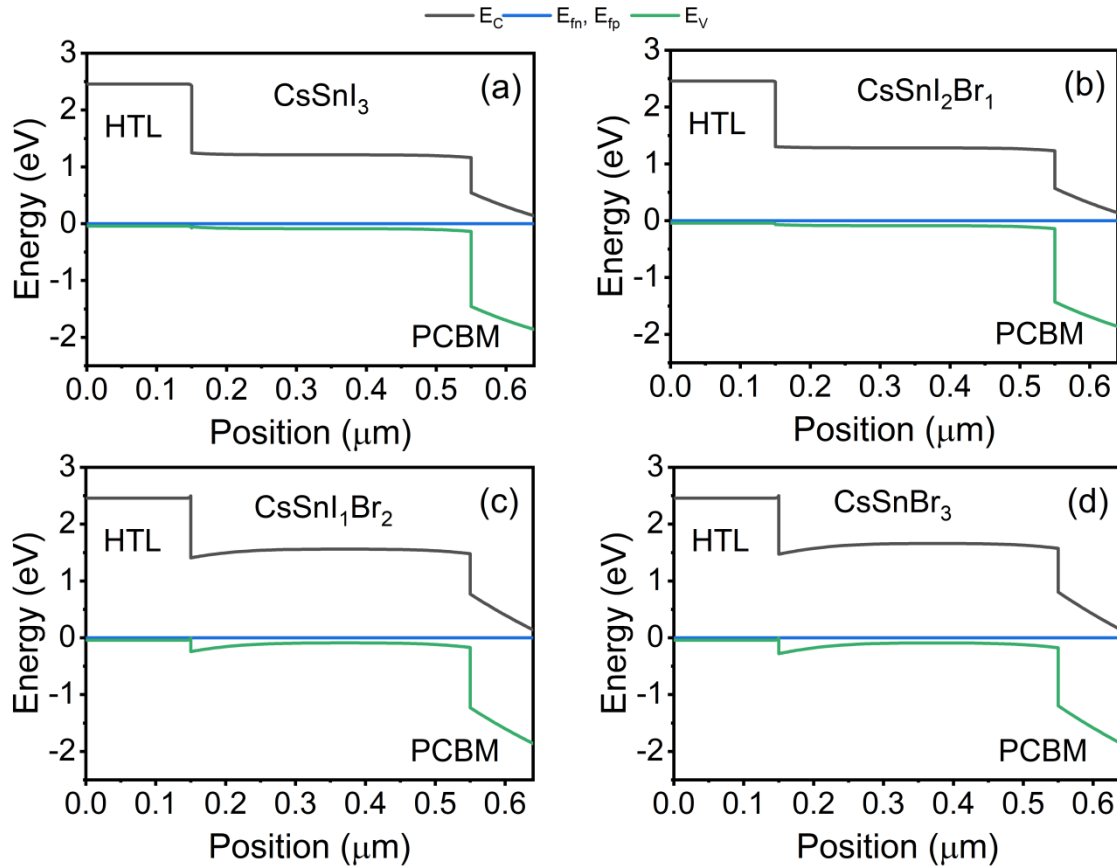


Figure 4-2 Energy band diagram for different Cs and Sn-based perovskite solar cells having different iodine and bromine composition (a) D1, (b) D2, (c) D3 and (d) D4. The data is obtained under thermal equilibrium.

**CHAPTER 4: DESIGN AND SIMULATION OF PEROVSKITE-SILICON TANDEM  
SOLAR CELLS USING LEAD FREE PEROVSKITE-BASED TOP CELLS**

**Table 4-1** Material parameters used during simulation for Cs and Sn-based perovskite solar cells having different iodine and bromine composition (Yang, Zhang et al. 2019, Al-Ashouri, Köhnen et al. 2020, Wang, Wang et al. 2021)

Material	PCBM	CsSnI <sub>3</sub>	CsSnI <sub>2</sub> Br <sub>1</sub>	CsSnI <sub>1</sub> Br <sub>2</sub>	CsSnBr <sub>3</sub>	HTL
<b>Parameter</b>						
<b>Bandgap (eV)</b>	2.0	1.3	1.37	1.65	1.75	2.9
<b>Electron affinity (eV)</b>	3.9	3.28	3.78	3.19	3.13	2.1
<b>Dielectric Permittivity</b>	9	10	10	10	10	10
<b>CB effective density of states (cm<sup>-3</sup>)</b>	2.2x10 <sup>18</sup>	1x10 <sup>19</sup>	1x10 <sup>19</sup>	1x10 <sup>19</sup>	1x10 <sup>19</sup>	1x10 <sup>19</sup>
<b>VB effective density of states (cm<sup>-3</sup>)</b>	1.8x10 <sup>19</sup>	1x10 <sup>19</sup>	1x10 <sup>19</sup>	1x10 <sup>19</sup>	1x10 <sup>19</sup>	1x10 <sup>19</sup>
<b>Electron mobility (cm<sup>2</sup>V<sup>-1</sup>s<sup>-1</sup>)</b>	4	2	2	2	2	5.0x10 <sup>1</sup>
<b>Hole mobility (cm<sup>2</sup>V<sup>-1</sup>s<sup>-1</sup>)</b>	4	2	2	2	2	5.0x10 <sup>1</sup>
<b>Donor density N<sub>D</sub> (cm<sup>-3</sup>)</b>	1x10 <sup>16</sup>	0	0	0	0	0
<b>Acceptor density N<sub>A</sub> (cm<sup>-3</sup>)</b>	0	5x10 <sup>16</sup>	5x10 <sup>16</sup>	5x10 <sup>16</sup>	5x10 <sup>16</sup>	2x10 <sup>18</sup>

**Table 4-2** Interface defect parameters used during simulation for Cs and Sn-based perovskite solar cells having different iodine and bromine composition.

Interface	HTL/CsSnI <sub>3-x</sub> Br <sub>x</sub>	CsSnI <sub>3-x</sub> Br <sub>x</sub> /PCBM
<b>Parameters</b>		
<b>Capture cross section electrons (cm<sup>2</sup>)</b>	1x10 <sup>-19</sup>	1x10 <sup>-19</sup>
<b>Capture cross section holes (cm<sup>2</sup>)</b>	1x10 <sup>-19</sup>	1x10 <sup>-19</sup>
<b>Energy with respect to reference (eV)</b>	0.6	0.6
<b>Total density (integrated over all energies) (cm<sup>-2</sup>)</b>	1x10 <sup>10</sup>	1x10 <sup>10</sup>
<ul style="list-style-type: none"> <li>For all the cases, the defect type is neutral with a single energetic distribution. The reference for defect energy level (E<sub>t</sub>) is above the highest E<sub>v</sub>.</li> <li>For neutral defects, carrier lifetimes are determined using <math>\tau_n = 1/(\sigma_n v_{th} N_t)</math> and <math>\tau_p = 1/(\sigma_p v_{th} N_t)</math>. Where <math>\sigma_n, \sigma_p, v_{th}, N_t</math> are the electron capture cross-section, hole capture cross-section, thermal velocity (10<sup>7</sup> cm/s), and total defect density, respectively.</li> </ul>		

The material parameters used during simulations are summarized in Table 4.1, and considered values for interface defects are shown in Table 4.2. The neutral type bulk defect for the active layer is also considered for the active (perovskite) layer with an electron/hole capture cross-

section of  $1 \times 10^{15} \text{ cm}^2$  having a defect density of  $1.5 \times 10^{16} \text{ cm}^{-3}$  to account for bulk defect recombination. Standard AM1.5G spectrum has been utilized to illuminate the device and to obtain optoelectronic performances. The equation and coefficient utilized by SCAPS-1D to solve the device physics are also considered, as reported in the previous chapter. Square root at  $E_g$  model is utilized to generate the optical properties for the perovskite absorber layer. Generated absorption coefficient data is represented in Fig. 4-3. Increasing the bromide concentration resulted in a reduction in the higher cutoff wavelengths from 953 nm to 708 nm due to enhancement in energy band gap.

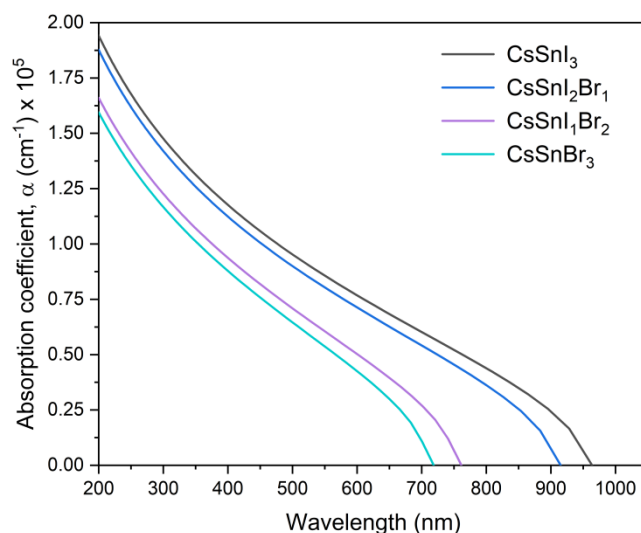


Figure 4-3 Absorption coefficient for different Cs and Sn-based perovskite solar cells having different iodine and bromine composition i.e.,  $\text{CsSnI}_3$ ,  $\text{CsSnI}_2\text{Br}_1$ ,  $\text{CsSnI}_1\text{Br}_2$  and  $\text{CsSnBr}_3$ .

### **4.3: RESULTS AND DISCUSSIONS**

As stated in the previous chapter, the performance of solar cells depends on the efficient utilization of the solar cell and the successful collection of light-generated charge carriers in the external circuits (Gonzalez-Pedro, Juarez-Perez et al. 2014, Chowdhury, Shahahmadi et al. 2020). Absorber layer thickness and bulk defect density play a crucial role in determining the overall performance of the device (Chowdhury, Shahahmadi et al. 2020). A thick absorber layer-based device yields higher photon absorption but requires a higher carrier lifetime so that light generated carriers can travel up to the higher diffusion length to ensure their arrival at collecting interfaces, i.e., ETL/absorber layer or HTL/absorber layer. On the other hand, if we consider a thin absorber layer device then active layer with even small carrier lifetime and

diffusion length is capable in extracting the light generated electron hole pairs. Therefore, collective optimization of defect density and absorber layer thickness is a must consideration to optimize the performance of the device. Section 4.3.1 is dedicated for such analysis.

The electron and hole transport layer also play a critical role in extracting the light-generated charge carriers, which are generated upon optical illumination (Mahmood, Sarwar et al. 2017, Valadi, Gharibi et al. 2021). The transport layer must have an appropriate band alignment with the absorber layer and must offer a low resistance for the charge carrier (Gong, Sun et al. 2018). Overall doping in the transport layer can help in tuning the resistivity of the transport layer, and therefore this particular aspect is also analyzed, and a detailed analysis of ETL and HTL doping on PV performance is reported in section 4.3.2.

### **4.3.1: Comprehensive analysis of the collective impact of absorber layer thickness and bulk defect density on the performance of CsSnI<sub>3-x</sub>Br<sub>x</sub> based perovskite solar cells.**

#### **➤ Impact on J<sub>SC</sub>**

The collective impact of absorber layer thickness and bulk defect density is investigated for all the devices from D1 to D4 and presented in Fig. 4-4 to Fig. 4-7. PV parameters such as J<sub>SC</sub>, V<sub>OC</sub>, FF and PCE are reported in Fig. 4-4, 4-5, 4-6 and 4-7, respectively. The absorption coefficient, as reported in Fig. 4-3, showed that D1 has a wider absorption spectrum compared to other devices, and it reduces while moving from D2 to D4. Therefore, a higher J<sub>SC</sub> value has been obtained for the D1 device compared to other devices in line. It is worth noting that all the devices showed inferior J<sub>SC</sub> values for thin, i.e., 100 nm thick absorber layer at the same time, performance remains immune to variation in defect density from 1x10<sup>15</sup> cm<sup>-3</sup> to 1x10<sup>17</sup> cm<sup>-3</sup>. The situation is different at higher thicknesses, i.e., to ensure better J<sub>SC</sub>, a higher thickness is required but with the lowest possible bulk defect value of 1x10<sup>15</sup> cm<sup>-3</sup>. Increasing the defect at higher thicknesses increases the recombination of light-generated charge carriers and reduces the J<sub>SC</sub>, as shown in Fig. 4-4(a-d).

Minimum/maximum JSC values for different device from D1 to D4 is listed as 17.2 mA.cm<sup>-2</sup>/30.8 mA.cm<sup>-2</sup>, 16.74 mA.cm<sup>-2</sup>/27.42 mA.cm<sup>-2</sup>, 11.72 mA.cm<sup>-2</sup>/18.75 mA.cm<sup>-2</sup>, and 10.39 mA.cm<sup>-2</sup>/16.17 mA.cm<sup>-2</sup>. D1 outperforms compared other devices in terms of JSC and delivered maximum value of 30.8 mA.cm<sup>-2</sup> with 500 nm thick absorber layer having minimal defect density of 1x10<sup>15</sup> cm<sup>-3</sup>.

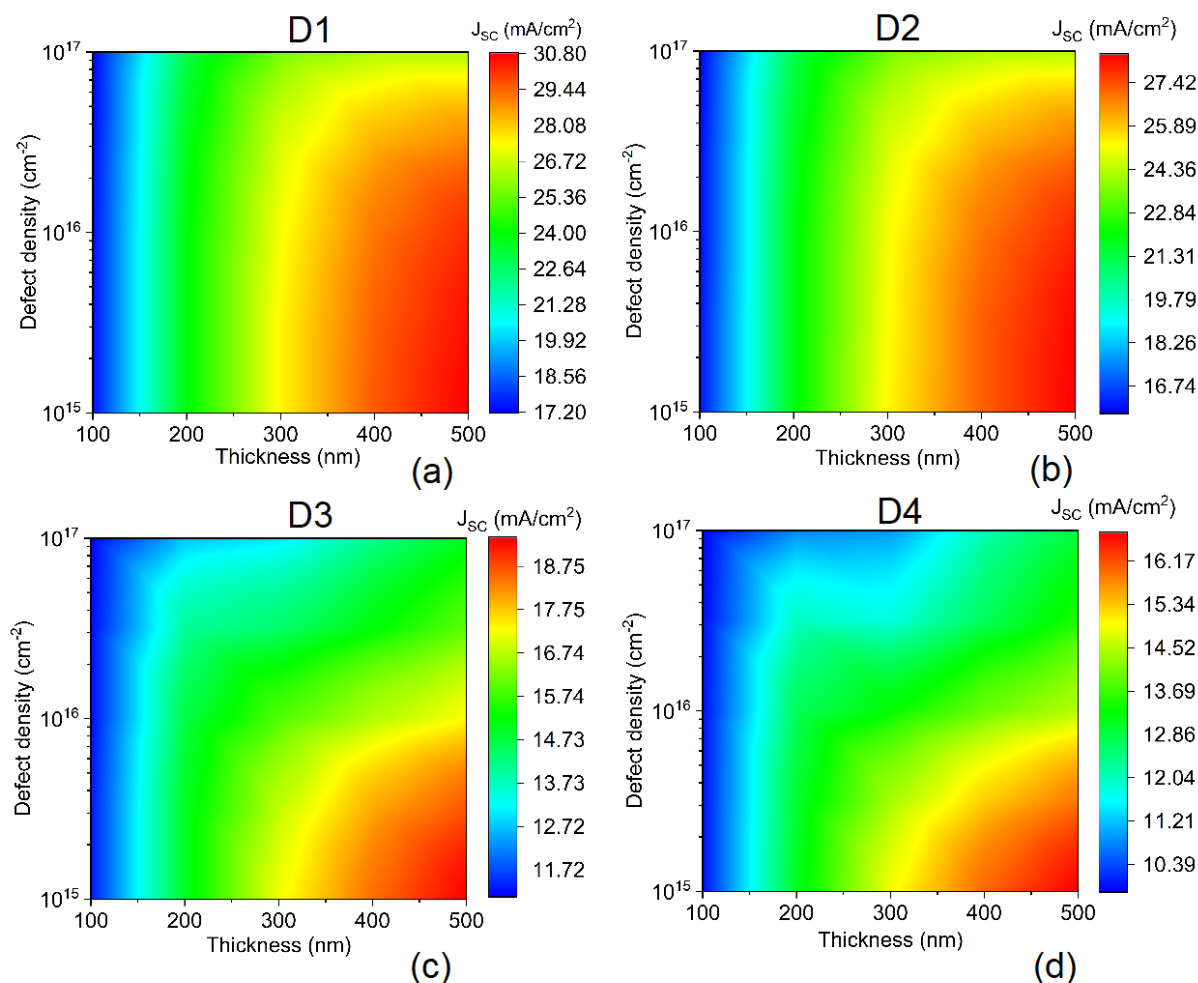


**Figure 4-4** Contour plot of JSC during collective variation of defect density and absorber layer thickness for different devices (a) D1, CsSnI<sub>3</sub> (b) D2, CsSnI<sub>2</sub>Br<sub>1</sub> (c) D3, CsSnI<sub>1</sub>Br<sub>2</sub> and (d) D4, CsSnBr<sub>3</sub>

### ➤ Impact on Voc

This sub-section explored the defect density at different thicknesses for the lead-free perovskite solar cells, i.e., CsSnI<sub>3</sub>, and its implications for photovoltaic performance on Voc and reported in Fig. 4-5(a-d). As stated earlier, D4 has a higher bandgap compared to other devices and therefore showed superior Voc values compared to other devices. It is observed that both D1 and D2 showed the

lowest VOC with a thickness of 500 nm and defect density of  $1 \times 10^{17} \text{ cm}^{-3}$ , whereas D3 and D4 showed inferior values of VOC with 100 nm thickness and higher defect density of  $1 \times 10^{17} \text{ cm}^{-3}$ . Both D1 and D2 showed higher absorption and hence higher number of lights generated carriers, but elevated recombination neutralizes them through the recombination process at higher thickness, therefore, showing minimum VOC at the higher thickness and defect levels. Alternatively, for the D3 and D4, considering lower absorption and a smaller number of lights generated, charge carriers' VOC gets reduced at lower thickness with higher defect levels.

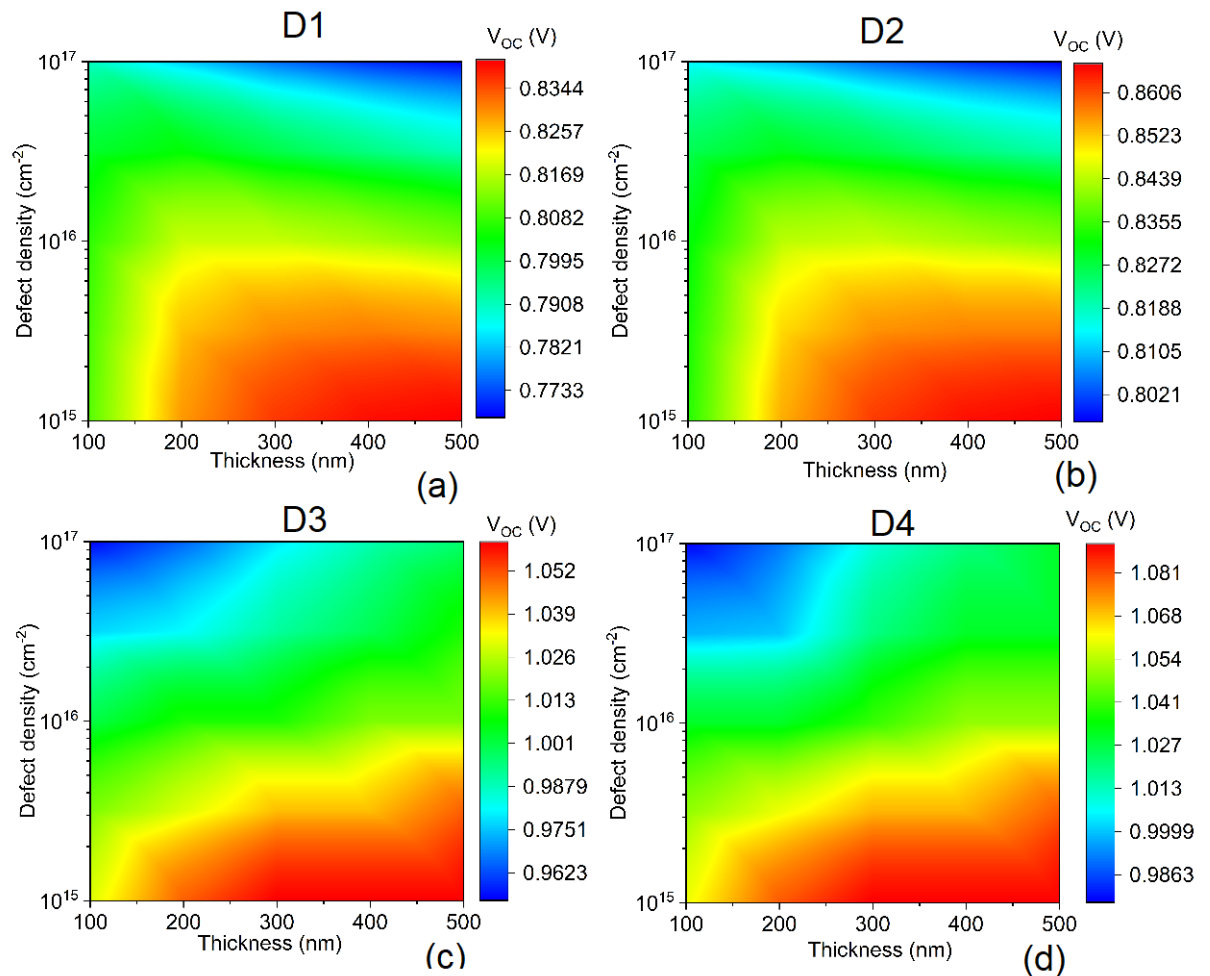


**Figure 4-5** Contour plot of JSC during collective variation of defect density and absorber layer thickness for different devices (a) D1, CsSnI<sub>3</sub> (b) D2, CsSnI<sub>2</sub>Br<sub>1</sub> (c) D3, CsSnI<sub>1</sub>Br<sub>2</sub> and (d) D4, CsSnBr<sub>3</sub>

Minimum/maximum VOC values for the different device from D1 to D4 is listed as 773 mV/834 mV, 802 mV/860 mV, 962 mV/1052 mV, and 986 mV/1081

mV. D4 outperforms compared other devices in terms of VOC and delivers a maximum value of 1081 mV with a 500 nm thick absorber layer having a minimal defect density of  $1 \times 10^{15} \text{ cm}^{-3}$ . Higher VOC is attributed to the wider bandgap of D4 compared to other absorber layer-based devices.

➤ **Impact on FF**

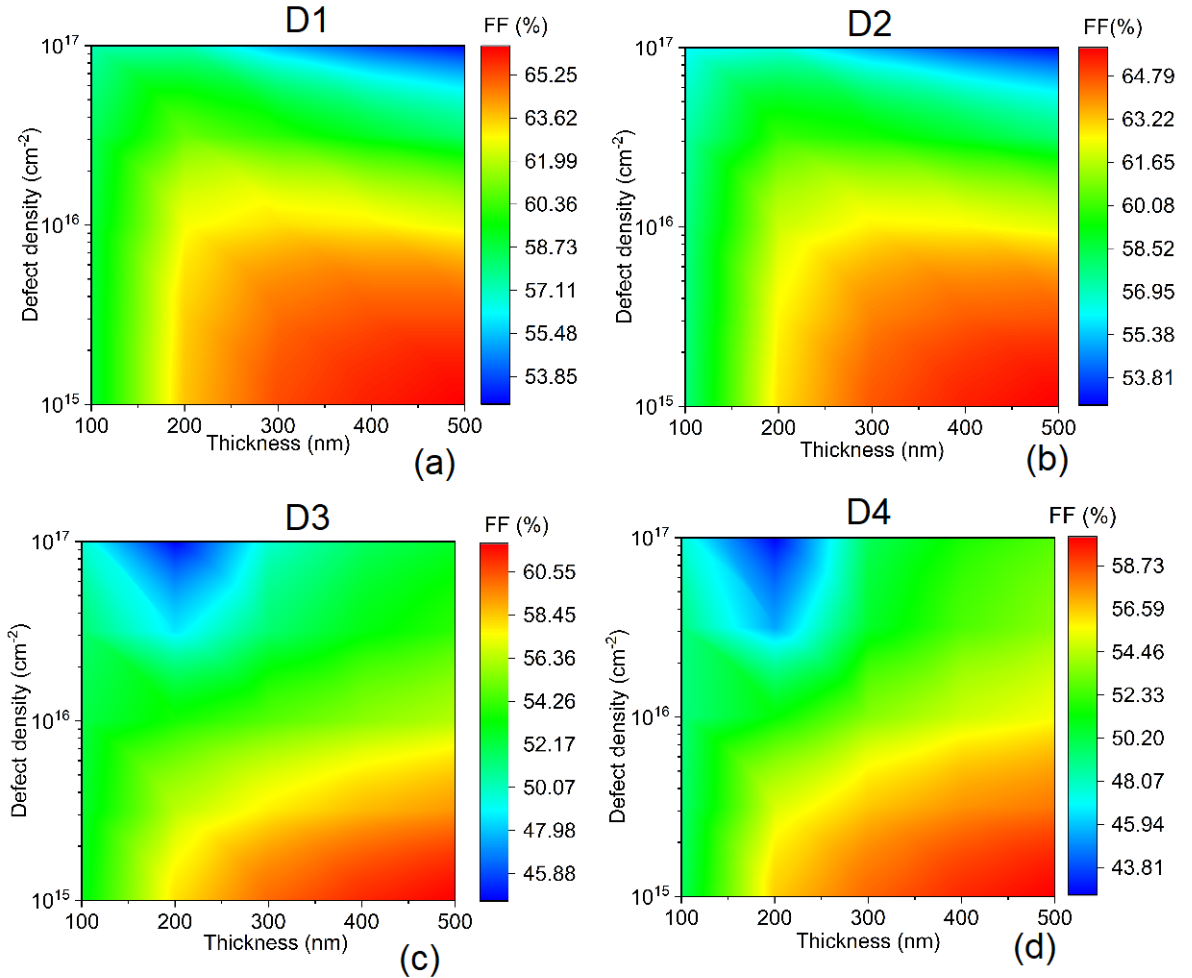


**Figure 4-6** Contour plot of JSC during collective variation of defect density and absorber layer thickness for different devices (a) D1,  $\text{CsSnI}_3$  (b) D2,  $\text{CsSnI}_2\text{Br}_1$  (c) D3,  $\text{CsSnI}_1\text{Br}_2$  and (d) D4,  $\text{CsSnBr}_3$

This sub-section explored the defect density at different thicknesses for the lead-free perovskite solar cells, i.e.,  $\text{CsSnI}_3$ , and its implications for photovoltaic performance on FF and reported in Fig. 4-6(a-d). FF solely depends on the series resistance of the device and showed a similar trend as VOC and validates that a thick absorber layer-

based device is required with low defect density to get maximum deliverable FF from the respective device. Minimum/maximum FF values for different device from D1 to D4 is listed as 53.8 %/65.2 %, 53.8 %/64.8 %, 45.9 %/60.5 %, and 43.8 %/58.7 %. D1 outperformed compared to other devices in terms of FF and delivered a maximum value of 65.2% with a 500 nm thick absorber layer having a minimal defect density of  $1 \times 10^{15} \text{ cm}^{-3}$ . Higher FF is attributed to the smaller band gap of D1, which offered lower resistance compared to other absorber layer-based devices.

➤ **Impact on PCE**

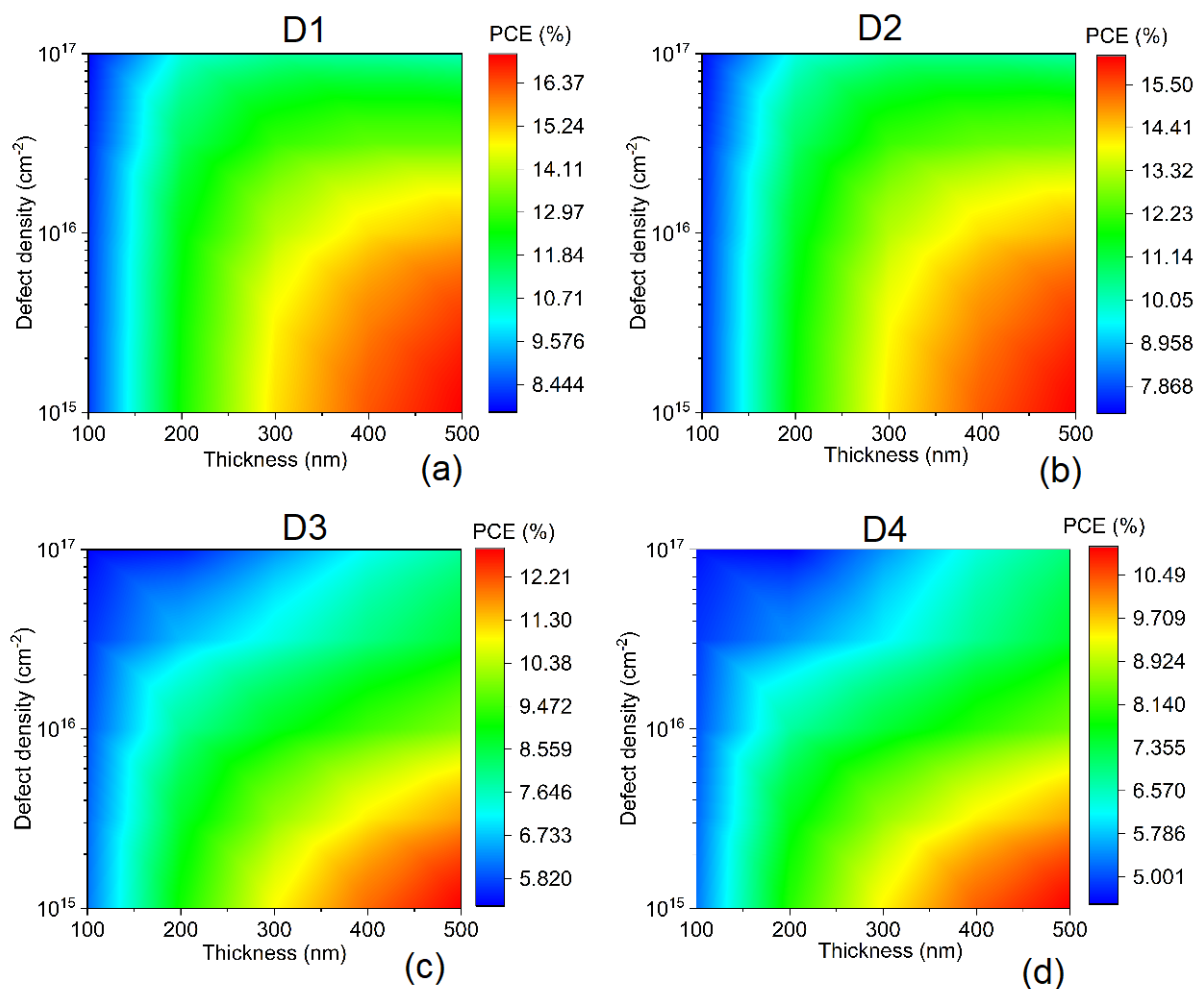


**Figure 4-7** Contour plot of JSC during collective variation of defect density and absorber layer thickness for different devices (a) D1, CsSnI<sub>3</sub> (b) D2, CsSnI<sub>2</sub>Br<sub>1</sub> (c) D3, CsSnI<sub>1</sub>Br<sub>2</sub> and (d) D4, CsSnBr<sub>3</sub>

The collective influence of defect density and absorber layer thickness on PCE is reported in Fig. 4-7(a-d) for the different devices from D1 to D4. Overall conversion efficiency is determined by the combination of  $J_{sc}$ ,  $V_{oc}$  and FF, i.e., PCE is the product of JSC, VOC and FF. Therefore, it can be estimated from the results concluded in the previous subsection. D1 outperformance in terms of JSC and FF, whereas D4 showed superior VOC compared to other devices. In the case of D1, improvement in JSC and FF is significant to mitigate any loss in VOC values; therefore, in overall comparison in terms of PCE, D1 surpassed the maximum achieved PCE by D2 to D4.

Minimum/maximum PCE values for different device from D1 to D4 is listed as 8.4 %/16.3 %, 7.8 %/15.5 %, 5.8 %/12.2 %, and 5.0 %/10.5 %. D1 outperforms compared other devices in terms of PCE and delivers maximum value of 16.4% with a 500 nm thick absorber layer having a minimal defect density of  $1 \times 10^{15} \text{ cm}^{-3}$ . Higher PCE is attributed to higher JSC and FF values due to the smaller band gap of D1 compared to other absorber layer-based devices.

### **4.3.2: Comprehensive analysis of the doping variation in ETL and HTL on the performance of $\text{CsSnI}_{3-x}\text{Br}_x$ based perovskite solar cells.**

#### **➤ ETL doping**

ETL is basically utilized to extract the light generated electrons from electron-hole pairs generated within the absorber layer. An ETL must offer a low resistive path for the electron to ensure a better collection yield in the external circuit. Therefore, optimization of overall doping is a crucial parameter to tune the performance of the device. Considering this in mind, a detailed investigation of donor doping in ETL has been performed for all the devices from D1 to D4. Devices with optimum performance in terms of PCE have been selected for the ETL doping variation. D1, D2, D3 and D4 considered with PCE of 17.1%, 16.2%, 12.7% and 10.9%, respectively. It is also important to note that in the previous section, to optimize the defect and thickness, ETL and HTL doping were kept constant, as shown in Table 4-1.

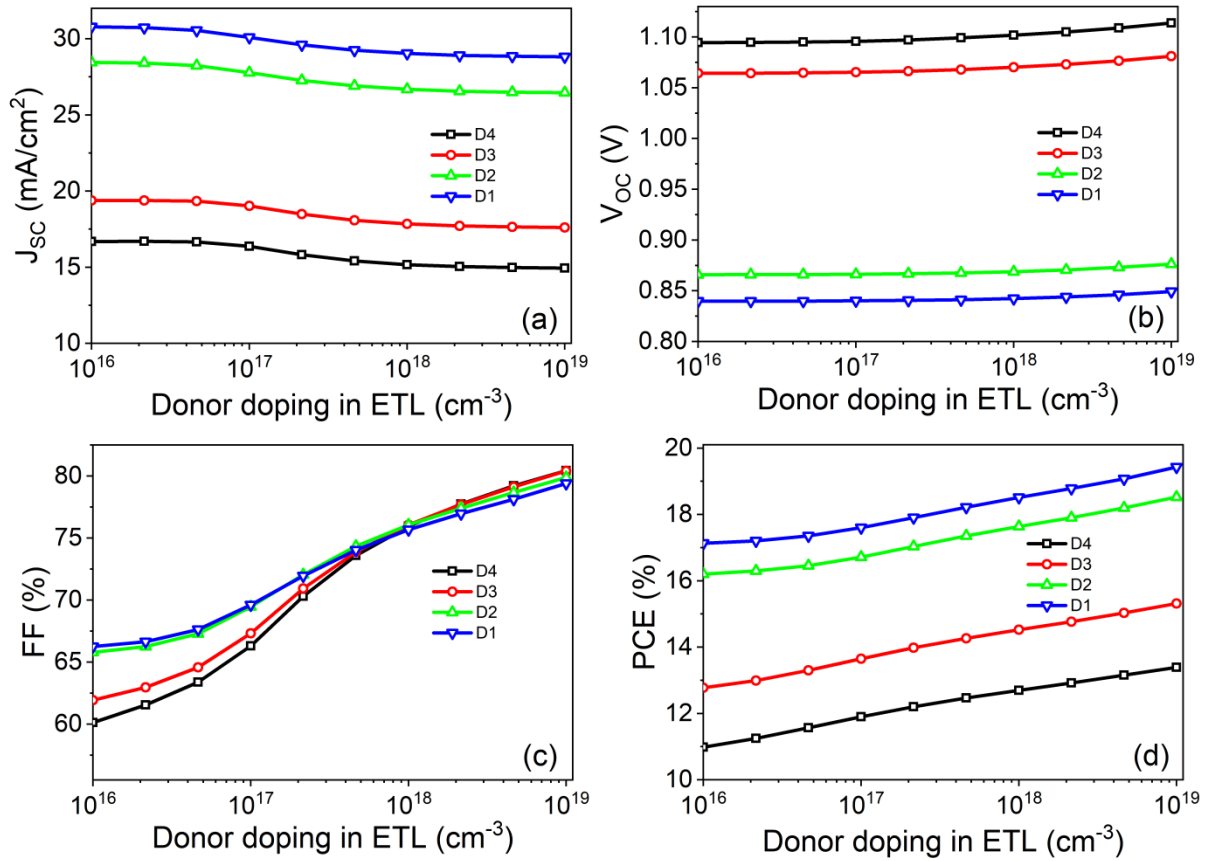


**Figure 4-8** PV parameters for Cs and Sn-based halide devices (D1 to D4) at various donor densities in ETL.

Performance in terms of  $J_{sc}$ ,  $V_{oc}$ , FF and PCE of all the four devices is summarized in Fig. 4-8(a-d). Increasing the doping increases the built-in potential and increases the electric field associated with the ETL/absorber layer interface however remained confined within a small region at higher doping levels. This eventually reduces the collection probability; therefore, a reduction in  $J_{sc}$  has been observed in all the devices while increasing the doping from  $1 \times 10^{16}$  cm<sup>-3</sup> to  $1 \times 10^{19}$  cm<sup>-3</sup>. An increase in  $V_{oc}$  is also observed while increasing the doping due to higher built-in potential and better splitting of quasi-Fermi levels. Donor doping variation majorly affected the FF of the device and showed remarkable improvement in FF while increasing the doping from  $1 \times 10^{16}$  cm<sup>-3</sup> to  $1 \times 10^{19}$  cm<sup>-3</sup>. The highest FF of close to 80% has been simulated in almost all the devices. Enhancement in FF yielded improvement

in PCE from 17.1% to 19.4%, 16.2% to 18.5%, 12.7% to 15.3% and 10.9% to 13.4%, respectively for D1, D2, D3 and D4 devices while increasing the doping from  $1 \times 10^{16} \text{ cm}^{-3}$  to  $1 \times 10^{19} \text{ cm}^{-3}$ . ETL doping optimization resulted in the highest efficiency of 19.4% with the D1 device.

➤ **HTL doping**

Just like ETL, HTL is basically utilized to extract the light generated holes from electron-hole pairs generated within the absorber layer. An HTL must also offer a low resistive path for the holes to ensure a better collection yield in the external circuit. Therefore, optimization of overall acceptor doping is a crucial parameter to tune the performance of the device. Considering this in mind, a detailed investigation of acceptor doping in HTL has also been performed for all the devices from D1 to D4. Performance in terms of J<sub>SC</sub>, V<sub>OC</sub>, FF and PCE of all the four devices is summarized in Fig. 4-9(a-d). Results showed that increasing the doping increases does not affect the J<sub>SC</sub> and V<sub>OC</sub> significantly but improves the FF of the device. Improvement in FF is also linked to the reduced series resistance of HTL at higher doping. The highest FF of close to 80% has been simulated in almost all the devices. Enhancement in FF yielded improvement in PCE from 5% to 19.6%, 5.6% to 18.6%, 8.2 to 15.5% and 8.0% to 13.5%, respectively for D1, D2, D3 and D4 devices while increasing the doping from  $1 \times 10^{16} \text{ cm}^{-3}$  to  $1 \times 10^{19} \text{ cm}^{-3}$ . HTL doping optimization resulted in the highest efficiency of 19.6% with the D1 device.

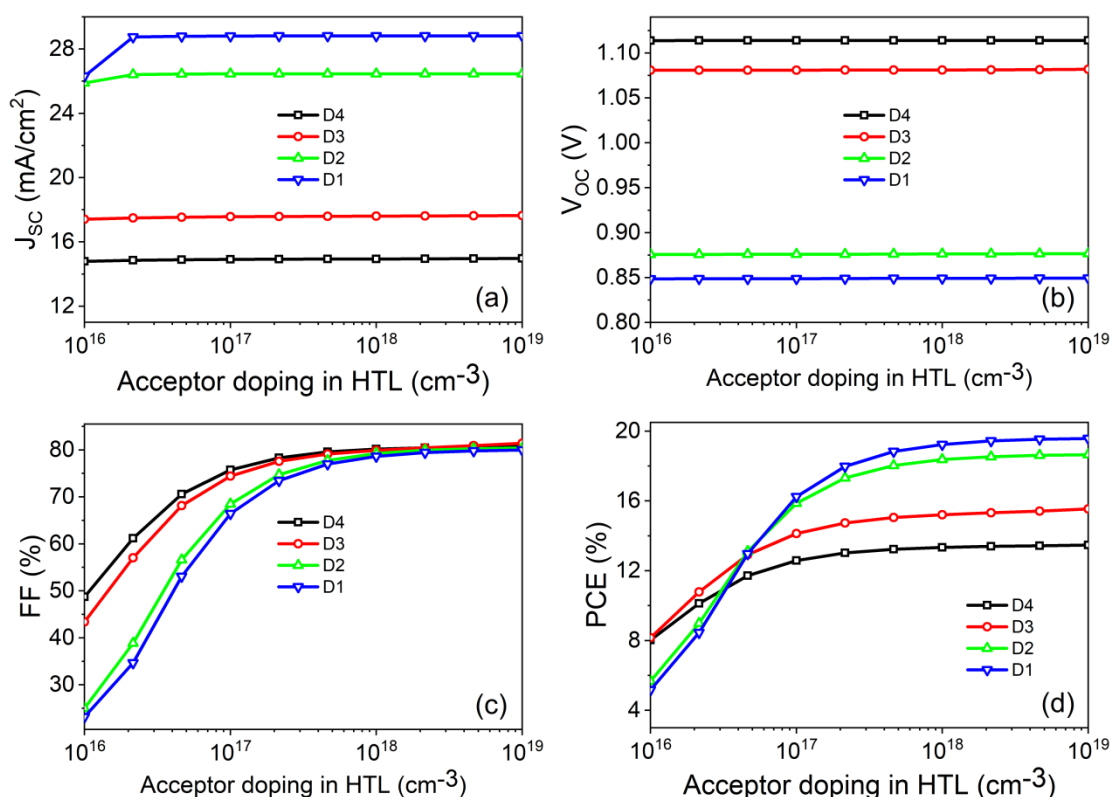


**Figure 4-9** PV parameters for Cs and Sn-based halide devices (D1 to D4) at various donor densities in ETL.

#### 4.4: SUMMARY

This chapter brought the comprehensive study of Cs and Sn-based lead-free halide perovskite solar cells having different iodide and bromide composition. Considered perovskite is a potential alternative to existing lead-based perovskite solar cells. However, a detailed investigation is required to explore the real potential of these devices. Therefore, performance optimization of such devices has been carried out in terms of defect density and absorber layer thickness variation for CsSnI<sub>3</sub>, CsSnI<sub>2</sub>Br<sub>1</sub>, CsSnI<sub>1</sub>Br<sub>2</sub> and CsSnBr<sub>3</sub> based perovskites. This resulted in optimum conversion efficiency of 17.1% with the CsSnI<sub>3</sub> absorber layer-based device. Thereafter, the impact of ETL and HTL doping has also been investigated for all four devices to further improve the performance by mitigating the resistive losses associated with transport layers. Transport layer doping optimization yielded a 19.6% efficient CsSnI<sub>3</sub> based perovskite solar cell.

Chapter 3 concluded  $\text{MASnI}_3$  perovskite solar cell with 20% conversion efficiency, and chapter 4 summarized  $\text{CsSnI}_3$  based perovskite solar cell with 19.6% conversion efficiency. This shows that it is very difficult to boost the conversion efficiency beyond 20% in standalone configuration due to inherent thermalization and transparent band gap losses. Therefore, in the next chapter, the concept of a tandem device has been proposed and investigated to boost the conversion efficiency for lead-free perovskite solar cells beyond 20% by mitigating thermalization and transparent band gap losses.

## **4.5: REFERENCES**

Al-Ashouri, A., et al. (2020). "Monolithic perovskite/silicon tandem solar cell with > 29% efficiency by enhanced hole extraction." Science**370**(6522): 1300-1309.

Cao, J. and F. Yan (2021). "Recent progress in tin-based perovskite solar cells." Energy & Environmental Science**14**(3): 1286-1325.

Chowdhury, M., et al. (2020). "Effect of deep-level defect density of the absorber layer and n/i interface in perovskite solar cells by SCAPS-1D." Results in Physics**16**: 102839.

Chung, I., et al. (2012). "CsSnI<sub>3</sub>: Semiconductor or Metal? High Electrical Conductivity and Strong Near-Infrared Photoluminescence from a Single Material. High Hole Mobility and Phase-Transitions." Journal of the American Chemical Society**134**(20): 8579-8587.

Deng, Z., et al. (2018). "Octahedral connectivity and its role in determining the phase stabilities and electronic structures of low-dimensional, perovskite-related iodoplumbates." APL Materials**6**(11): 114202.

Duan, C., et al. (2021). "Lead-Free Cesium-Containing Halide Perovskite and Its Application in Solar Cells." IEEE Journal of Photovoltaics**11**(5): 1126-1135.

Gong, X., et al. (2018). "Highly efficient perovskite solar cells with gradient bilayer electron transport materials." Nano Letters**18**(6): 3969-3977.

Gonzalez-Pedro, V., et al. (2014). "General working principles of  $\text{CH}_3\text{NH}_3\text{PbX}_3$  perovskite solar cells." Nano Letters**14**(2): 888-893.

Kong, D., et al. (2020). "Solution processed lead-free cesium titanium halide perovskites and their structural, thermal and optical characteristics." Journal of Materials Chemistry C**8**(5): 1591-1597.

Mahmood, K., et al. (2017). "Current status of electron transport layers in perovskite solar cells: materials and properties." RSC Advances**7**(28): 17044-17062.

Valadi, K., et al. (2021). "Metal oxide electron transport materials for perovskite solar cells: a review." Environmental Chemistry Letters**19**(3): 2185-2207.

Wang, M., et al. (2021). "Lead-Free Perovskite Materials for Solar Cells." Nano-Micro Letters**13**(1): 62.

Yang, D., et al. (2019). "Stable Efficiency Exceeding 20.6% for Inverted Perovskite Solar Cells through Polymer-Optimized PCBM Electron-Transport Layers." Nano Letters**19**(5): 3313-3320.

Ye, T., et al. (2021). "Ambient-Air-Stable Lead-Free CsSnI<sub>3</sub> Solar Cells with Greater than 7.5% Efficiency." Journal of the American Chemical Society**143**(11): 4319-4328.

# CHAPTER 5

---

## DESIGN AND SIMULATION OF PEROVSKITE-SILICON TANDEM SOLAR CELLS USING LEAD FREE PEROVSKITE-BASED TOP CELLS

---

The previous chapters summarize the comprehensive study of  $\text{MASnI}_{3-x}\text{Br}_x$  and  $\text{CsSnI}_{3-x}\text{Br}_x$  based lead-free perovskite solar cells, where optimization has also been performed to improve the conversion efficiency. Both the previous chapters, i.e., 3 and 4, focused only on single-junction design, which suffers from thermalization and transparent band gap losses, which are inherent and are unavoidable using the single-junction approach. In chapter 3,  $\text{MASnI}_3$  based perovskite yielded a maximum of 20% conversion efficiency, and in chapter 4, 19.5% conversion efficiency was achieved with  $\text{CsSnI}_3$  perovskite. Both the chapters concluded that efficiency beyond 20% is practically impossible unless we minimize the thermalization and transparent band gap losses. Therefore, in the ongoing chapter, a detailed simulation has been performed to design a perovskite-silicon tandem solar cell to boost the conversion efficiency beyond 20%.

### ***5.1: INTRODUCTION***

A single-junction silicon solar cell or any other single-junction solar cell can achieve maximum efficiency of 32%, and this limit comes from the thermodynamics limit called the Shockley Queisser (SQ) limit (Shockley and Queisser 1961). If we make a very high-efficiency device by using high light-absorbing material and try to optimize the morphology in the best possible way so that the charge transport and also the charge recombination is optimized to get maximum efficiency. Still, there are some limitations which come intrinsically from the device. Because of that, we cannot go beyond a particular number for single-junction cells. Therefore, researchers started stacking many solar cells together to surpass the SQ limit. One can either similar stack kind of solar cell like perovskite-perovskite or can stack perovskite with silicon together to form stacked solar cells known as tandem

solar cells (Ameri, Dennler et al. 2009, Ameri, Li et al. 2013, Leijtens, Bush et al. 2018, Kim, Jung et al. 2021).

This chapter is devoted to discussing the tandem solar cell, which is a unique form of a solar cell consisting of two or more sub cells stacked together to convert more of the sunlight spectrum into electricity and therefore increase the overall cell efficiency( Madan, Pandey et al. 2020, Akhil, Akash et al. 2021). Further, if we have a single junction solar cell from silicon giving an average conversion efficiency of 20% to 22% efficiency and that from a perovskite solar cell of 15% to 20% efficiency, we can make stacking of silicon and perovskite together to utilize the advantage of the silicon as well as the perovskite solar cell (Pandey and Chaujar 2016, Sahli, Werner et al. 2018, Werner, Niesen et al. 2018, Pandey, Singla et al. 2019). This kind of geometry is called a tandem solar cell or silicon-perovskite tandem cell. In the tandem configuration, higher band gap cells are placed on top, and lower band gap cells are placed at the bottom so that the lower wavelength spectrum is utilized by the top cell and the higher wavelength spectrum transmitted by the top cell is absorbed by the bottom cell (You, Dou et al. 2013, Werner, Niesen et al. 2018). These two different components of the hybrid solar cells or the tandem solar cell can be of the same solar cell, for example, perovskite-perovskite, or they can be from different semiconductor families like you can take silicon and also you can take an organic solar cell.

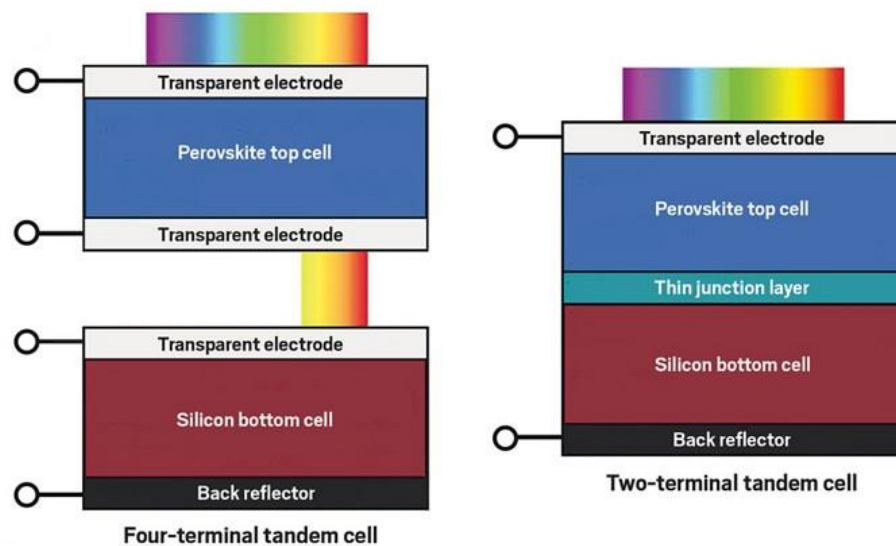


**Figure 5-1** Multijunction tandem structure (a) four terminal or mechanically stacked (b) two-terminal monolithically stacked. Source (Werner, Niesen et al. 2018)

By arranging them like this, we can capture more energy from the sun, and tandem cells are an attractive option for achieving high efficiency. Now looking at Fig. 5-1, we can arrange top and bottom sub cells in two different configurations, such as four terminals mechanically stacked (Fig. 5-1(a)) and two terminals monolithically stacked tandem (Fig. 5-1(b)) configuration. The direction of illumination is through the front electrode or the transparent electrode, and there are two different kinds of solar cell has been sandwiched, namely perovskite on top and silicon on the bottom. In the case of mechanically stacked, both top and bottom sub cells are fabricated individually and then connected in an external circuit, and this configuration demands three transparent electrodes to ensure sufficient optical coupling of photons transmitted by the top cell, as shown in Fig. 5-1(a). Whereas in the case of monolithic stacking, the entire device is fabricated by using layer by layer deposition and requires only one transparent electrode to ensure sufficient utilization of spectrum by both top and bottom subcells. In both the configuration, the top cell directly receives the standard AM1.5G spectrum, and the bottom cell receives the filtered AM1.5G spectrum transmitted by the top cell.

A monolithic stacked configuration is preferred in literature since it requires minimal components and fewer transparent electrodes. Monolithically stacked tandem configuration resembles the circuit of two diodes connected in series, as shown in Fig. 5-2. This configuration demands that an equal amount of current must flow in the circuit all the time, which can only be achieved by ensuring a flow of the same amount of current from both the top and bottom sub cell. This puts a limitation on getting the maximum deliverable  $J_{SC}$  value from the tandem device since this circuit cannot surpass the maximum  $J_{SC}$  deliverable by the top cell, which usually gives lower  $J_{SC}$  compared to the bottom cell owing to the higher band gap (this will be validated in the result section of this chapter). Therefore, the cell giving the lower  $J_{SC}$  will act as a limiting cell in tandem configuration, and the real advantage of this configuration can be noticed in terms of tandem  $V_{OC}$ . Both the cells are connected in series, and hence the total  $V_{OC}$  would be the sum of individual  $V_{OC}$  (this will be validated in the result section of this chapter).

As stated earlier that equal amount of current must flow in the circuit and through both the device, and to ensure the same, a tunnel recombination junction is required, which is sandwiched between the top and bottom sub cell schematically shown in Fig. 5-1(b).

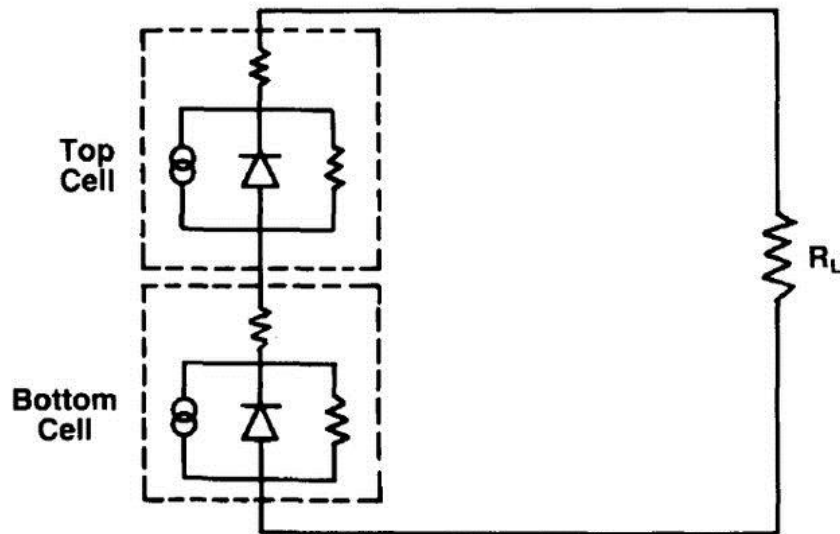


Figure 5-2 Equivalent circuits of two-terminal monolithic tandem solar cells. Source (Pathania, Pandey et al. 2020)

The objective of the tandem cell is to improve the efficiency, so while constructing this structure, one thing has to be kept in mind the charge transport properties should be optimum now. A very common example of a tandem solar cell is a perovskite-silicon tandem cell structure. Here in the top solar cell, we have a perovskite top cell, and in the bottom, we have a silicon bottom cell. Now there are two different solar cells which are coupled opto-electrically. This allows the light to transmit completely and couples the electromagnetic wave or the light which is coming from the top solar cell towards the bottom cell. Perovskite usually has a band gap of 1.3 eV to 2.15 eV, and silicon is 1.1 eV, so the idea is that if we make a tandem by utilizing these two materials so we can utilize the advantages of two different band gap properties of the two different materials because higher band gap corresponds to a particular wavelength of the absorption and lower band gap of 1.1 eV will correspond to a particular wavelength of the absorption. The reflection, transmittance and absorption (R, T, A) plot for a conventional perovskite-silicon tandem solar cell is shown in Fig. 5-3. Here, we can see that the use of perovskite ensures the utilization of the visible spectrum and the spectrum left by perovskite is being absorbed by the bottom sub cell. A

tandem configuration has the potential to get a theoretical efficiency of 44%, and researchers are trying their best to get close to this number.

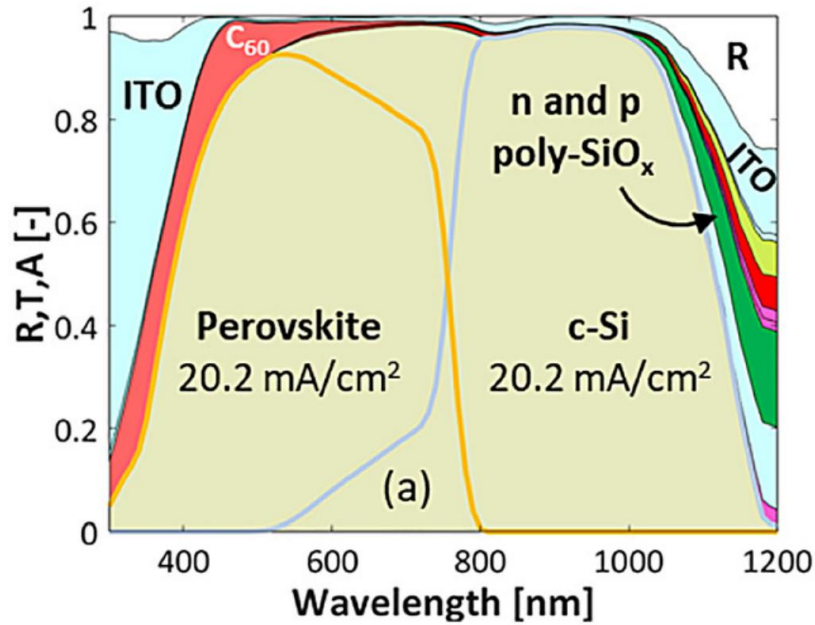


Figure 5-3 Reflection, transmission, and absorption spectrum of perovskite-silicon based tandem solar cells. Source (Singh, Santbergen et al. 2020)

Commercialization of any PV device depends on three important factors, namely manufacturing cost, cell efficiency and cell lifetime. The cost must be as low as possible, and efficiency and lifetime must be higher to have a real commercial application. If we consider the current dominance of the PV market, then silicon-based devices are leaders with a market share of more than 90%. Silicon PV devices give an average conversion efficiency of 22% at the industrial level, and improvement in performance has been stagnant for the last ten years; therefore, further increase in efficiency is like breaking the mountain. It is also equally important that considering the dominance of silicon in the PV industry, one cannot remove the entire fabrication setup overnight. Therefore, it is the right time to assist the silicon-based PV devices to further increase the conversion efficiency using tandem design.

The first perovskite-silicon tandem solar cell was proposed in the year 2015 with 13.7% conversion efficiency (Mailoa, Bailie et al. 2015), and after that, extensive research in this field led to a record conversion efficiency of +29% achieved in the year 2021 (Al-Ashouri, Köhnen et al. 2020). These devices are also ready to be commercialized. However, in all

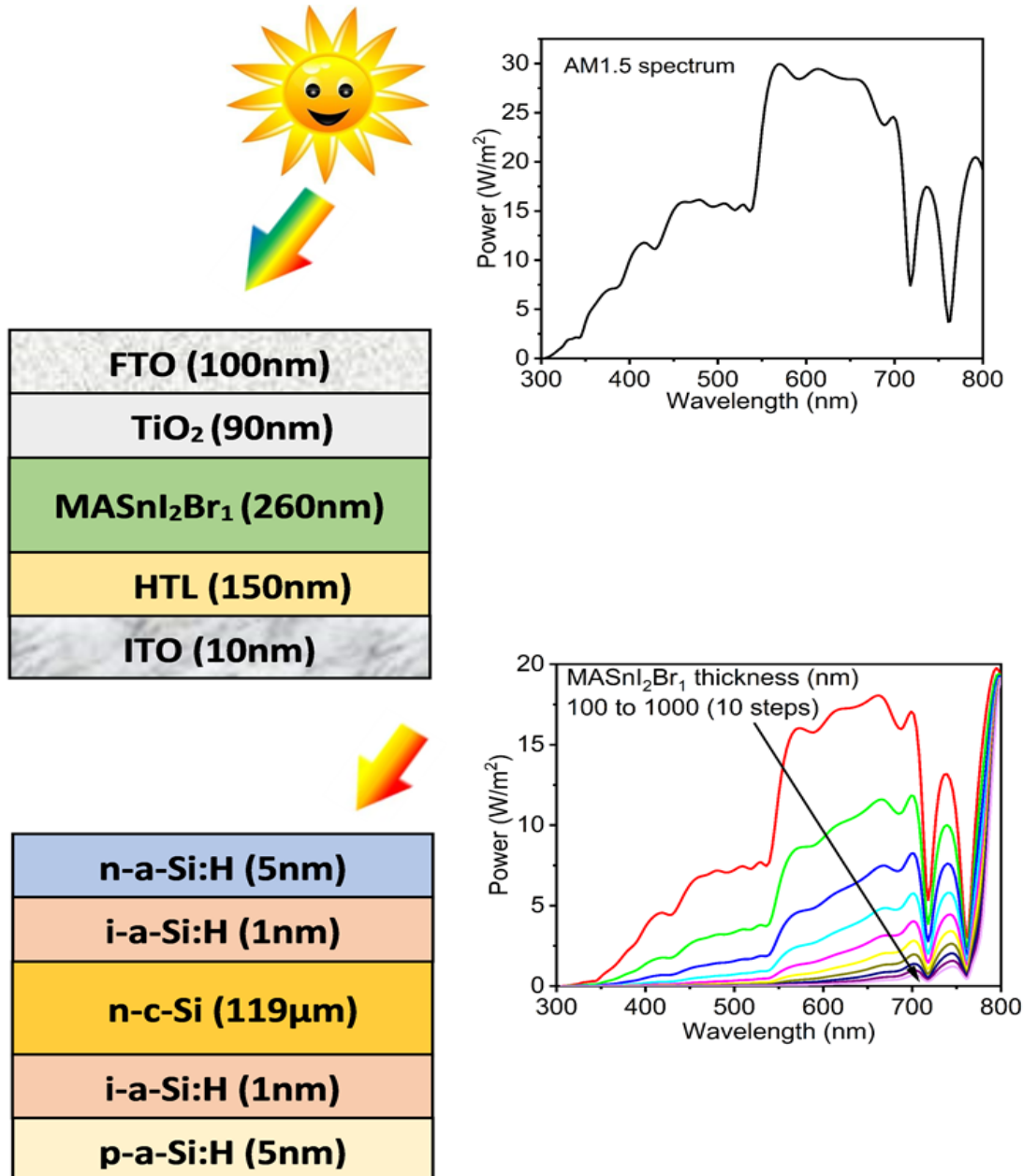
previous perovskite-silicon tandem devices, lead-based halides are being deployed, which are not eco-friendly, as already discussed in the preceding chapters. Therefore, it is important to propose and discuss lead-free perovskite solar cells for top cell application in perovskite silicon tandem solar cells. Here in this chapter, we utilized two different perovskites as explored in the previous chapters, namely  $\text{MASnI}_2\text{Br}_1$  (1.56 eV) and  $\text{CsSnI}_1\text{Br}_2$  (1.65 eV) and applied them in tandem configuration with silicon-based bottom sub cell. The reason for selecting only these two materials is based on the consideration of the top cell energy band gap, which should lie in the range of 1.5 eV to 1.7 eV for perovskite-silicon tandem solar cells. The band gap of the rest of the lead-free perovskite discussed in the previous chapter did not fall in this range and hence was not considered for further analysis.

## **5.2: DEVICE STRUCTURE AND SIMULATION METHODOLOGY**

SCAPS-1D device simulator is again utilized to perform the device simulation for the two different tandem devices under consideration, namely  $\text{MASnI}_2\text{Br}_1$ -Silicon and  $\text{CsSnI}_1\text{Br}_2$ -Silicon-based tandem solar cells.  $\text{MASnI}_2\text{Br}_1$ -Silicon and  $\text{CsSnI}_1\text{Br}_2$ -Silicon tandem devices are named TD1 and TD2 for further discussion in this ongoing chapter. A schematic of the tandem simulation is shown in the following Fig. 5-4(a-b). Two terminal monolithic tandem structures for TD1 and TD2 solar cells are represented in Fig. 5-4(a) and (b), respectively. During tandem simulation using SCAPS-1D, filtered spectrum and current matching approach are extensively utilized (Madan, Shivani et al. 2020, Islam, Jani et al. 2021, Kumar, Singh et al. 2021, Madan, Singh et al. 2021, Pandey, Sharma et al. 2021). Therefore the same approach is adopted in this chapter to design and realize perovskite-silicon tandem solar cells. In the filtered spectrum approach, the top cell is simulated with standard AM1.5G spectrum, and filtered spectrum by the top cell is utilized to simulate the bottom sub cell, followed by obtaining the current matched condition to finally construct the tandem J-V curve. More details about the tandem simulation and corresponding results are provided in the results section.

**CHAPTER 5: DESIGN AND SIMULATION OF PEROVSKITE-SILICON TANDEM SOLAR CELLS USING LEAD FREE PEROVSKITE-BASED TOP CELLS**

The electrical parameters of material used during simulations are listed in Table 5-1, and optical properties are obtained from inbuilt square root at  $E_g$  optical models in SCAPS-1D. Material properties and optimized parameters are the same for  $\text{MASnI}_2\text{Br}_1$  and  $\text{CsSnI}_1\text{Br}_2$  as mentioned in chapters 3 and 4, respectively, whereas, for silicon-based bottom subcell, it is tabulated in Table 5-1 along with interface and bulk defect specification as listed in Table 5-1 and 5-2, respectively.



(a)

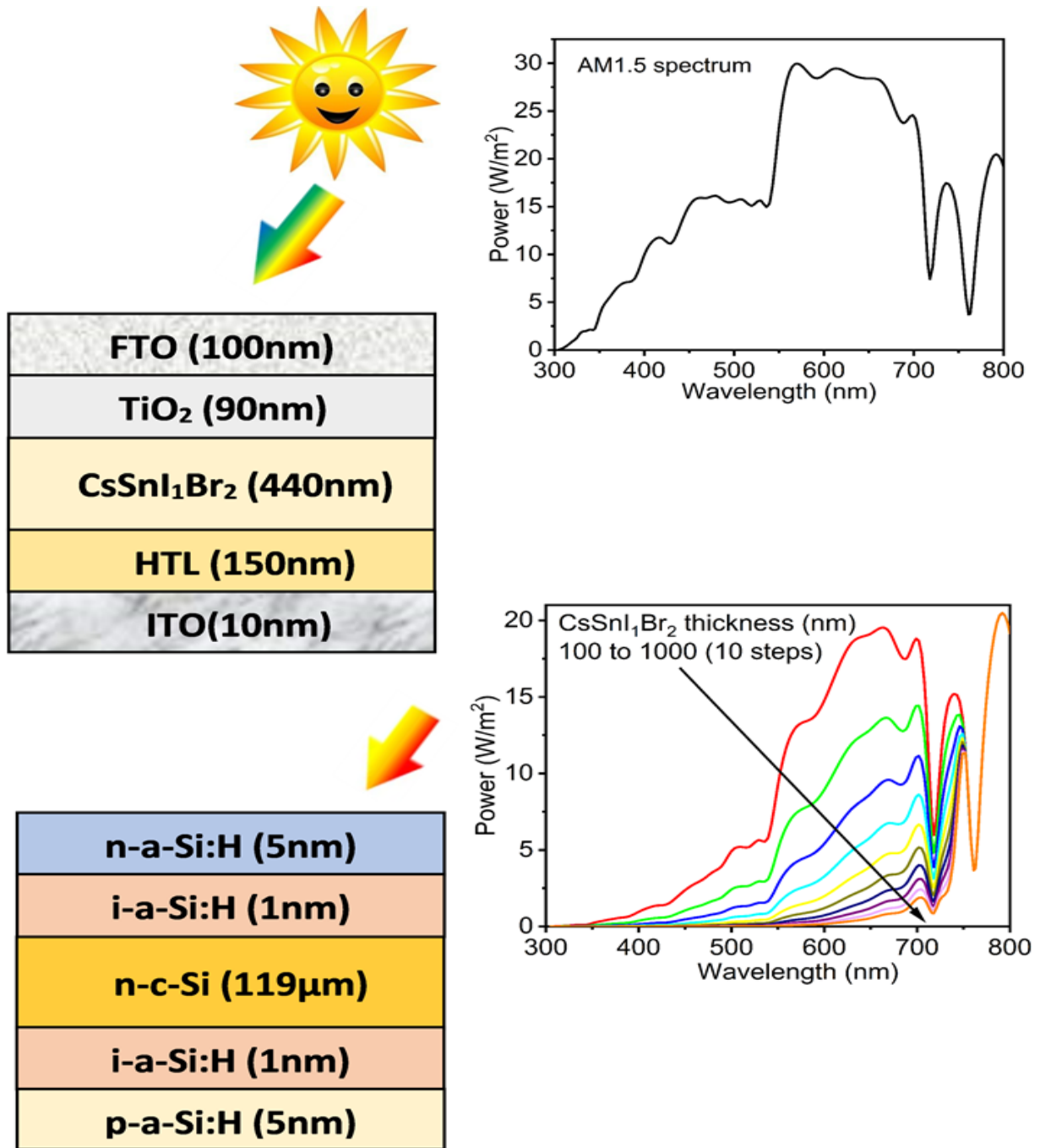


Figure 5-4 Schematic device structures and strategy used for tandem simulation of (a) TD1 and (b) TD2.

**CHAPTER 5: DESIGN AND SIMULATION OF PEROVSKITE-SILICON TANDEM  
SOLAR CELLS USING LEAD FREE PEROVSKITE-BASED TOP CELLS**

Table 5-1 The listed materials are used for the simulation of the bottom cell, and all the data related to its electrical and optical properties are taken from already published papers(Zhao, Zhou et al. 2008, Dao, Heo et al. 2010, Shrivastav, Madan et al. 2021).

Properties	Bottom Cell			
	n-a-Si:H	i-a-Si:H	n- c-Si	p-a-Si:H
Bandgap (eV)	1.74	1.74	1.12	1.74
Electron affinity (eV)	3.8	3.8	4.05	3.8
Dielectric Constant	11.9	11.9	11.9	11.9
CB effective density (/cm <sup>3</sup> )	1×10 <sup>20</sup>	1×10 <sup>20</sup>	2.84×10 <sup>19</sup>	1×10 <sup>20</sup>
VB effective density (/cm <sup>3</sup> )	1×10 <sup>20</sup>	1×10 <sup>20</sup>	1.04×10 <sup>19</sup>	1×10 <sup>20</sup>
Electron mobility (cm <sup>2</sup> /Vs)	20	20	1.4×10 <sup>3</sup>	20
Hole mobility (cm <sup>2</sup> /Vs)	5	5	4.5×10 <sup>2</sup>	5
N <sub>D</sub> (/cm <sup>3</sup> )	1×10 <sup>20</sup>	1×10 <sup>6</sup>		0
N <sub>A</sub> (/cm <sup>3</sup> )	0	1×10 <sup>6</sup>	5×10 <sup>6</sup>	1×10 <sup>20</sup>

Table 5-2Details of interface defect parameters used during the simulations of the bottom cells (Shrivastav, Madan et al. 2021).

Properties	Bottom cell interface defects		
	n-a-Si:H/ i-a-Si:H	i-a-Si:H/ n- c-Si	n- c-Si/ p-a-Si:H
Defect type	Neutral	neutral	neutral
Capture cross section electrons(cm <sup>2</sup> )	1×10 <sup>-15</sup>	1×10 <sup>-15</sup>	1×10 <sup>-19</sup>
Capture cross section holes (cm <sup>2</sup> )	1×10 <sup>-15</sup>	1×10 <sup>-15</sup>	1×10 <sup>-19</sup>
Energetic distribution	Single	single	single
Reference for defect energy level Et	Above the highest E <sub>v</sub>	Above the highest E <sub>v</sub>	Above the highest E <sub>v</sub>
Energy level w.r.t. reference (eV)	.600	.600	.600
Total density (1/cm <sup>2</sup> )	1×10 <sup>1</sup>	1×10 <sup>1</sup>	1×10 <sup>1</sup>

Table 5-3Details of bulk defects parameters considered in intrinsic and p-type and n-type a-Si:H layers (Shrivastav, Madan et al. 2021). Detailed information regarding these parameters can be found in the SCAPS-1D manual.

i-a-Si:H	p-a-Si:H and n-a-Si:H
<b>Defect 1</b> charge type: amphoteric: [+0, 0/-] total density (1/cm3): Uniform 8.000e+16 grading Nt(y): uniform energy distribution: Gauss; Et = [0.70; 0.50] eV below Ec; Ekar = 0.29 eV	<b>Defect 1</b> charge type: amphoteric: [+0, 0/-] total density (1/cm3): Uniform 8.000e+14 grading Nt(y): uniform energy distribution: gauss; Et = [0.70; 0.50] eV below EC; Ekar = 0.29 eV
<b>Defect 2</b> charge type: acceptor: [0/-] total density (1/cm3): Uniform 1.000e+16 grading Nt(y): uniform energy distribution: CB tail; Et = 0.01 eV below Ec; Ekar = 0.10 eV	<b>Defect 2</b> charge type: acceptor: [0/-] total density (1/cm3): Uniform 1.000e+15 grading Nt(y): uniform energy distribution: CB tail; Et = 0.01 eV below EC; Ekar = 0.10 eV
<b>Defect 3</b> charge type: donor: [+0] total density (1/cm3): Uniform 1.000e+16 grading Nt(y): uniform energy distribution: VB tail; Et = 0.01 eV above EV; Ekar = 0.10 eV	<b>Defect 3</b> charge type: donor: [+0] total density (1/cm3): Uniform 1.000e+16 grading Nt(y): uniform energy distribution: VB tail; Et = 0.01 eV above EV; Ekar = 0.10 eV

### **5.3: RESULTS AND DISCUSSIONS**

Tandem simulation of two different devices such as MASnI<sub>2</sub>Br<sub>1</sub>-Silicon named as TD1 and CsSnI<sub>1</sub>Br<sub>2</sub>-Silicon named as TD2 based tandem solar cells are presented in this section. Results are summarized on the basis of filtered spectrum, current matching curve, EQE spectrum and tandem J-V curve.

➤ **Comprehensive analysis of two-terminal monolithic MASnI<sub>2</sub>Br<sub>1</sub>-Silicon and CsSnI<sub>1</sub>Br<sub>2</sub>-Silicon tandem solar cells.**

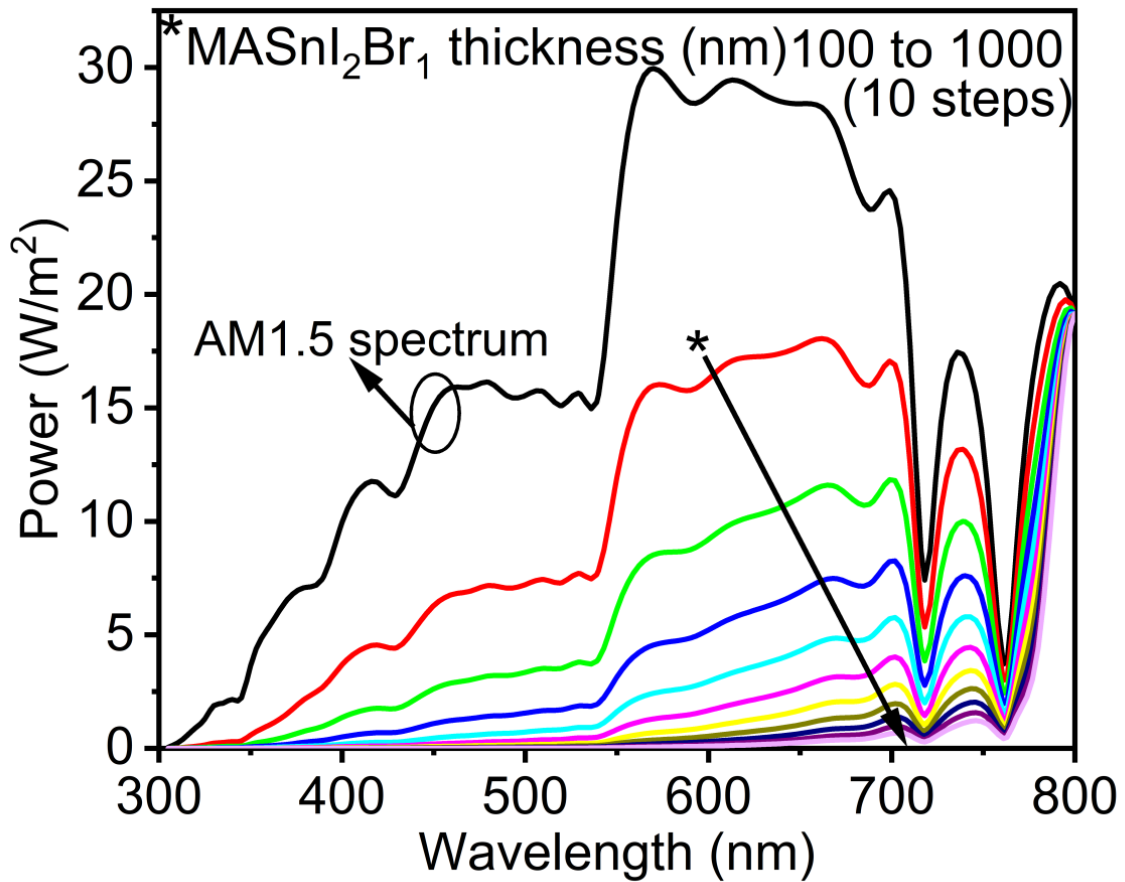
As stated earlier in the introduction section of this chapter, top cells utilize the standard AM1.5G spectrum directly and transmit the filtered part of AM.15G spectrum to the bottom cell. The transmitted spectrum is further utilized by the bottom subcell for PV performance. In the past, researchers reported the formula to calculate the filtered spectrum by top cell on the basis of the absorption coefficient and thickness of each layer used in the top cell (Madan, Shivani et al. 2020, Sarker, Islam et al. 2021, Jafarzadeh, Aghili et al. 2022). The same formula is utilized in this chapter to calculate the filtered spectrum and is mentioned below.

$$T(\lambda) = T_0(\lambda) \exp \left[ \sum_{k=1}^4 - (a_k(\lambda) \cdot d_k) \right]$$

Here  $T(\lambda)$  is the filtered spectrum,  $T_0(\lambda)$  is the input AM1.5G spectrum,  $a_k$  is the absorption coefficient, and  $d_k$  is the thickness. The  $k=1,2,3,4$  corresponds to different materials FTO, TiO<sub>2</sub>, MASnI<sub>2</sub>Br<sub>1</sub> and HTL, respectively for TD1 and FTO, TiO<sub>2</sub>, CsSnI<sub>1</sub>Br<sub>2</sub> and HTL, respectively for TD2 .

While calculating the filtered spectrum by the top cell, the only thickness of the perovskite-based absorber layer is varied in the top cell and obtained filtered

spectrum is shown in Fig. 5-5 (a-b). The thickness of the absorber layer in the top cell is varied from 100 nm to 1000 nm in ten equal spectrums, and obtained filtered is recorded as shown in Fig. 5-5 (a-b). It is important to compare the filtered spectrum at different thicknesses with the actual AM1.5G spectrum; therefore, original AM1.5G is also plotted. It has been observed that increasing the thickness of the absorber layer in the top cell increases the photon absorption in the top cell, but at the same time, it reduces the power of the filtered spectrum that would be utilized by the bottom cell.



(a)

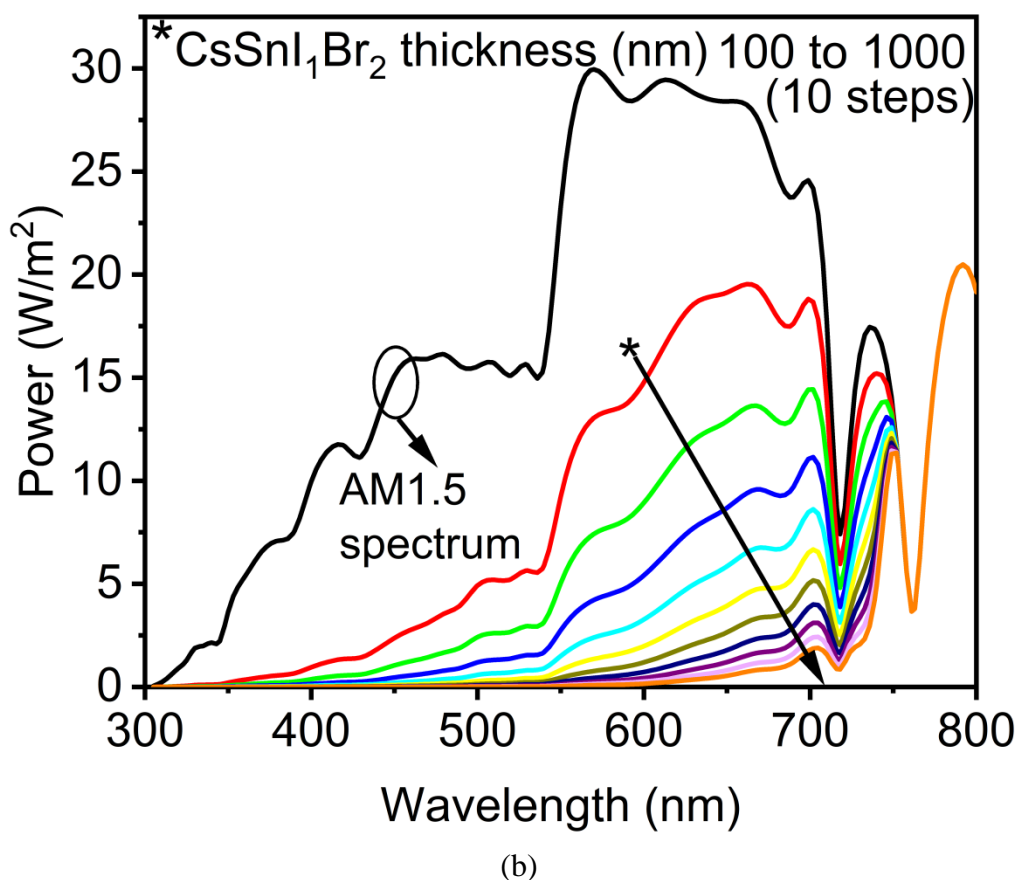
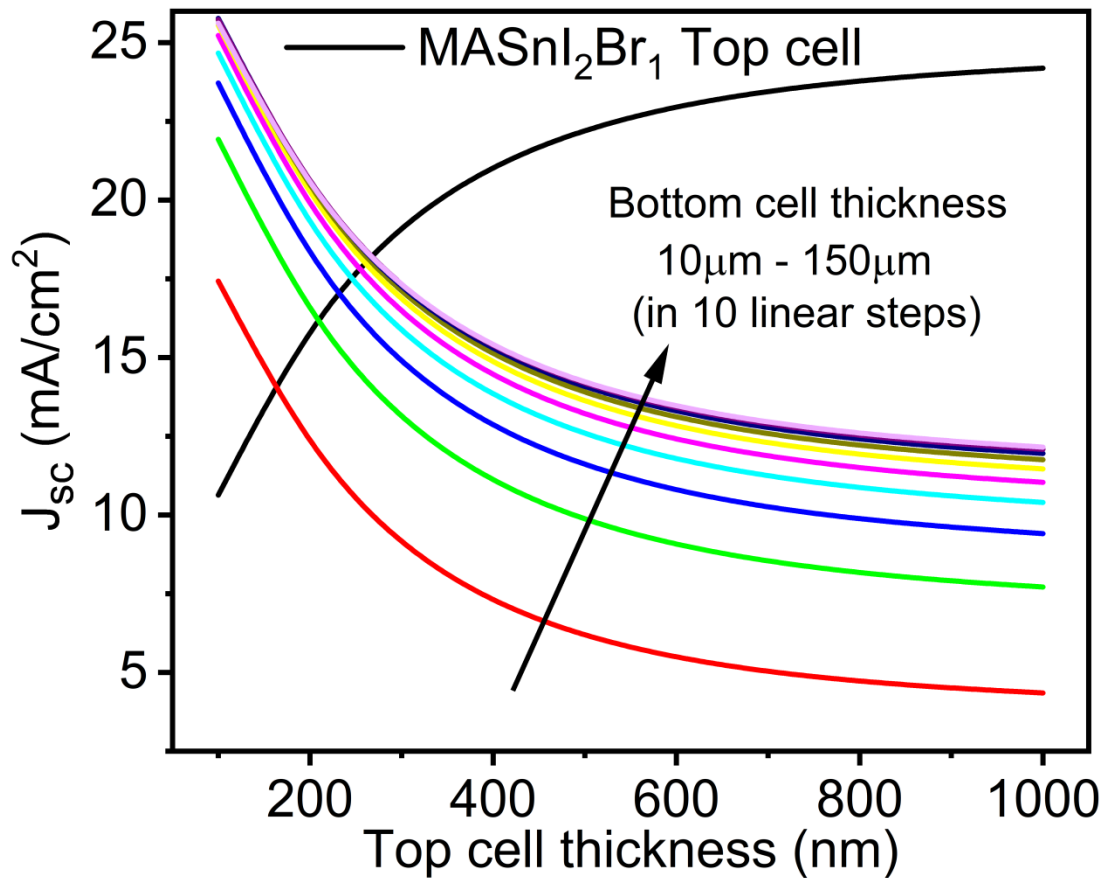


Figure 5-5 Filtered spectrum transmitted by the top cell at different absorber layer thicknesses from 100 nm to 1000 nm (a)  $\text{MA}\text{SnI}_2\text{Br}_1$  based top cell and (b)  $\text{CsSnI}_1\text{Br}_2$  based top cell.

Ten different spectrum files for each device are created using the data obtained from the formula and are further utilized for the bottom cell. Now the bottom cell at various thicknesses from 10  $\mu\text{m}$  to 150  $\mu\text{m}$  is simulated under this filtered spectrum, and its  $J_{\text{SC}}$  values are reported to construct a current matching curve with top cells. Results for the current matching curve are provided in Fig. 5-6 (a-b). It is important to obtain the thickness of both top and bottom subcells where they deliver the same  $J_{\text{SC}}$  value, which is the main requirement of the tandem solar cell. Therefore current matching points are obtained as shown in Fig. 5-6 (a-b). While varying the thickness of both top and bottom subcell and it is observed that in total, ten current matching points are possible; however, it is always required to pick the point which can deliver the maximum  $J_{\text{SC}}$ . In this case, intersect function is utilized to obtain the exact thickness for the top and bottom subcell to get the

maximum possible  $J_{sc}$ . Top cell thickness of 260 nm and bottom cell thickness of 119  $\mu\text{m}$  showed current matched JSC of  $18.26 \text{ mA}\cdot\text{cm}^{-2}$  for TD1 and top cell thickness of 440 nm and bottom cell thickness of 119  $\mu\text{m}$  showed current matched JSC of  $17.14 \text{ mA}\cdot\text{cm}^{-2}$  for TD2.



(a)

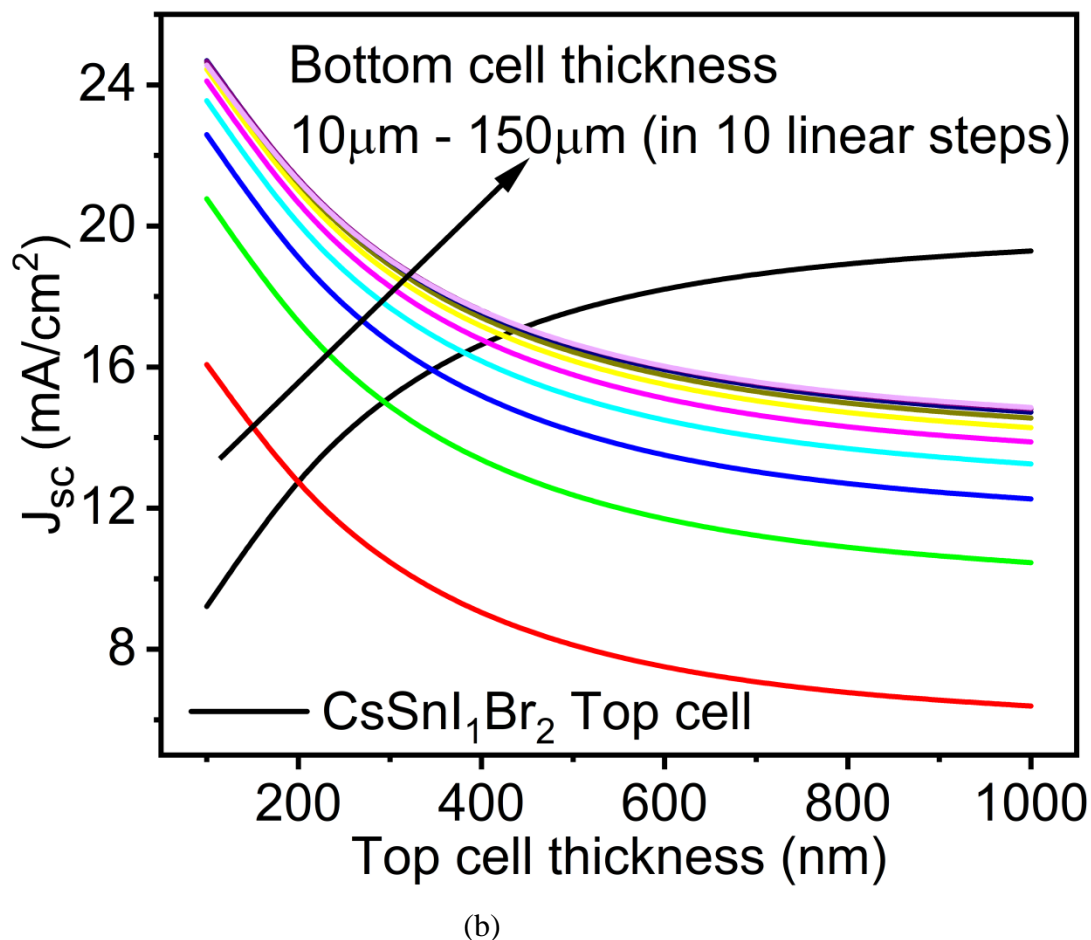
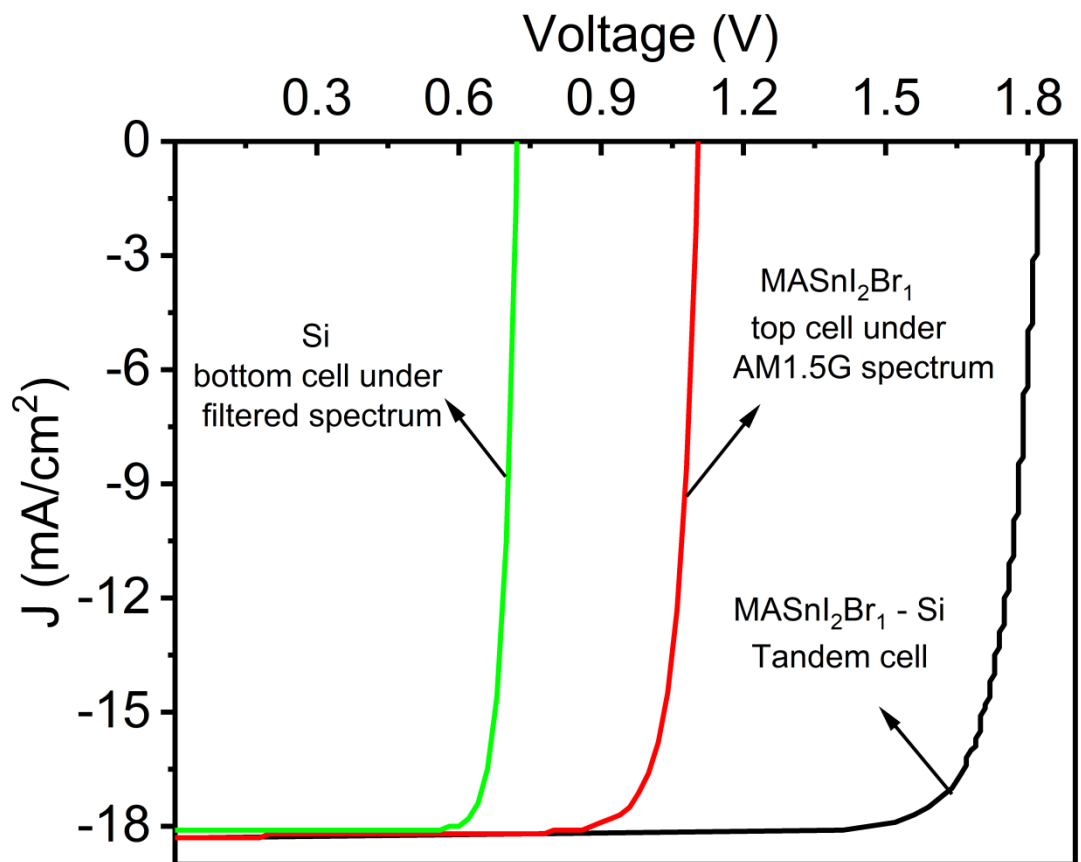


Figure 5-6 Current matching curve for (a) TD1 and (b) TD2 at various top and bottom subcell thicknesses ranging from 100 nm to 1000 nm and 10 μm to 150 μm.

After getting the current matching point, the next step is to construct the tandem J-V curve, which is done by adding the voltage of the top and bottom sub cell at the equal current matching point. The scripting feature of SCAPS-1D is utilized to generate the tandem J-V curve, as shown in Fig. 5-7(a-b). More details about the script are provided in Sec. 5.4. Three different J-V curves are shown in the following figures, which include the J-V curve of the bottom sub cell under filtered spectrum by top cell and top cell under AM.15G spectrum and final tandem J-V curve. It is interesting to note that all the curves intersect at the same value on the y-axis, i.e., the current density axis. This validates that an equal amount of current will flow from the top, bottom and complete tandem device, which is the main requirement. In addition, as mentioned in the introduction

section that the real advantage of the tandem device lies in the  $V_{OC}$ , which is equal to the sum of individual  $V_{OC}$ s of the top and bottom sub cell. Results reported in Fig. 5-7 (a-b) show that net tandem  $V_{OC}$  is equal to the sum of individual  $V_{OC}$ . To get the following curve, the thickness of the top cell is 260 nm, the bottom cell is 119  $\mu\text{m}$ , and the complete tandem device comprises top (260 nm)- bottom (119 $\mu\text{m}$ ) for TD1, and the thickness of the top cell is 440 nm, the bottom cell is 119  $\mu\text{m}$ , and complete tandem device comprise top (440 nm)- bottom (119 $\mu\text{m}$ ) for TD2.



(a)

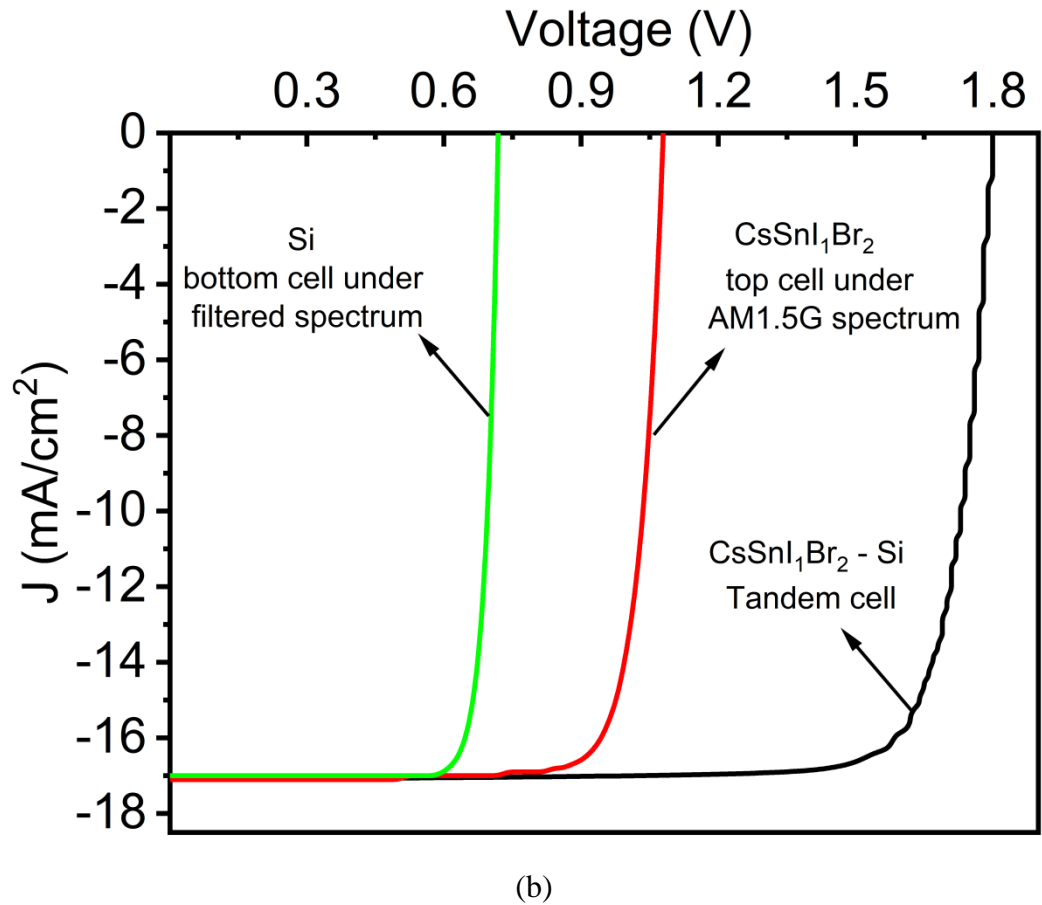
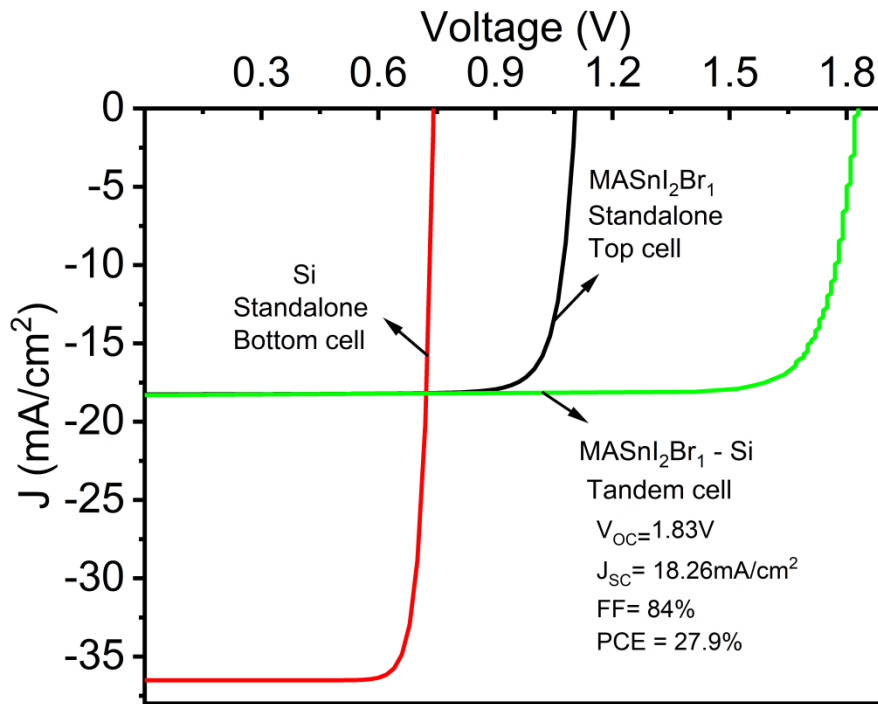
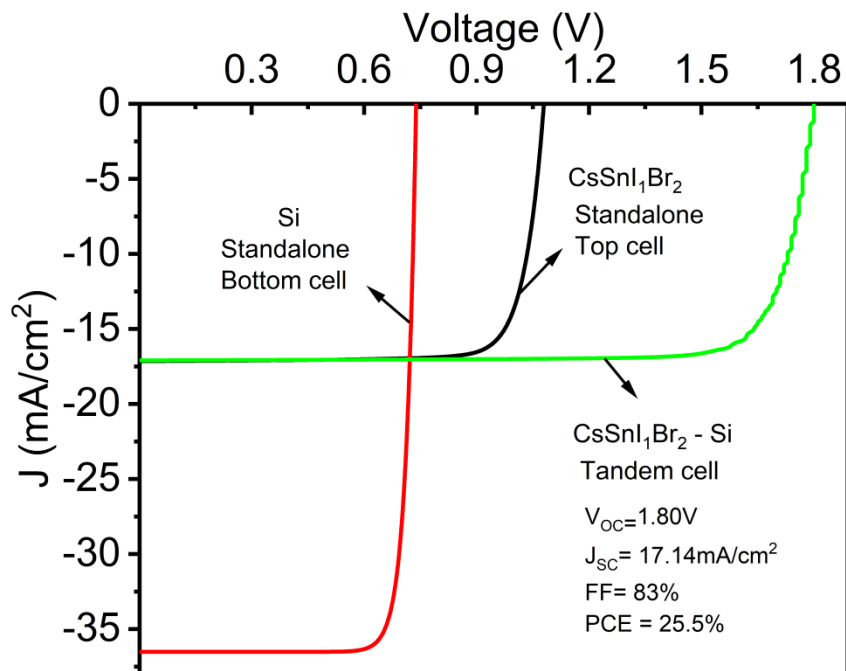


**Figure 5-7**J-V curve of the top cell under AM1.5G, bottom cell under filtered spectrum and tandem cell for (a) TD1 and (b) TD2.

The bottom cell J-V curve reported in Fig. 5-7 (a-b) is obtained when the cell is simulated under a filtered spectrum, but it is also important to compare the performance when the bottom cell is also simulated under AM1.5G spectrum like the top cell and should be compared with the tandem curve. Therefore, another J-V curve is also obtained where both top and bottom sub cells are simulated under the AM1.5G spectrum, and their J-V curves are compared with the tandem curve as shown in Fig. 5-8 (a-b). It can be validated that due to the low band gap, the bottom cell delivered higher  $J_{SC}$ , and the higher band gap of the top cell yielded lower  $J_{SC}$  and acted as a limiting cell in the tandem device. The final tandem device can not surpass the  $J_{SC}$  delivered by the top cell. Therefore, it showed a similar  $J_{SC}$  as the bottom cell. However,  $V_{OC}$  is the sum of both.



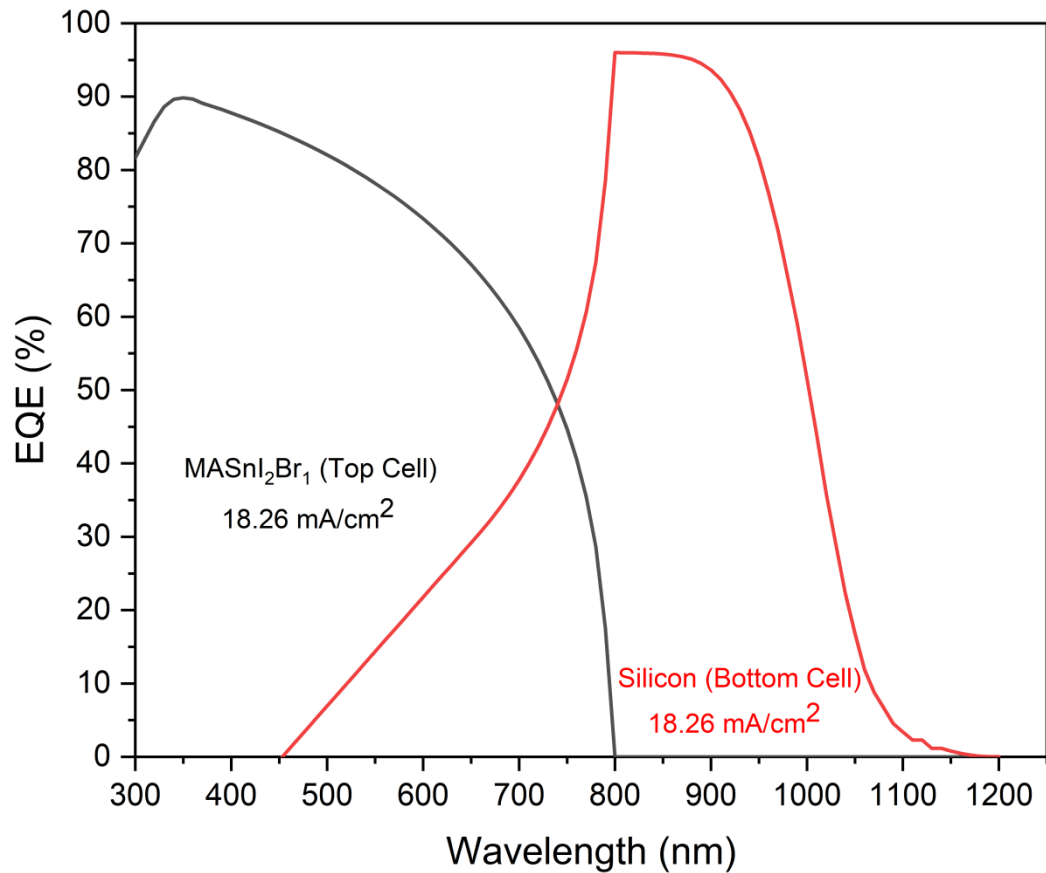
(a)



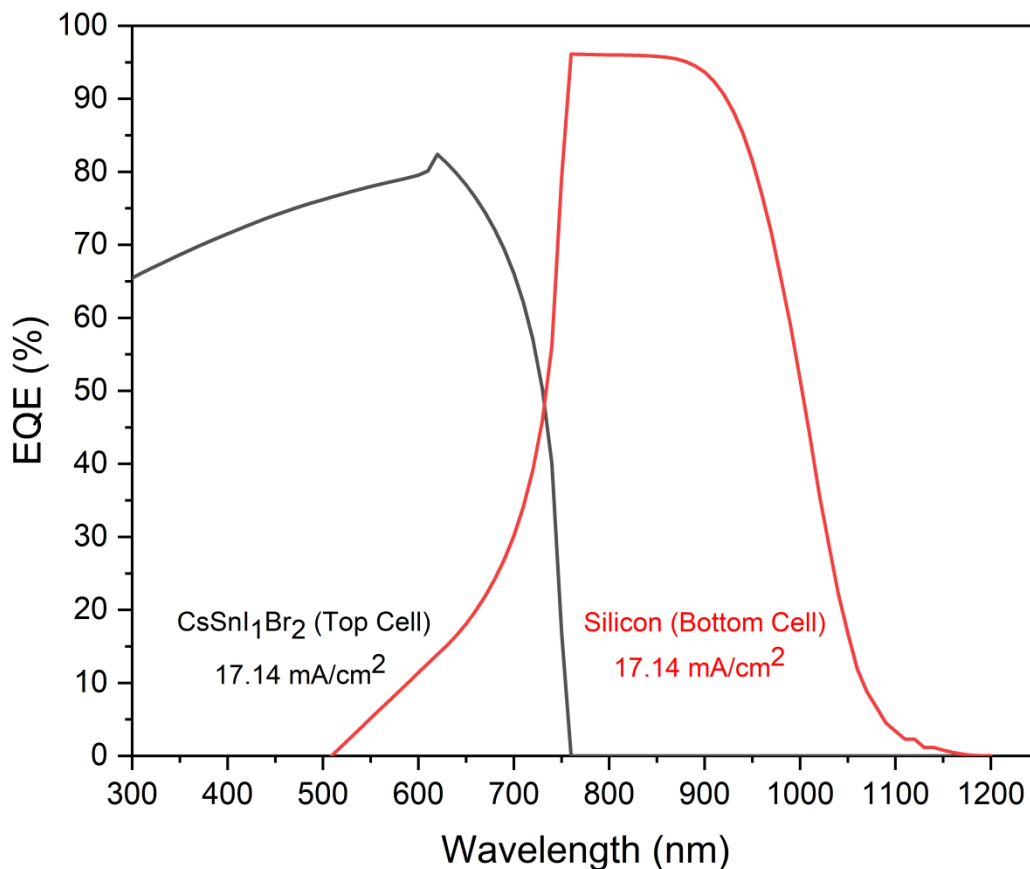
(b)

Figure 5-8 Standalone J-V curve of the top and bottom subcell and tandem J-V curve for (a) TD1 and (b) TD2. Standalone means simulation directly under the AM1.5G spectrum.

External quantum spectrum is also obtained to validate the spectrum utilization by the top and bottom sub cell. The higher band gap top cell utilizes the lower wavelength spectrum, and the lower band gap bottom sub cell uses the higher wavelength, and the same is validated through the data reported in Fig. 5-9 (a-b). The top cell showed the spectrum cutoff close to 800 nm and the bottom sub cell at 1180 nm. Lower wavelength spectrums are utilized by the top cell and are not available for the bottom cell that why EQE for the bottom cell is very low at the lower wavelengths. After the top cell is cut off, all the spectrum is available for the bottom sub cell.



(a)



(b)

**Figure 5-9**Top and bottom cell EQE curve for (a) TD1 and (b) TD2. Integrated  $J_{sc}$  values are also provided to validate the final  $J_{sc}$  values.

This section concludes 27.9% efficient MASnI<sub>2</sub>Br<sub>1</sub>- Si (TD1) and 25.5% CsSnI<sub>1</sub>Br<sub>2</sub>- Si (TD2) monolithic tandem solar cell with  $J_{sc}$ (18.26 mA.cm<sup>-2</sup>),  $V_{oc}$  (1.83 V) and FF of 84% for TD1 and  $J_{sc}$ (17.14 mA.cm<sup>-2</sup>),  $V_{oc}$  (1.80 V) and FF of 83% for TD2, respectively. If we recall chapter 3 and 4, single junction MASnI<sub>2</sub>Br<sub>1</sub>and CsSnI<sub>1</sub>Br<sub>2</sub> showed 19.4% and 15.5% efficiency which is further elevated to 27.9% and 25.5% by combining with the silicon based bottom sub cell in tandem configuration.

## **5.4: SCAPS-1D SCRIPT FOR TANDEM CALCULATIONS**

### **➤ MASnI<sub>2</sub>Br<sub>1</sub> – Si**

```
// SCAPS script
clear all // take a clean start
load definitionfile K_Phula.def // or your def file of the top cell (need to be in the
scaps/def folder)
action spectrumfile AM1_5G 1 sun.spe
set layer2.thickness 0.260
calculate singleshot
get iv xy // for top cell: V is stored in xvector, I in yvector
get characteristics.jsc yvalue // jsc is stored in yvalue
set scriptvariable.yvalue yvector[0] // the first calculated J value is in yvalue
math scalarabs yy // the first calculated |J| value is in yvalue
// show scriptvariables

load definitionfile K_Phula_HIT_for_Bottom_25052021.def // or your def file of
the top cell (need to be in the scaps/def folder)
action spectrumfile KPhula_MASnI2Br1_156_CMT260_B119.spe
set layer3.thickness 119
calculate singleshot
get iv zu // for bottom cell: V is stored in uvector, I in zvector
get characteristics.jsc uvalue // jsc is stored in uvalue

set scriptvariable.vvalue 0.002 // start varying Jtandem from Jsc(top) + this
increment (in mA/cm2) (should be > 0, not <= 0)
math scalarsubtract vvy // starting value for Jtandem
set scriptvariable.wvalue 0 // stop value for Jtandem
math filllinear vvector vvalue wvalue 100 // fill vvector = Jtandem with (here) 100
values from start to stop
// set length of v and w vectors
set scriptvariable.maxiterationnv
set scriptvariable.nwnv
math fillconstant w 0 nw
// show scriptvariables

// start the loop: vary Jtandem
loop start
// find the voltage of the top cell at this Jtandem (by interpolation); set it in xvalue
set scriptvariable.yvalue vvector[loopcounter]
math interpolatexXyY
// find the voltage of the bottom cell at this Jtandem (by interpolation); set it in
zvalue
set scriptvariable.uvalue vvector[loopcounter]
```

```
math interpolatezZuU
// do the series connection: add the voltages of top and bottom cell and place the
result in xvalue
math scalaraddxxz
set scriptvariable.wvector[loopcounter] xvalue // and set this xvalue in wvector
loop stop

// set suitable names the vectors, and plot them
set scriptvariable.xnameVtop (V)
set scriptvariable.ynameJtop (mA/cm2)
set scriptvariable.znameVbottom (V)
set scriptvariable.unameJbottom (mA/cm2)
set scriptvariable.wnameVtandem (V)
set scriptvariable.vname Jtandem (mA/cm2)
show scriptvariables
plot draw wv // the tandem cell I-V
plot draw xy // the top cell I-V
plot draw zu // the bottom cell I-V

// extracting the efficiency parameters of the tandem, and place them in the scalars
xvalue, yvalue,...wvalue
math characteristics.vocxwv
math characteristics.jsc ywv
math characteristics.ffzwv
math characteristics.etauwv
math characteristics.vmppvwv
math characteristics.jmppwwv
show scriptvariables
```

➤ **CsSnI<sub>1</sub>Br<sub>2</sub> – Si**

```
// SCAPS script
clear all // take a clean start
load definitionfile K_Phula_CsSnI1Br2_Top_tandem.def // or your def file of the
top cell (need to be in the scaps/def folder)
action spectrumfile AM1_5G 1 sun.spe
set layer2.thickness 0.440
calculate singleshot
get iv xy // for top cell: V is stored in xvector, I in yvector
get characteristics.jsc yvalue // jsc is stored in yvalue
set scriptvariable.yvalue yvector[0] // the first calculated J value is in yvalue
math scalarabs yy // the first calculated |J| value is in yvalue
// show scriptvariables

load definitionfile K_Phula_HIT_for_Bottom_25052021.def // or your def file of
the top cell (need to be in the scaps/def folder)
```

```
action spectrumfile KPhula_CsSnI1Br2_165_CMT440_B119.spe
set layer3.thickness 119
calculate singleshot
get iv zu // for bottom cell: V is stored in vvector, I in zvector
get characteristics.jsc uvalue // jsc is stored in uvalue

set scriptvariable.vvalue 0.002 // start varying Jtandem from Jsc(top) + this increment
(in mA/cm2) (should be > 0, not <= 0)
math scalarsubtract vvy // starting value for Jtandem
set scriptvariable.wvalue 0 // stop value for Jtandem
math filllinear vvector vvalue wvalue 100 // fill vvector = Jtandem with (here) 100
values from start to stop
// set length of v and w vectors
set scriptvariable.maxiterationnv
set scriptvariable.nwnv
math fillconstant w 0 nw
// show scriptvariables

// start the loop: vary Jtandem
loop start
// find the voltage of the top cell at this Jtandem (by interpolation); set it in xvalue
set scriptvariable.yvalue vvector[loopcounter]
math interpolatexXyY
// find the voltage of the bottom cell at this Jtandem (by interpolation); set it in zvalue
set scriptvariable.uvalue vvector[loopcounter]
math interpolatezZuU
// do the series connection: add the voltages of top and bottom cell and place the result
in xvalue
math scalaraddxxz
set scriptvariable.wvector[loopcounter] xvalue // and set this xvalue in wvector
loop stop

// set suitable names the vectors, and plot them
set scriptvariable.xnameVtop (V)
set scriptvariable.ynameJtop (mA/cm2)
set scriptvariable.znameVbottom (V)
set scriptvariable.unameJbottom (mA/cm2)
set scriptvariable.wnameVtandem (V)
set scriptvariable.vname Jtandem (mA/cm2)
show scriptvariables
plot draw wv // the tandem cell I-V
plot draw xy // the top cell I-V
plot draw zu // the bottom cell I-V

// extracting the efficiency parameters of the tandem, and place them in the scalars
xvalue, yvalue,...wvalue
```

math characteristics.vocxwv  
math characteristics.jsc ywv  
math characteristics.ffzwv  
math characteristics.etauwv  
math characteristics.vmppvwv  
math characteristics.jmppwv  
show scriptvariables

## **5.5: SUMMARY**

This chapter brought the comprehensive study of  $\text{MASnI}_2\text{Br}_1$ - Si and  $\text{CsSnI}_1\text{Br}_2$  - Si based two-terminal monolithic tandem solar cell design with 27.9% and 25.5% conversion efficiency, respectively. Tandem design is investigated using widely used filtered spectrum and current matching techniques. Filtered spectrum is calculated at varying thicknesses of perovskite top cell, and the same is fed to bottom cell for obtaining the current matching curve at different bottom subcell thicknesses. The scripting feature is utilized to calculate the tandem curve.

Chapter 5 concluded 27.9% and 25.5% efficient lead-free perovskite-silicon tandem solar cells for future eco-friendly photovoltaic applications. Next, the chapter provides a brief conclusion and future outlook of the thesis.

## **5.6: REFERENCES**

Akhil, S., et al. (2021). "Review on perovskite silicon tandem solar cells: Status and prospects 2T, 3T and 4T for real world conditions." Materials & Design**211**: 110138.

Al-Ashouri, A., et al. (2020). "Monolithic perovskite/silicon tandem solar cell with > 29% efficiency by enhanced hole extraction." Science**370**(6522): 1300-1309.

Ameri, T., et al. (2009). "Organic tandem solar cells: A review." Energy & Environmental Science**2**(4): 347-363.

Ameri, T., et al. (2013). "Highly efficient organic tandem solar cells: a follow up review." Energy & Environmental Science**6**(8): 2390-2413.

**CHAPTER 5: DESIGN AND SIMULATION OF PEROVSKITE-SILICON TANDEM  
SOLAR CELLS USING LEAD FREE PEROVSKITE-BASED TOP CELLS**

---

Dao, V. A., et al. (2010). "Simulation and study of the influence of the buffer intrinsic layer, back-surface field, densities of interface defects, resistivity of p-type silicon substrate and transparent conductive oxide on heterojunction with intrinsic thin-layer (HIT) solar cell." Solar Energy**84**(5): 777-783.

Islam, M. T., et al. (2021). "Investigation of CsSn 0.5 Ge 0.5 I 3-on-Si Tandem Solar Device Utilizing SCAPS Simulation." IEEE Transactions on Electron Devices**68**(2): 618-625.

Jafarzadeh, F., et al. (2022). "Design and optimization of highly efficient perovskite/homojunction SnS tandem solar cells using SCAPS-1D." Solar Energy**236**: 195-205.

Kim, C. U., et al. (2021). "Strategy for large- scale monolithic Perovskite/Silicon tandem solar cell: A review of recent progress." EcoMat**3**(2): e12084.

Kumar, A., et al. (2021). "Computational Modelling of Two Terminal CIGS/Perovskite Tandem Solar Cells with Power Conversion Efficiency of 23.1%." European Journal of Inorganic Chemistry**2021**(47): 4959-4969.

Leijtens, T., et al. (2018). "Opportunities and challenges for tandem solar cells using metal halide perovskite semiconductors." Nature Energy**3**(10): 828-838.

Madan, J., et al. (2020). "Device simulation of 17.3% efficient lead-free all-perovskite tandem solar cell." Solar Energy**197**: 212-221.

Madan, J., et al. (2020). "Device simulation of 17.3% efficient lead-free all-perovskite tandem solar cell." Solar Energy**197**: 212-221.

Madan, J., et al. (2021). "Comprehensive device simulation of 23.36% efficient two-terminal perovskite-PbS CQD tandem solar cell for low-cost applications." Scientific Reports**11**(1): 1-13.

Mailoa, J. P., et al. (2015). "A 2-terminal perovskite/silicon multijunction solar cell enabled by a silicon tunnel junction." Applied Physics Letters**106**(12): 121105.

Pandey, R. and R. Chaujar (2016). "Numerical simulations: Toward the design of 27.6% efficient four-terminal semi-transparent perovskite/SiC passivated rear contact silicon tandem solar cell." Superlattices and Microstructures**100**: 656-666.

Pandey, R., et al. (2021). "Numerical simulations of 22% efficient all-perovskite tandem solar cell utilizing lead-free and low lead content halide perovskites." Journal of Micromechanics and Microengineering**32**(1): 014004.

**CHAPTER 5: DESIGN AND SIMULATION OF PEROVSKITE-SILICON TANDEM  
SOLAR CELLS USING LEAD FREE PEROVSKITE-BASED TOP CELLS**

---

Pandey, R., et al. (2019). "Toward the design of monolithic 23.1% efficient hysteresis and moisture free perovskite/c-Si HJ tandem solar cell: a numerical simulation study." Journal of Micromechanics and Microengineering**29**(6): 064001.

Pathania, A., et al. (2020). "Design and optimization of 26.3% efficient perovskite/FeSi<sub>2</sub> monolithic tandem solar cell." Journal of Materials Science: Materials in Electronics**31**(18): 15218-15224.

Sahli, F., et al. (2018). "Fully textured monolithic perovskite/silicon tandem solar cells with 25.2% power conversion efficiency." Nature Materials**17**(9): 820-826.

Sarker, S., et al. (2021). "A SCAPS simulation investigation of non-toxic MAgE<sub>3</sub>-on-Si tandem solar device utilizing monolithically integrated (2-T) and mechanically stacked (4-T) configurations." Solar Energy**225**: 471-485.

Shockley, W. and H. J. Queisser (1961). "Detailed balance limit of efficiency of p- n junction solar cells." Journal of Applied Physics**32**(3): 510-519.

Shrivastav, N., et al. (2021). "Investigations aimed at producing 33% efficient perovskite–silicon tandem solar cells through device simulations." RSC Advances**11**(59): 37366-37374.

Singh, M., et al. (2020). "Comparing optical performance of a wide range of perovskite/silicon tandem architectures under real-world conditions." Nanophotonics**10**(8): 2043-2057.

Werner, J., et al. (2018). "Perovskite/silicon tandem solar cells: Marriage of convenience or true love story?–An overview." Advanced Materials Interfaces**5**(1): 1700731.

You, J., et al. (2013). "A polymer tandem solar cell with 10.6% power conversion efficiency." Nature Communications**4**(1): 1-10.

Zhao, L., et al. (2008). "Design optimization of bifacial HIT solar cells on p-type silicon substrates by simulation." Solar Energy Materials and Solar Cells**92**(6): 673-681.

# CHAPTER 6

---

## CONCLUSION AND OUTLOOK OF THE THESIS

---

**This thesis summarizes lead-free perovskite solar cells' importance for standalone and tandem configuration. Important of simulation related work in the field of the solar cell has also been highlighted. A detailed investigation of four different Sn-based halides  $\text{MASnI}_{3-x}\text{Br}_x$  having different iodide, and bromide compositions have been carried out. Analysis and optimization have been carried out regarding absorber layer thickness variation and bulk defect density. Results are interpreted with the help of an energy band diagram and illuminated J-V curves. It has been observed that the best performance is obtained with a 500 nm thick absorber layer having the lowest defect density of  $1 \times 10^{15} \text{ cm}^{-3}$  for all the devices under consideration. The champion device showed 20% conversion efficiency with  $\text{MASnI}_3$  at 500 nm thickness with a bulk defect of  $1 \times 10^{15} \text{ cm}^{-3}$ . Detailed analysis related to transparency of substrate and cathode work function is also reported to understand the influence of these parameters on the performance of lead-free Sn-based perovskite solar cells.**

Next, a comprehensive study of Cs and Sn-based lead-free halide  $\text{CsSnI}_{3-x}\text{Br}_x$  perovskite solar cells having different iodide and bromide composition has been considered since it is also a potential alternative to conventional lead-based perovskite. Therefore, performance optimization of such devices has been carried out in terms of defect density and absorber layer thickness variation for  $\text{CsSnI}_3$ ,  $\text{CsSnI}_2\text{Br}_1$ ,  $\text{CsSnI}_1\text{Br}_2$  and  $\text{CsSnBr}_3$  based perovskites. This resulted in optimum conversion efficiency of 17.1% with the  $\text{CsSnI}_3$  absorber layer-based device. After that, the impact of ETL and HTL doping has been investigated for all four devices to further improve the performance by mitigating the resistive losses associated with

transport layers. Transport layer doping optimization yielded a 19.6% efficient CsSnI<sub>3</sub> based perovskite solar cell.

To minimize thermalization and transparent band gap losses, a comprehensive study of 27.9% efficient MASnI<sub>2</sub>Br<sub>1</sub>- Si and 25.5% efficient CsSnI<sub>1</sub>Br<sub>2</sub> - Si based two-terminal monolithic tandem solar cell design has also been proposed to enhance the conversion efficiency beyond silicon junction limit. Tandem design is investigated using widely used filtered spectrum and current matching techniques. Filtered spectrum is calculated at varying thicknesses of perovskite top cell, and the same is fed to bottom cell for obtaining the current matching curve at different bottom sub cell thicknesses. The scripting feature is utilized to calculate the tandem curve.

Work reported in this thesis would help the researchers working on lead-free perovskite solar cells to fabricate the lead-free perovskite device for higher conversion efficiencies in standalone and tandem configurations. The work of the thesis can be further extended for the design, analysis, and fabrication of different element based lead-free perovskite solar cells in the future.